

Multiscale Cardiovascular Analysis and Simulations for the Understanding of Intra-Uterine Cardiovascular Remodelling

Patricia Garcia Cañadilla

TESI DOCTORAL UPF / 2015

Directors de la tesi:
Dr. Bart Bijmens
Dra. Fàtima Crispi Brillas
Dr. Eduad Gratacós i Solsona

Departament de Tecnologies de la Informació i les Comunicacions
Universitat Pompeu Fabra



This work was carried out at Physense, Department of Information and Communication Technologies, Universitat Pompeu Fabra, Barcelona, Spain; and at BCNatal - Barcelona Center for Maternal-Fetal and Neonatal Medicine, IDIBAPS.

Patricia Garcia-Cañadilla was supported by the Programa de Ayudas Predoctorales de Formación en investigación en Salud (FI12/00362) from the Instituto Carlos III, Spain.

Financial support for this work was provided by Ministerio de Economía y Competitividad (ref. SAF2012-37196); the Instituto de Salud Carlos III (ref. PI11/00051, PI11/01709, PI12/00801, PI14/00226) integrado en el Plan Nacional de I+D+I y cofinanciado por el ISCIII-Subdirección General de Evaluación y el Fondo Europeo de Desarrollo Regional (FEDER) “Otra manera de hacer Europa”; the EU FP7 for research, technological development and demonstration under grant agreement VP2HF (no 611823); The Cerebra Foundation for the Brain Injured Child (Carmarthen, Wales, UK); Obra Social “la Caixa” (Barcelona, Spain); We acknowledge to Boehringer Ingelheim Fonds for the travel grant to do a research stay at LaBS group in Politecnico di Milano.

"Success is not the key to happiness. Happiness is the key to success. If you love what you are doing, you will be successful."
Albert Schweitzer



Abstract

Cardiovascular diseases are nowadays one of the major causes of death in developed countries. Besides the already known risk factors such as lifestyle and genetics, there is a growing evidence that adverse remodelling during prenatal life presents a risk factor for some cardiovascular diseases at later life. Several studies have shown a clear association between low birth weight and increased cardiovascular mortality in adulthood, including an increased risk of hypertension, diabetes, etc. Recent studies have demonstrated that fetuses with intra-uterine growth restriction show cardiovascular remodelling at organ, vascular and also cellular and subcellular level, and moreover these changes persist postnatally. However this is a complex mechanism that needs to be further investigated. Currently, Doppler ultrasonography is one of the techniques most used to assess the fetal cardiovascular status and to study the heart and vascular remodelling in clinical practice. However, some of underlying hemodynamic and vascular changes cannot be assessed clinically and more sophisticated techniques are needed.

Computational modelling of biological systems arises as a powerful tool to overcome this challenge, to support clinicians and to improve the understanding of different pathologies. In this thesis we proposed the use of computational models of fetal circulation, of cardiac cells and also image processing tools, to improve the understanding of intra-uterine cardiac remodelling that takes place at different scales of the fetal cardiovascular system, and also to estimate the patient-specific hemodynamic properties that cannot be directly assessed from clinical measurements.

Therefore, the aim of this thesis was to develop computational models and tools for the study of intra-uterine cardiovascular remodelling at vascular and cellular level in fetuses with intrauterine growth restriction. The results arising from this thesis demonstrate that computational models are able to improve the understanding and detection of the intra-uterine cardiovascular remodelling by means of patient-specific simulations.



Resum

Les malalties cardiovasculars són avui en dia una de les principals causes de mortalitat en països desenvolupats. Deixant de banda els factors de risc relacionats amb l'estil de vida i la genètica, existeix una creixent evidència de què la remodelació adversa durant la vida prenatal esdevé un factor de risc per a algunes malalties cardiovasculars en l'edat adulta. Diversos estudis han demostrat l'existència d'una clara associació entre tenir un baix pes al néixer amb l'augment de la mortalitat a causa de malalties cardiovasculars durant la vida adulta, incloent a més a més un major risc de patir hipertensió, diabetes, etc. S'ha demostrat que els fetus amb restricció de creixement intrauterina mostren signes de remodelació cardiovascular tant a nivell d'òrgan, vascular com a nivell cel·lular i subcel·lular, i molts cops aquests canvis persisteixen postnatalment. No obstant, és tracta d'un mecanisme complex que necessita ser investigat en profunditat. Actualment, l'ecografia Doppler és una de les tècniques més emprades per avaluar l'estat cardiovascular fetal i per estudiar la remodelació tant cardíaca com vascular durant la pràctica clínica. No obstant, alguns dels canvis hemodinàmics i vasculars subjacents no es poden avaluar clínicament, requerint de tècniques més sofisticades.

El modelatge computacional de sistemes biològics es presenta com un potent instrument per superar aquest repte, per donar suport als metges i millorar la comprensió de les diferents patologies. En aquesta tesi es presenta per una banda l'ús de models computacionals tant de la circulació fetal com també de la cèl·lula cardíaca i la utilització d'eines de processat d'imatge amb la finalitat de millorar la comprensió de la remodelació cardiovascular intrauterina que té lloc a diferents escales del sistema cardiovascular fetal, i estimar les propietats hemodinàmiques específiques de cada pacient, les quals no es poden extreure directament a partir de mesures clíniques.

En conseqüència, l'objectiu central d'aquesta tesi és el desenvolupament de models computacionals i la creació d'eines per a l'estudi de la remodelació cardiovascular intrauterina tant a nivell vascular com cel·lular en fetus amb restricció del creixement intrauterí. Els resultats derivats d'aquesta tesi demostren que els models computacionals són capaços de millorar la comprensió i la detecció de la remodelació cardiovascular intrauterina mitjançant simulacions específiques del pacient.



Contents

Abstract	iii
Resum	v
Acronyms and abbreviations	xvii
1 Introduction	1
1.1 Motivation	2
1.2 The fetal circulation system	3
1.2.1 Structure of the fetal heart	4
1.2.2 Electrical conduction system	5
1.3 The cardiac cell	6
1.4 Cardiovascular remodelling in IUGR and its postnatal persistence	8
1.4.1 Blood flow redistribution (brain sparing effect) in IUGR fetuses	9
1.4.2 Ultrastructural remodelling	10
1.5 Survey of the state of the art of computational models	12
1.5.1 Lumped models of the fetal circulation	13
1.5.2 Electromechanical models of the cardiac cell	14
1.6 Hypothesis and Objectives	15
2 A computational model of the fetal circulation to quantify blood redistribution in intrauterine growth restriction	17
2.1 Introduction	19
2.2 Methods	20
2.2.1 Study individuals	20
2.2.2 Lumped model of the fetal circulation	21
2.2.3 Simulations	25
2.3 Results	27
2.3.1 Characteristics of the study individuals	27

vii

2.3.2	Calibration of the equivalent lumped model in normal conditions	29
2.3.3	Parametric study of flow changes in the AoI and CA	29
2.3.4	Patient-specific modelling	31
2.4	Discussion	32
2.5	Conclusions	36

3	Understanding the aortic isthmus Doppler profile, and its changes with gestational age, using a lumped model of the fetal circulation	41
3.1	Introduction	43
3.2	Methods	45
3.2.1	Lumped model of the fetal circulation	45
3.2.2	Validation of the lumped model for assessing the AoI flow profile	46
3.2.3	Single and multi parametric analysis to study what influences the AoI flow	46
3.3	Results	47
3.3.1	Validation	47
3.3.2	Single parametric studies	47
3.3.3	Multi parametric study	48
3.3.4	Simulating the advance of gestation	49
3.4	Discussion	51
3.5	Conclusions	56
3.A	Appendix: Validation of the lumped model for assessing the AoI flow profile	57
3.A.1	Study individuals	57
3.A.2	Patient-specific fitting	57
3.A.3	Results of the validation of the lumped model for assessing AoI flow profile	58
3.B	Supplementary methods	59
3.B.1	Obtaining blood flow waveforms from Doppler recordings	59
3.B.2	Patient-specific fitting	59
3.B.3	Aortic and pulmonary artery blood flows definition	60
3.B.4	Single parametric studies	61
3.B.5	Multi parametric analysis	63
3.B.6	Simulating the advance of gestation	64

4	Patient-specific estimates of vascular and placental properties in growth-restricted fetuses based on a model of the fetal circulation	67
4.1	Introduction	69
4.2	Methods	70
4.2.1	Study population	70
4.2.2	Patient-specific modeling	71
4.2.3	Placental evaluation	73
4.2.4	Statistical analysis	74
4.3	Results	75
4.3.1	Study population	75
4.3.2	Model-based parameters and feto-placental Doppler	76
4.3.3	Model-based parameters and placental evaluation	76
4.3.4	Model-based parameters and perinatal outcome	78
4.4	Discussion	79
4.5	Conclusions	82
4.A	Appendix A	84
4.B	Appendix B	85
5	Automated cardiac sarcomere analysis from second harmonic generation images	89
5.1	Introduction	91
5.2	Methods	93
5.2.1	Image processing	93
5.2.2	Simulation of computer generated muscle fibers	94
5.2.3	Analysis of biological samples	96
5.3	Results	97
5.3.1	Rubustness analysis with numerical simulations	97
5.3.2	Manual vs. automatic quantification of muscle fibers	98
5.3.3	Quantification of sarcomeres at different SNRs and status	98
5.4	Discussion	101
5.5	Conclusions	103
6	A two dimensional electromechanical model of a cardiomyocyte to assess intra-cellular regional mechanical heterogeneities	105
6.1	Introduction	107
6.2	Methods	108
6.2.1	Cardiomyocyte imaging and quantification	108
6.2.2	Description of the model	110
6.2.3	Multi-parametric analysis of the local strain	112

6.2.4	Cell-specific finite-element simulation of a cardiomyocyte contraction	113
6.3	Results	114
6.3.1	Evaluation of the experimentally measured relationship between local calcium and contraction	114
6.3.2	Quantification of the local strain and Ca^{2+} transients	115
6.3.3	Initial conditions for Young's modulus: relationship between elasticity and strain	116
6.3.4	Multi-parametric analysis of the local strain	117
6.3.5	Cell-specific simulation of a cardiomyocyte contraction	118
6.4	Discussion	119
6.5	Conclusions	122
7	Conclusions	123
7.1	General conclusions	124
7.2	Overview	124
7.3	Future perspective	126
	References	129
	Publications	xvii
	Acknowledgements	xxi
	Curriculum Vitae	xxiii

List of Figures

1.1	The fetal cardiovascular system.	3
1.2	Structure and electrical conduction system of the fetal heart.	5
1.3	Structure of the cardiomyocytes, the cells that compose the myocardial wall within the heart.	7
1.4	Cardiomyocyte architecture, intracellular organelles and ion channels involved in the cardiac excitation–contraction coupling.	7
1.5	Two-dimensional apical 4-chamber views at end diastole illustrating the more globular cardiac shape in IUGR. Adapted from Crispi et al. [7].	8
1.6	Blood flow redistribution (brain-sparing effect) in IUGR fetuses	10
1.7	(a) Electrical equivalent model of an arterial segment and (b) a three-element Windkessel model of a vascular bed.	14
2.1	Anatomical simplified configuration and equivalent lumped model of the fetal circulation.	23
2.2	Doppler ultrasound data of the study individuals.	29
2.3	Measured and model-based flow and pressure waveforms of the control fetus.	30
2.4	Model-based flow waveforms in the aortic isthmus and cerebral arteries.	32
2.5	Plots of the aortic isthmus flow related indexes.	33
2.6	Plots of the cerebral arteries and descending aorta flow related indexes.	38
2.7	Measured and model-based flow waveforms and model parameters of the intrauterine growth restricted fetuses.	39
3.1	Anatomical simplified configuration of the fetal circulation	46
3.2	Characterization of the aorta and pulmonary artery velocity profiles	48
3.3	Patient-specific fitting	50

3.4	Model-based waveforms of the single parametric analyses	52
3.5	Model-based aortic isthmus waveforms of the single parametric analyses of vasculature changes	53
3.6	Model-based waveforms of the simulation of the advance of gestation without considering changes throughout gestation of the timing variables of both pulmonary and aortic flows	53
3.7	Model-based waveforms of the simulation of the advance of gestation considering changes throughout gestation of the timing variables of both pulmonary and aortic flows	54
4.1	A schematic representation of the lumped model of the fetal circulation	72
4.2	Block diagram of the implemented algorithm for the patient-specific fitting.	73
4.3	Measured and model-based velocity waveforms in the AoI, MCA and UA for a control and an IUGR fetus	77
4.4	Model-based parameters estimated with the model for the 13 evaluated placentas.	79
4.5	Model-based parameters for the three groups: controls, IUGR and fetuses with adverse perinatal outcome.	81
5.1	Schematic representation, electron microcopy image and also SHG signal of a sarcomere	92
5.2	Computer generated muscle fibers	94
5.3	Success rate and root-mean square error of the different sarcomeric distances for all the simulated scenarios	98
5.4	Real values of the sarcomere length (SL) of the simulated computer generated muscle fibers plotted against the corresponding estimated values	99
5.5	Estimation of the local fiber orientation in SHG images.	100
5.6	Output of the algorithm: distribution of the four sarcomeric characteristics in a SHG image	100
5.7	Examples of SHG images from (a) young adult rabbit cardiac tissue with a SNR of 23 dB and (b) fetal rabbit cardiac tissue with a SNR of 17 dB.	101
6.1	(a) Correlation between local time of sarcomere re-lengthening (τ_{sl}) and local time of Ca^{2+} decay (τ_{Ca}) in one of the three cardiac cells. (b) Correlation between local maximal contraction (ϵ_l^{max}) and local maximum Ca^{2+} amplitude (Ca_{max}^{2+}) in one of the three cardiac cells.	115
6.2	Acquired images during the cardiac cell experiments	116

6.3	Local and global Ca^{2+} transients from images shown in Figure 6.2.	116
6.4	Estimated local strain from the cell shown in Figure 6.2 . . .	117
6.5	Maximum longitudinal strain (ϵ_l^{max}) plotted against the different Young's modulus E	117
6.6	Results of the cell-specific simulations	119
6.7	Comparison between the (a) real line-scan transmitted light image and a (b) virtual line-scan image created by plotting the local displacements of the simulated cell points across time.	120



List of Tables

1.1	Analogy between circulation and electrical elements in lumped 0D models.	13
2.1	Equations describing vessel's length, diameter and Young's modulus (E)	24
2.2	Prenatal ultrasound and perinatal characteristics of the study population	28
2.3	Comparison between reported and model-based combined cardiac output (CCO) distribution in a control fetus of 33 weeks of gestational age.	30
2.4	Values of the initial peripheral resistances and estimated compliances	31
2.5	Modelling results for the control and the three IUGR fetuses.	34
3.1	Prenatal ultrasound and perinatal characteristics of the study individuals	49
3.2	Values of the estimated parameters after nonlinear optimization	51
3.3	Results of the multivariate regression analysis	51
4.1	Doppler parameters before delivery and perinatal characteristics of normally grown (control) and IUGR fetuses	75
4.2	Model-based parameters estimated for all the fetal population	76
4.3	Multiregression analysis between the Doppler and the model-based parameters.	78
4.4	Categories/subcategories of placental attributes (n=13) consistent with under-perfusion in study population.	78
4.5	Doppler and model-based parameters of the fetal population classified to have or not an adverse perinatal outcome.	80
4.6	Accuracy, sensitivity and specificity of the logistic regression analysis for detecting adverse perinatal outcome.	80

4.7	Equations describing the dimensions and Young's moduli (E) of the different arterial segments of the fetal circulation included in the lumped model.	85
4.8	Exponents "b" of the allometric equations for scaling vascular bed resistances and compliances.	85
5.1	Comparison of muscle fibers morphometric measurements (mean \pm standard deviation) calculated with our algorithm against manual measurements in 30 different regions within the same image.	100
5.2	Results of the automatic measurement of muscle fibers morphology in two sets of images	101
6.1	Results from the multivariate regression analysis for the maximum contraction amplitude and the time of re-lengthening.	118
6.2	Results of the cell-specific simulations performed for three different cardiomyocytes.	119

Acronyms and abbreviations

2D	Two-dimensional
ABL	A-Band length
AoI	Aortic isthmus
Ao	Aorta
ATP	Adenosine triphosphate
AV	Atrioventricular node
BCT	Brachiocephalic trunk
CA	Cerebral arteries
CCO	Combined cardiac output
CO	Cardiac output
CPR	Cerebroplacental ratio
DOM	Depth of modulation
EDF	End-diastolic flow
ET	Ejection time
FO	Fiber orientation
FT	Fourier transform
GA	Gestational age
HR	Heart rate
ICA	Internal carotid artery
IFI	Isthmic flow index
IUGR	Intrauterine growth restriction
LV	Left Ventricle
MBP	Mean blood pressure
MCA	Middle cerebral artery
pA	Pulmonary artery
PI	Pulsatility index
RMSE	Root-mean-square error

RV	Right Ventricle
SA	Sinoatrial node
SD	Standard deviation
SE	Standard error
SHG	Second Harmonic Generation
SL	Sarcomere length
SNR	Signal-to-noise ratio
SR	Sarcoplasmic reticulum
TPV	Time-to-peak velocity
TTIL	Thick-thin interaction length
UA	Umbilical Artery
UtA	Uterine Artery
WGN	White gaussian noise

CHAPTER **1**

Introduction

1.1 Motivation

Cardiovascular diseases are the leading cause of mortality on developed countries, with around 4 million of deaths in Europe [1]. In most cases, cardiovascular diseases have a long subclinical period before starting clinical manifestations [2, 3]. Beside the already known risk factors related to lifestyle and genetics, there is a growing evidence that some cardiovascular diseases have their origin during prenatal life [4, 5]. Numerous historical cohorts [4, 5] and some animal models [6] studies have shown a clear association between low birth weight and increased cardiovascular mortality in adulthood, including risk of hypertension, diabetes, dyslipidemia and impaired coagulation in children and adults. This is known as fetal programming of diseases in adulthood: an insult in utero can lead to functional changes in key organs remaining in postnatal life and leading to increased risk of various diseases in adulthood [4, 5]. There are many fetal conditions that can lead to fetal cardiac remodelling in utero which often persist postnatally. In total it is estimated that more than 10% of pregnancies may show some cardiovascular remodelling. The most studied is the intrauterine growth restriction (IUGR) [7].

Small-for-gestational-age (SGA) is defined as a low birth weight (below 10th percentile). The terms SGA and IUGR are often used interchangeably, although this is misleading. The growth-restricted fetus is a fetus that fails to reach its growth potential and is at risk for adverse perinatal morbidity and mortality. Not all fetuses with an estimated weight below the 10th percentile are at risk for adverse perinatal outcome; many are just constitutionally small. IUGR refers to the fetus who is SGA and shows other signs of chronic hypoxia or malnutrition [8]. It is mostly due to placental insufficiency resulting in a chronic restriction of oxygen and nutrients to the fetus [8]. IUGR cases account for 5-10% of pregnancies and is one of the main causes of perinatal mortality [8] and long term disability. The heart is a key organ in the fetal adaptive mechanisms to placental insufficiency and hypoxia [9]. Multiple studies have demonstrated that IUGR cases show adverse cardiac remodelling in utero [9, 10]. Adverse cardiac remodelling is present from early stages of fetal impairment and worsens progressively with fetal damage [10, 11]. Additionally, as a part of the phenomena of adaptation, IUGR fetuses show a hypertensive status and hemodynamic redistribution associated with in utero volume and pressure overload [12].

For all of this, it would be very important and clinically relevant to better understand the mechanisms of cardiovascular remodelling in IUGR and/or other fetal pathologies. This would allow us to find new biomarkers and therapeutic strategies and therefore to improve the future cardiovascular health of these fetuses.

1.2 The fetal circulation system

During prenatal life, the fetal circulatory system works differently than after birth. The principal difference is that the fetus gets the oxygen and nutrients from the mother through the blood vessels in the umbilical cord that connects the fetus to the placenta. A diagram of the fetal cardiovascular system illustrating the main differences from the neonatal circulation is shown in Figure 1.1.

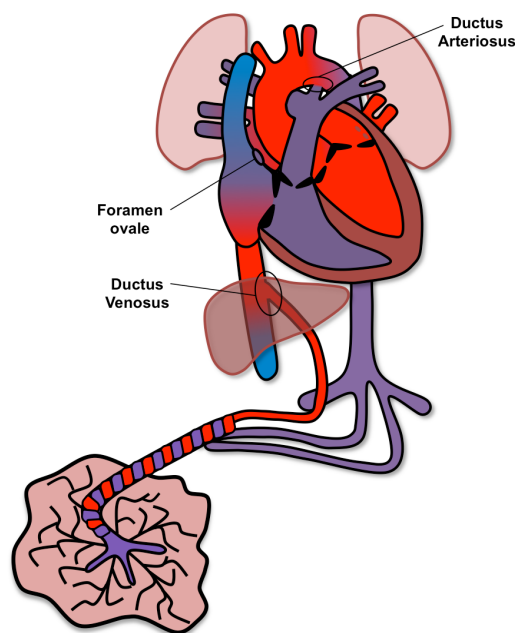


Figure 1.1: The fetal cardiovascular system.

The fetal circulation is characterized by 3 vascular shunts:

- **Foramen ovale.** It is a opening situated between the left and right atria that allows blood to pass from right to left atria.
- **Ductus arteriosus.** It is an arterial connection between the pulmonary artery and the aorta. Since the lungs are not in use to get the oxygen, they present a large resistance to blood flow and most of the blood coming from the right ventricle is diverted to the systemic circulation through the ductus arteriosus. It closes at birth.
- **Ductus venosus.** It shunts part of the blood of the umbilical vein directly to the inferior vena cava. Thus, it allows oxygenated blood from the placenta to bypass the liver.

1.2. *The fetal circulation system*

The process of fetal blood oxygenation is performed in the placenta, from where the oxygenated blood is leaving through the umbilical vein to the fetal circulatory system. This blood presented the highest O_2 concentration. The blood reaches the inferior vena cava, where it is partially mixed with the deoxygenated blood that this vessel is transporting from the bottom part of the fetal body. All this blood that goes through the umbilical vein arrives at the right atrium of the heart. Since pressure in the right atrium is larger than pressure in the left, most of the blood is shunted through the foramen ovale into the left atrium, and only a small portion goes through the tricuspid valve. The right atrium receives also deoxygenated blood from the superior vena cava (which brings blood used by the upper part of the fetal body) and the coronary sinus (with blood used by the heart); the blood entering from these two pathways passes preferentially towards the right ventricle through the tricuspid valve. The blood in the right ventricle goes to the pulmonary artery, but as the lungs are not functional only a small amount reach the pulmonary capillaries and most of the blood goes through the ductus arteriosus to the aortic arch, where it mixes with blood coming in this artery. The small portion of blood that goes to the lungs returns to the left atria, where it joins with the blood passing through the foramen ovale. All the blood in the left atrium passes through the mitral valve into the left ventricle and is ejected to the ascending aorta. When it passes the aortic valve, a small amount of blood goes into the coronary arteries for the heart perfusion. The blood that finally arrives to the ascending aorta reaches the aortic arch where part of it is pumped to the brachiocephalic trunk and subclavian arteries to the head and upper extremities. Finally, the blood that is not going through these arteries continues its way and is mixed with the blood coming from the ductus arteriosus (from the pulmonary artery), that is poorly oxygenated, so the mixed blood that goes to the descending aorta is markedly oxygen decreased. This blood is finally distributed to the rest of the tissues and organs of the fetal lower body. Deoxygenated blood returns to the placenta via the umbilical arteries.

At birth, the umbilical cord is clamped and the baby no longer receives oxygen and nutrients from the mother. With the first breaths of life, the lungs begin to expand, and the ductus arteriosus and foramen ovale both close.

1.2.1 **Structure of the fetal heart**

The human heart is an organ that pumps blood throughout the body, supplying oxygen and nutrients to the tissues. The fetal heart consisted on 4 chambers: 2 atria and 2 ventricles, and 4 valves: two between the atria and the ventricles, named atrioventricular (AV) valves or tricuspid (right) and mitral (left) valves, and two more connecting the ventricles with the two ar-

1.2. The fetal circulation system

teries: the main pulmonary artery and the aorta (see Figure 1.2). They only allow exit of blood from the heart towards these vessels following ventricular contractions. The septum is a muscle wall that separates the two cardiac ventricles. The outer walls of the heart consists on four differentiated layers:

- **Pericardium:** a fibrous membrane that surrounds the heart.
- **Epicardium:** the outermost layer of the heart muscle. It is composed of fibrous tissue that surrounds the heart.
- **Myocardium:** the middle layer. It contains the muscle cells that contracts to pump the blood.
- **Endocardium:** the inner layer that contacts the blood. It is primarily made up of endothelial cells and controls myocardial function.

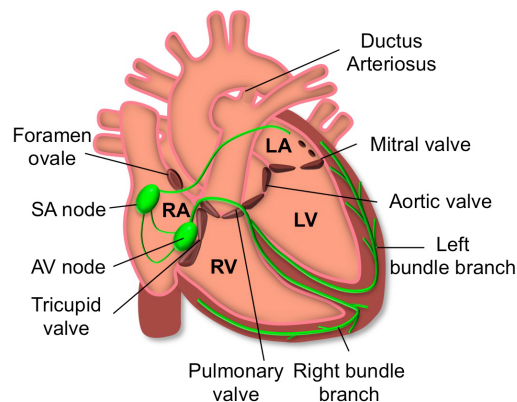


Figure 1.2: Structure and electrical conduction system of the fetal heart.

1.2.2 Electrical conduction system

The conduction system of the heart initiates and coordinates the electric signal that causes the rhythmic and synchronized contractions of the atria and ventricles. The sinoatrial node (SA node) located in the upper part of the right atrium generates an electrical stimulus, thanks to the SA self-excitatory cells, also known as *pacemaker* cells. This electrical stimulus travels through the conduction pathways in the atria until it arrives to the boundary between the atria and ventricles, where the atrioventricular node (AV node) is located (see Figure 1.2). Then, the AV node slows down the impulse for a very short period of time, and then sends it further through

the conduction pathways of the ventricles. This conduction system is composed of a common bundle and it splits into two bundle branches propagating along each side of the septum, constituting the right and left bundle branches. They provide the electrical stimulation to both ventricles. In fetuses, this electrical stimulus is generated 120-160 times per minute. The myocardium begins to contract rhythmically 3 weeks after conception, with a starting heart rate around 100-120 beat per minute (bpm). With further growth and maturation of the conduction system, including definition of the SA node, there is a subsequent increase in the heart rate to 170 bpm by 9-10 weeks of gestation, and then it gradually decreases to 130 bpm by term [13].

1.3 The cardiac cell

Cardiac muscle cells or cardiomyocytes are the contractile cells that make up the myocardium (Figure 1.3). Cardiomyocytes within the heart need to contract in unison in order to pump blood out efficiently from inside the cardiac chambers towards the different organs and tissues. The contraction of the individual cardiomyocytes is regulated by the different ion channels and exchangers that control Ca^{2+} entry into and out of the cell and the sarcoplasmic reticulum (SR). The cardiac action potential is initiated by depolarization of the sarcolemma and is kept on a plateau phase by the activation of voltage-gated L-type Ca^{2+} channels (Figure 1.4). Ca^{2+} entry via these channels triggers the Ca^{2+} release from the SR. This phenomenon is known as calcium induced-calcium release. Then, the amount of free Ca^{2+} inside the cytosol of the cell binds to the troponin-C and activates the myofilaments of the sarcomeres generating the cell contraction. This process is called excitation-contraction coupling. Cardiomyocytes are electrically coupled through the gap junctions, so the electrical stimulus is propagated from one cell to another allowing the ventricular/atrial cells to contract synchronously.

Sarcomeres are the elemental contractile units within a cardiomyocyte. Sarcomeres are composed of two different myofilaments of proteins: thick filaments of myosin and thin filaments of actin (Figure 1.4). Thin filaments of actin extend from Z-discs to the center of the sarcomere. In contrast, thick filaments of myosin lie at the center of the sarcomere and overlap the thin filaments. Z-discs form the boundaries of the sarcomere. The A-band is defined as the zone where actin and myosin filaments overlap. When Ca^{2+} ions bind with troponin-C molecules, the thin filaments of actin pull the thick filaments of myosin towards the center, and both filaments slide with respect to one and other, consuming ATP as source of energy. As a result, the Z-discs are pulled closer together and the sarcomere shortens. The contraction of a whole muscle fiber results from the simultaneous contraction

1.3. The cardiac cell

of all of its sarcomeres.

Finally, removal of the cytosolic Ca^{2+} is achieved by re-uptake into the SR via SERCA and also by the extrusion via the Na^+/Ca^{2+} exchanger (NCX). Then the cell relaxes and returns to its resting state.

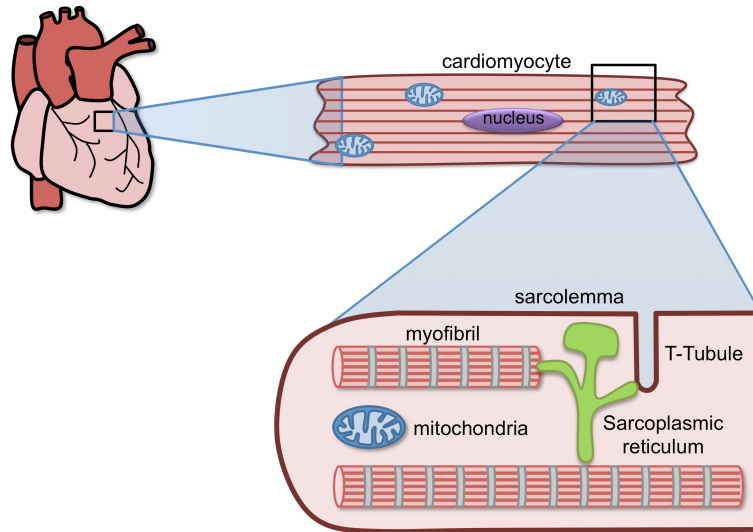


Figure 1.3: Structure of the cardiomyocytes, the cells that compose the myocardial wall within the heart.

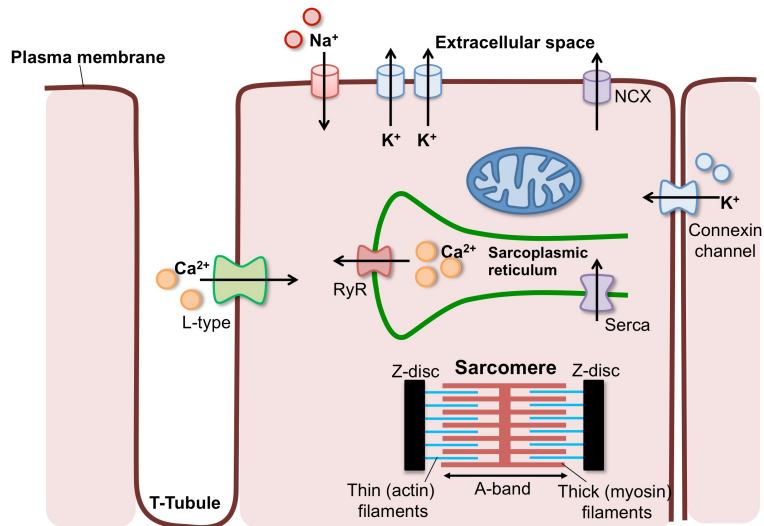


Figure 1.4: Cardiomyocyte architecture, intracellular organelles and ion channels involved in the cardiac excitation–contraction coupling.

1.4 Cardiovascular remodelling in IUGR and its postnatal persistence

Clinical and experimental studies have shown hemodynamic and cardiovascular functional and structural changes in utero [14, 15] that persist after birth [6] showing structurally remodelled and less efficient hearts in IUGR fetuses (see Figure 1.5). The experimental evidence in a cohort of human fetuses and children has been recently confirmed and demonstrated for the first time that cardiovascular remodelling in cases of IUGR persists postnatally [7]. IUGR children show significant changes in cardiac morphology (more globular hearts) (see Figure 1.5), a decrease of systolic ejection volume compensated by an increase in heart rate, and decreased myocardial longitudinal velocities. The more globular cavities decrease local wall stress given that pressure is increased. However, since the globular shape remains present after birth, this means that adaptation to acute pressure loading (in normal hearts partially compensated by going from an elliptical to a more globular shape) is partially lost making the individual more susceptible to future insults and increased cardiovascular risk in the long term. Significant changes in the vascular system has been also reported, such as increased blood pressure and increased intima-media wall thickness of the carotid arteries. The placental resistance increase in IUGR fetuses leads to higher blood pressures increasing the cardiac loading. This may lead to an increase in the arterial wall thickness and may be in the arterial stiffness too. These results indicate that cardiovascular remodelling is probably due to pressure and volume overload in an environment of chronic hypoxia/hyponutrition that may explain the apparent cardiac shape and functional changes.

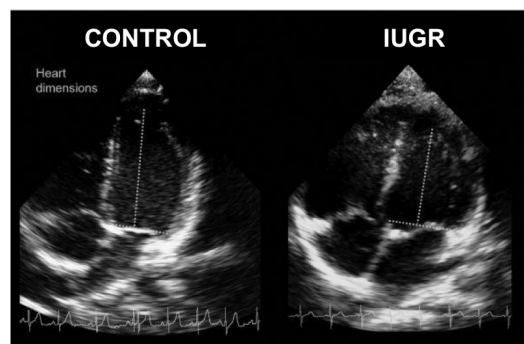


Figure 1.5: Two-dimensional apical 4-chamber views at end diastole illustrating the more globular cardiac shape in IUGR. Adapted from Crispi et al. [7].

1.4.1 Blood flow redistribution (brain sparing effect) in IUGR fetuses

Placental insufficiency is the major placental abnormality in IUGR fetuses, which has been associated with a reduction in delivery of oxygenated and/or nutrients to the fetus caused by the increase in the placental resistance. In response to this acute hypoxemia, fetuses redistributes its blood flow trying to protect and maintain an adequate oxygenated level in their more vital organs such as brain, heart and adrenal glands at expense of peripheral tissues. This compensatory mechanism is known as “brain-sparing-effect”. The term brain-sparing refers to relative protection of the brain as compared with other organs during fetal development, but this does not guarantee normal development after birth. This blood redistribution originated by the increase in the placental resistance may be associated with the apparent vasodilation observed in the cerebral and coronary arteries, and it allows the fetus to increase the blood flow to the brain and heart and consequently to decrease the blood flow to the lower body (see Figure 1.6).

This flow redistribution leads to significant changes in blood flow through the aortic isthmus (AoI), a segment of the aorta located between the left subclavian artery and the junction of the ductus arteriosus with the aorta. The AoI is also the only arterial segment that connects both ventricular outputs ejecting blood in parallel to the upper and the lower body of the fetus. Its unique disposition makes the AoI a good candidate for the assessment of the fetal hemodynamic condition. In systole, blood flow in the AoI depends both on left and right ventricular functions. The final systolic pattern of the AoI flow waveform is determined by the relative contributions of left and right ventricular stroke volumes as well as the balance between vascular impedances of the upper and lower body. In diastole, the direction of the flow essentially depends on balance between the upper and the lower body circulation. Under normal conditions, forward flow (from heart to the placenta) is present through the AoI, both in systole and diastole, because of the low lower body impedance. However, in altered conditions such as IUGR, placental resistance, which is normally the lowest in the whole fetal circulation, increases. This increase in placental resistance, together with the subsequent decrease in brain resistance due to cerebral vasodilation can reduce the forward diastolic flow in AoI and in more severe cases can lead to the reversal of the AoI flow during diastole and also in late-systole [16] (Figure 1.6).

The AoI (Doppler) blood flow velocity profile has a characteristic shape with a rapid systolic rise of the velocity, followed by a more gradual deceleration with a small reserval notch (in some cases) at the end of systole, with forward flow during diastole. Some studies [16–18] have reported that

1.4. Cardiovascular remodelling in IUGR and its postnatal persistence

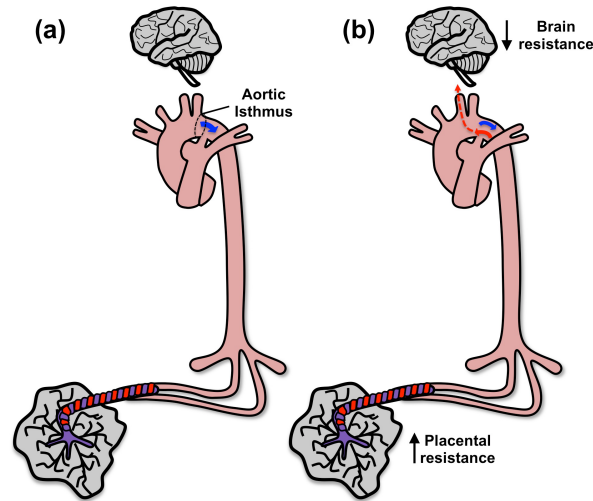


Figure 1.6: (a) Normal (forward) flow in the AoI. (b) Reversal flow in the AoI as a consequence of blood flow redistribution in IUGR.

this small notch starts to appear at 25-30 weeks of gestation approximately with a progressive increase with the advance of gestation, resulting in a brief peak of reversal flow at the end of systole/beginning of diastole. However, the origin of this reversed peak is unclear. Some authors [19] suggested that this brief peak of reversal flow at the end of systole is caused by a longer and late ejection of the right ventricle. However, on the other hand, Del Rio and colleagues considered this brief reversal of flow artifactual [20], since it was difficult to explain the detection of both forward and reversal flow at the same time and in the same arterial segment. Therefore, the origin of this end-systolic notch of the AoI is still not fully understood and needs to be further investigated.

1.4.2 Ultrastructural remodelling

IUGR is associated with cardiovascular remodelling, which persists into adulthood. Although the effects of IUGR on cardiac organ remodelling have been characterized, the underlying subcellular remodelling and cardiovascular programming events are still poorly documented. The cellular and molecular changes that are initiated in fetal life and persist as permanent features in youth and adulthood, are markers to evaluate the impact of any intervention aimed at preventing cardiovascular remodelling associated to fetal programming in IUGR.

At the ultrastructural level, molecular changes in the myocyte contractile machinery have been recently demonstrated [21–25], similar to those

1.4. Cardiovascular remodelling in IUGR and its postnatal persistence

described in dilated cardiomyopathy and diastolic heart failure. Gene expression of regulatory proteins of the sarcomere is altered in IUGR fetuses and this alteration persists in adult life [22, 25]. At the same time, IUGR sarcomere length is shorter compared to controls [21, 22, 24], may be due to structural changes in their key proteins (actin, myosin and/or tintin). Shorter sarcomeres have been also found in animal models of a variety of cardiac diseases [26–28]. Sarcomere structure is strongly related to sarcomere function and contraction force. Sarcomere length has an effect on actin-myosin cross-bridge recruitment. It is associated with the degree of thick-thin filament overlap, which affects the probability of actin-myosin cross-bridge formation and thus the capacity to generate force [29]. The permanent changes in sarcomere structure could be as well a response to the known sustained increase in fetal blood pressure that occurs in IUGR. Recent findings suggest that isolated neonatal cardiomyocytes undergo structural modifications within their myofibrils in response to changes in environmental stiffness, resulting in differences in resting sarcomere length [30].

The heart is an organ with high-energy requirements in the form of ATP to ensure proper blood pumping. Efficient energetic homeostasis depends on the correct arrangement of subcellular organelles. A close spatial interaction between mitochondria and the sarcomere contractile filaments is essential to ensure adequate and quick transportation of ATP. This is reached by the intracellular energetic units (ICEUs), which are structural and functional units, consisting of mitochondria located at the level of sarcomeres between Z-discs interacting with surrounding myofilaments, sarcoplasmic reticulum, cytoskeleton, etc. A recent study in an animal model of IUGR [23] has shown an association between IUGR and less organized intracellular arrangement of the cardiomyocyte organelles. The specific disarrangement of the ICEUs together with differences in the expression of key pathways for energy production suggest an impairment of the energetic metabolism under IUGR. This study provides evidence that IUGR fetal hearts show a less organized intracellular arrangement, characterized by an increased relative volume occupied by cytoplasm and a decreased relative volume occupied by mitochondria.

Several studies on cardiomyocytes from different animal species and human have provided quantitative evidence for regional spatial and temporal inhomogeneities in the subcellular regulation of Ca^{2+} release. Specifically, in pig ventricular cardiac cells, the areas of delayed Ca^{2+} release were related to regional absence of T-Tubules. The extensive T-tubular system of ventricular myocytes ensures a rapid and homogeneous increase in $[Ca^{2+}]$ throughout the cell. When the number of T-tubules is decreased, Ca^{2+} release is more inhomogeneous. The inhomogeneous distribution of Ca^{2+} release units leads to dyssynchronous Ca^{2+} release, and has been re-

1.5. Survey of the state of the art of computational models

lated to cardiomyocyte dysfunction in myocardial remodelling and heart failure [31, 32]. Additionally, another experimental study performed in pig, rat and human myocytes [33], have reported regional differences in the sub-cellular regulation of $[Ca^{2+}]$ decay in the cytosol during diastole. The rate of $[Ca^{2+}]$ decay varied between adjacent regions within the cardiomyocyte. A variety of processes are regulated by local cytosolic $[Ca^{2+}]$, and different rates of cytosolic $[Ca^{2+}]$ decay may result in dyssynchrony of local sarcomere re-lengthening. Indeed, the local time of sarcomere re-lengthening was highly correlated with the rates of cytosolic $[Ca^{2+}]$ decay. Dyssynchronous Ca^{2+} removal could potentially be explained by an inhomogeneous distribution of SERCA2a protein along the SR. Also the same authors stated that variability in time of $[Ca^{2+}]$ decay is related to the distribution of intracellular structures, such as mitochondria. They found that regions of fast $[Ca^{2+}]$ decay were more often associated with regions of increased mitochondrial signal density.

Inhomogeneities in Ca^{2+} re-uptake and also in the SERCA2 distribution have been also observed in fetal and neonatal cardiomyocytes of an animal model of IUGR (data not published). However T-tubules are absent in fetal and neonatal cardiac cells. The exact mechanisms responsible for these changes remain unknown and need to be further investigated. Changes in T-tubule structure and protein expression occurring during development may contribute to the functional changes observed in these conditions.

1.5 Survey of the state of the art of computational models

Many physiological relationships with regard to cell, tissue, organ, or the whole system can be described by a mathematical relation. Thus, patient characteristics may be simulated by a computer model, composed of a network of applied physiological relationships. By adjusting relevant parameters on the computer model, so that model simulation and measurements agree, we can obtain a patient-specific simulation, which can be used for further improvement of diagnosis and better planning of treatment. Patient-specific simulations require that a wide variety of measurements can be combined to estimate the mechanical and hemodynamic status of the cardiovascular system as a whole.

Specifically, in this thesis we will focus on computational/mathematical models of the fetal circulation as well as on electromechanical models of the cardiac cell.

1.5.1 Lumped models of the fetal circulation

Lumped models or Zero-dimensional (0D) models, based on simplified representations of the different parts of the cardiovascular system, can contribute strongly to our understanding of circulatory physiology. Lumped models allow the evaluation of the hemodynamic interactions among the different cardiovascular organs. These models assume a uniform distribution of the fundamental variables (pressure, flow and volume) within any particular compartment (organ, vessel or part of a vessel) of the model at any instant in time. However, the higher dimensional models recognize the spatial variation of these parameters too. Computational models constructed from 0D components generally feature the major components of the system, such as the heart, the heart valves and the different compartments of the vasculature, and are suitable for examination of global distributions of pressure, flow and blood volume over a range of physiological conditions, including the study of interactions between the modeled components. In these models, the concept of a hydraulic-electrical analogue is applied. Generally, blood flow in the circulatory system and electric conduction in a circuit have much similarity: blood pressure gradient in the circulatory loop drives the blood to flow against the hydraulic impedance; similarly, voltage gradient in a circuit drives current to flow against the electric impedance. Hydraulic impedance represents the combined effect of the friction loss, vessel wall elasticity and blood inertia in the blood flow, whereas electric impedance represents the combination of the resistance, capacitance and inductance in the circuits. In Table 1.1 the analogy between circulation and electric elements is described. In Figure 1.7 two electrical equivalent models are shown: one for arterial segments and the other, a three-element Windkessel model for vascular beds.

Table 1.1: Analogy between circulation and electrical elements in lumped 0D models.

Circulation	Electrical
Pressure ($P(t)$)	Voltage ($V(t)$)
Flow ($Q(t)$)	Current ($I(t)$)
Viscosity	Resistor (R)
Compliance	Capacitor (C)
Inertia	Inductor (L)

Some lumped models have been proposed to recreate and better understand the flow changes in the fetal circulation [34–40]. Some of these previous approaches to model the fetal circulation focused mainly on the materno-fetal circulation [34, 37, 38] or have only modeled the fetal circu-

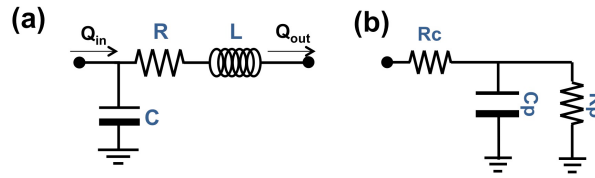


Figure 1.7: (a) Electrical equivalent model of an arterial segment and (b) a three-element Windkessel model of a vascular bed.

lation under normal conditions [35, 36]. However, the only reported studies focused mainly on fetal circulation and considering also pathological conditions did not include the aortic isthmus and ductus arteriosus [39, 40]. Another weak point from the models cited above is that they considered a single flow input with fixed values calculated from the literature instead of using patient-specific inputs (aortic and pulmonary blood flows) determined from real echocardiographic data (i.e. Doppler velocity waveforms from fetuses). Therefore, up to the starting of this thesis, no patient-specific lumped model of the fetal circulation, including the characteristics described above, was not published.

1.5.2 Electromechanical models of the cardiac cell

The study of myocardial function from analysis of single cardiac muscle cells have received an increased attention. Indeed, experiments performed in the isolated cell level enable an analysis of cardiomyocyte response to mechanical stress, as well as a visualization of cytosolic and nuclear calcium dynamics in contracting cardiac cells. Modelling cardiac cell electromechanical coupling is of particular importance because it enables the integration of comprehensive experimental data for cardiac cell structure and function and interactions between mechanical and biochemical/electrical processes within appropriate constitutive models. This can provide a relevant basis for prediction of cell contraction under different conditions. Also the analysis of cardiac cell response to mechanical stress may improve the understanding on various pathologies that alter the contractility of the cardiac tissue.

A rather large number of models of calcium-induced cardiomyocyte contraction have been proposed, with most recent publications incorporating a detailed description of the calcium kinetics together with different modules describing cell contraction. The first cellular model appeared in Nature in 1960 [41], where Denis Noble introduced the first mathematical and computational model of a cardiac Purkinje fibre cell, right through to 2004, when he presented a detailed model of human ventricular cardiomyocyte activity,

1.6. Hypothesis and Objectives

in collaboration with Ten Tusscher and Panfilov [42]. The papers published in last two decades about cellular models demonstrate in detail the progress that has been made in this area. They focus in some detail on a particular aspect of cardiac cell functionality, attempting to derive mathematical relationships, predominantly in the form of ordinary differential equations, which allow that computer simulations can reproduce experimental data. The most relevant contributions on modelling of ventricular myocyte activity were the following: Crampin et al. focused on the role of acidosis in cardiac electrophysiology and excitation–contraction coupling, presenting a modelling study of different effects to altered Ca^{2+} transients during acidosis [43]. Pásek et al. considered the role of T-tubules in the physiological modulation of electrical and contractile activity. To do this he developed a mathematical model of ventricular cardiomyocytes in which the cardiac T-Tubule system was described as a single compartment [44].

However, these models usually implemented the cell mechanical behaviour as phenomenological space-independent force–displacement relationships, instead of local stress–strain constitutive laws. Some electromechanical models of a cardiomyocyte based on the finite-element method that considered also the local stress-strain constitutive laws have been developed recently [45–47]. These models include all elementary processes involved in cardiomyocyte electrophysiology, contraction, and ATP metabolism. One of the most detailed one was the 3D electromechanical model published by Hatano et al. [45] that incorporated the T-Tubule network as well as the mitochondria, modelling the biological interaction between them.

Nevertheless, none of these cardiac cell models developed to date allow the study of the local structural and mechanical inhomogeneities of the cell, since in all of them, the different mechanical and elastic properties of the cardiac cell were assumed to be homogeneous in the whole cell. Therefore, in order to further investigate the local cell properties and also to evaluate the possible differences between healthy and IUGR cells, an electromechanical model of a cardiomyocyte that could reproduce the local inhomogeneities is needed.

1.6 Hypothesis and Objectives

In this thesis, we start from the hypothesis that computational models and image processing tools, based on an interdisciplinary approach, can improve the understanding of intra-uterine cardiac remodelling that takes place at different scales of the cardiovascular system of the fetus.

Therefore, the main goal of this thesis is to develop computational models and tools for the study of intra-uterine cardiac remodelling at vascular and also cellular level in fetuses with IUGR.

The specific objectives are:

- Regarding the vascular remodelling:
 1. To develop a simplified lumped model of the fetal circulation to study the blood flow redistribution in fetuses with IUGR, and to better understand the brain-sparing effect (addressed in *Chapter 2*).
 2. To use the implemented lumped model to study the evolution of the blood flow in the AoI through the pregnancy. Also to investigate the origins of the brief peak of reversal flow at late-systole in the AoI blood flow velocity waveform, observed in healthy fetus during the last trimester of gestation (addressed in *Chapter 3*).
 3. To extend the previous lumped model of the fetal circulation to obtain patient-specific hemodynamic vascular properties to better understand the underlying mechanisms of placental insufficiency. Also, to test the predictive capacity of the estimated patient-specific hemodynamic parameters in the prediction of adverse perinatal outcome (addressed in *Chapter 4*).
- And regarding the cellular remodelling:
 4. To develop and validate an automatic image processing tool to characterize the sarcomere distances in second-harmonic multi-photon images of cardiac tissue samples from hearts of an animal model of IUGR and also of human fetuses (addressed in *Chapter 5*).
 5. To develop a two-dimensional electromechanical model of a cardiomyocyte taking into account the local inhomogeneities and differences experimentally observed in cardiac cells that could explain the functional and structural differences observed between healthy and IUGR cells (addressed in *Chapter 6*).

CHAPTER **2**

A computational model of the fetal
circulation to quantify blood
redistribution in intrauterine growth
restriction

Abstract — Intrauterine growth restriction (IUGR) due to placental insufficiency is associated with blood flow redistribution in order to maintain delivery of oxygenated blood to the brain. Given that, in the fetus the aortic isthmus (AoI) is a key arterial connection between the cerebral and placental circulations, quantifying AoI blood flow has been proposed to assess this brain sparing effect in clinical practice. While numerous clinical studies have studied this parameter, fundamental understanding of its determinant factors and its quantitative relation with other aspects of hemodynamic remodelling has been limited. Computational models of the cardiovascular circulation have been proposed for exactly this purpose since they allow both for studying the contributions from isolated parameters as well as estimating properties that cannot be directly assessed from clinical measurements. Therefore, a computational model of the fetal circulation was developed, including the key elements related to fetal blood redistribution and using measured cardiac outflow profiles to allow personalization. The model was first calibrated using patient-specific Doppler data from a healthy fetus. Next, in order to understand the contributions of the main parameters determining blood redistribution, AoI and middle cerebral artery (MCA) flow changes were studied by variation of cerebral and peripheral-placental resistances. Finally, to study how this affects an individual fetus, the model was fitted to three IUGR cases with different degrees of severity. In conclusion, the proposed computational model provides a good approximation to assess blood flow changes in the fetal circulation. The results support that while MCA flow is mainly determined by a fall in brain resistance, the AoI is influenced by a balance between increased peripheral-placental and decreased cerebral resistances. Personalizing the model allows for quantifying the balance between cerebral and peripheral-placental resistances, thus providing potentially novel information to aid clinical follow up.

Adapted from: Garcia-Canadilla P, Rudenick PA, Crispi F, Cruz-Lemini M, Palau G, Camara O, Gratacos E, Bijns BH. *A computational model of the fetal circulation to quantify blood redistribution in intrauterine growth restriction*. PLoS Comput Biol, 10(6):e1003667, 2014

2.1 Introduction

Intrauterine growth restriction (IUGR), predominately due to placental insufficiency, is one of the main causes of perinatal mortality and morbidity [8,48], and defined as a birth weight below the 10th percentile for gestational age. IUGR fetuses, suffering from hypoxia and undernutrition, show Doppler changes in several arteries of the fetoplacental circulation such as umbilical artery (UA), middle cerebral artery (MCA), and also in the aortic isthmus (AoI). These changes are assessed in clinical practice to stage the severity of IUGR and are thought to reflect blood flow redistribution due to increased peripheral resistance, with decreased brain resistance in order to maximize brain blood supply under an adverse environment. In IUGR fetuses, AoI diastolic forward flow usually decreases and can become reversed in the more severe cases reflecting blood redistribution from the ductus arteriosus towards the brain instead of the periphery. Reverse flow in the AoI is associated with worse perinatal and neurodevelopmental outcome [49–53]. However, which remodelling or redistribution processes in the cardiovascular system induce the observed changes in AoI flow in IUGR fetuses is not fully understood. It has been proposed that cerebral vasodilation plays a major role in decreasing diastolic flow in the AoI [54]. However, other clinical studies suggested that AoI flow pattern is influenced by simultaneous changes in both cerebral and peripheral-placental resistances [19,52,55,56]. Moreover, some experimental studies in an ovine animal model [57–59] have quantified the influence of placental resistance increase in the AoI flow, showing a strong correlation between the increase in the placental resistance and the amount of diastolic reversal flow in the AoI. However, the cerebral vasodilation occurring as response to fetal hypoxemia also influences the flow patterns in the AoI, and this influence could not be isolated from those changes caused by the increase in placental resistance.

Therefore, it would be of interest to be able to estimate the separate influence of the individual contributors, such as the cerebral vasodilation and placental resistance increase, on the AoI flow. This can further improve the understanding of the flow changes in IUGR and provide more targeted assessment of flow redistribution. For this, lumped computational models have been proposed to recreate and better understand hemodynamic changes in the fetal circulation [34–40]. These models are based on the idea that the flow in a tube is analogous to the current in an electrical circuit and flow properties such as viscosity, inertia and compliance can be modeled with resistors, inductors and capacitors respectively. Hence, the different parts of the fetal circulation, such as arteries or vascular beds, can be modeled with a set of electrical components. The parameters of the electrical components are calculated based on the cardiovascular system's physical properties and

dimensions together with physiological and imaging measurements, where possible. Thus, an equivalent electric circuit of the fetal circulation can be obtained. Computational models have the advantage that they enable to evaluate the effects of changes in individual parameters on the total system performance. For example, the influence of changes in placental and/or brain resistance on the AoI flow can be evaluated separately, which cannot be performed in a clinical or experimental setting.

Previously published models of the fetal circulation focused either on the materno-fetal circulation, studying oxygen exchange [38] [34,37]; only focused on the fetal circulation under normal conditions [35,36]; lack the full complexity of the fetal circulation (such as the ductus arteriosus) to study the flow redistribution in the places connecting the specific segments present [37,40]; or have used a simplified and non-measured and personalized flow waveform at the entrance of the aorta and pulmonary artery [39] [40,60].

Therefore, we developed an extended lumped model of the fetal circulation, including all relevant components to study flow redistribution in IUGR that additionally can be tuned towards an individual fetus when blood flow measurements are available. This model was further used to help in better understanding the hemodynamic changes induced by altered conditions in the brain circulation, including the AoI and the MCA. The model was calibrated and validated using clinical measurements from a healthy control fetus. Next a parametric study was performed to specifically evaluate contributors to flow changes in the AoI and cerebral arteries (CA). Finally, the model was personalized with clinical data from three IUGR cases with different degrees of severity in order to show the individual contributors to flow redistribution.

2.2 Methods

2.2.1 Study individuals

In order to calibrate and validate the accuracy of the fetal circulation model, and to show its potential for personalization, clinical and Doppler data from one control and three IUGR fetuses with different degrees of severity were included. Eligible cases were singleton pregnancies that were selected from women who attended the Maternal-Fetal Medicine Department at Hospital Clínic de Barcelona. The study protocol was approved by the local Ethics Committee and patients provided written informed consent. IUGR was defined as an estimated fetal weight [61] and confirmed birth weight below the 10th percentile according to local reference curves [62] together with a pulsatility index (PI) in the UA above 2 standard deviations [63]. IUGR fetuses

2.2. Methods

were classified in stages of severity based upon the end-diastolic flow (EDF) in the UA as: present (PEDF), absent (AEDF) or reversed (REDF) [10]. We selected one IUGR representative of each severity stage.

All IUGR cases and the control fetus underwent an ultrasonographic examination between 31-34 weeks of gestation using a Siemens Sonoline Antares machine (Siemens Medical Systems, Malvern, PA, USA) which included estimation of fetal weight, standard obstetric Doppler evaluation and fetal echocardiography. Fetal echocardiography included the evaluation of flow velocities in the UA, MCA, AoI, ductus arteriosus and ascending aorta (only in the control fetus). The UA was evaluated in a free loop of the umbilical cord. The MCA was measured in a transverse view of the fetal skull at the level of its origin from the circle of Willis [64]. The cerebroplacental ratio was calculated by dividing MCA and UA PI [63]. PI was calculated as: systolic velocity minus diastolic velocity divided by time-averaged maximum velocity. Ductus arteriosus and AoI flow velocities were obtained either in a sagittal view of the fetal thorax with a clear visualization of the aortic arch or in a cross section of the fetal thorax at the level of the 3-vessel and trachea view [20]. The AoI flow velocity was quantified by measuring the AoI PI and flow index (IFI). The IFI was calculated as: (systolic + diastolic)/systolic velocity integrals. Aortic inflow velocity was imaged in an apical or basal 5-chamber view of the heart, and pulmonary artery inflow velocity was obtained in a right ventricular outflow tract view. Peak systolic velocities of both aortic and pulmonary artery inflows, ejection time and heart rate were measured. The diameters of the aortic and pulmonary valves were measured in frozen real-time images during systole by the leading-edge-to-edge method [65]. Additionally, Doppler recording from the ascending aorta was obtained in the control fetus. The angle of insonation was kept as close as possible to 0° and always below 30° . Doppler data are shown as crude values and z-scores by gestational age according to previously published normal values [10, 18, 20, 64]. Upon delivery, gestational age, birth weight, birth weight centile, mode of delivery, Apgar scores, presence of preeclampsia and length of stay at the neonatal intensive care unit were recorded.

2.2.2 Lumped model of the fetal circulation

Building blocks

The equivalent electrical lumped model of the fetal circulation was constructed using two main building blocks (Figure 2.1(b)): arterial segments and peripheral vascular beds. The block describing the arterial segments included the local resistance of blood due to blood viscosity, modeled with

a resistor (R), the arterial compliance modeled with a capacitor (C) and the blood inertia modeled with an inductor (L), as previously described in other cardiovascular models [40, 66, 67]. The component parameters (R , L , C) of each of the blocks modelling the different arterial segments were calculated according to their physical dimensions and properties, using the following equations: $R = 8\mu l/\pi r^4$, $L = \rho l/\pi r^2$ and $C = 3\pi r^3 l/2Eh$, where l and r are the length and the radius of the arterial segment, μ is the blood viscosity calculated as $\mu = (1.15 + 0.075 * GA)/100$ [40] where GA is the gestational age in weeks, ρ the blood density ($1.05g \cdot cm^{-3}$), h the wall thickness, assumed to be 15% of the arterial radius (r) [40], and E the Young's Modulus estimated from Myers and Capper [39] for the different arterial segments.

The block describing peripheral vascular beds consisted of a three-element Windkessel model. Its electrical analog circuit includes a resistor in series with a capacitor and a resistor in parallel. In the model, the series resistor R_c is chosen to equal the characteristic impedance of the feeding artery at high frequencies to avoid reflections at high frequencies. The parallel resistor R_p accounts for the organ peripheral resistance and the parallel capacitor C_p for the organ compliance. Additionally, a unique resistor was chosen to model the flow from the ascending aorta into the coronary arteries.

Anatomical configuration

The simplified fetal circulation was modeled as a set of 14 arterial segments, including the ductus arteriosus connecting the left and right circulation in the fetus, and 8 vascular beds, as shown in (Figure 2.1(a)). The peripheral vascular bed represents the combination of the fetal lower body and the placenta. Our preliminary model [60] only included 6 arterial segments and 3 simplified vascular beds, considering a unique upper body artery, but it was too limited to study the cerebral flow changes and for this reason the main upper body and cerebral arteries were included in the current model. The physical dimensions and properties of the different arterial segments were extracted from the literature [39] [68] [69–79] and are listed in Table 2.1. The AoI was considered to be 20% of the total length of the ascending aorta and aortic arch, with a diameter equal to the distal aortic arch. Ductus arteriosus diameter was considered 1.12 times larger than AoI diameter according to [70]. Right and left pulmonary artery length were considered 1.4 times smaller than main pulmonary artery according to [69]. Finally, according to [68] the brachiocephalic trunk diameter was considered 1.46 larger than the subclavian arteries, the right and left subclavian arteries were equals, right common carotid artery was 1.25 times larger than the left common carotid artery, the internal carotid artery length was equal to the common carotid artery length, and the its diameter was 1.17 times smaller than

2.2. Methods

the common carotid artery diameter.

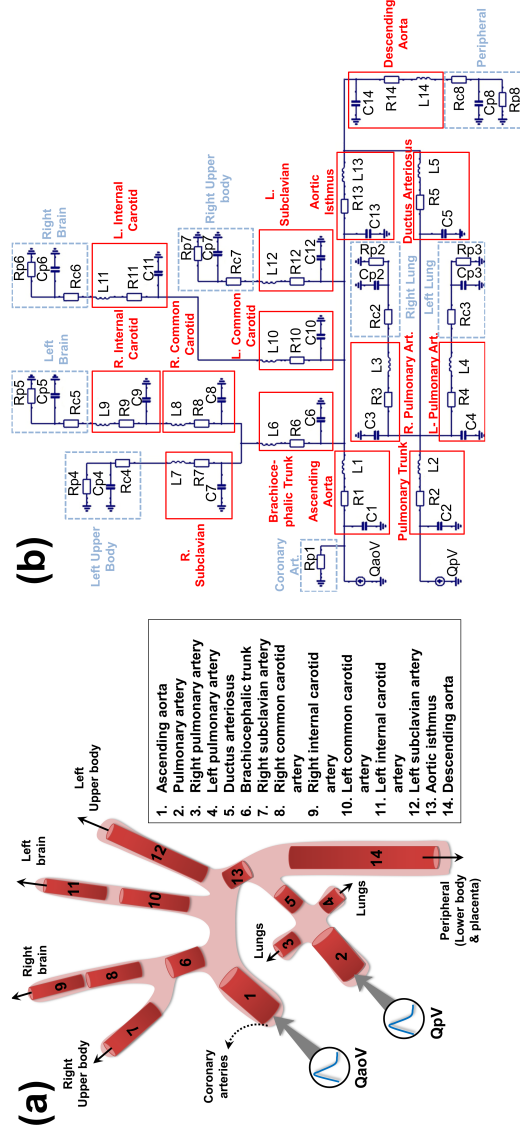


Figure 2.1: (a) Anatomical configuration composed of 14 arterial segments and 8 vascular beds: (1) right and (2) left upper body, (3) right and (4) left brain, (5) right and (6) left lung, (7) peripheral and (8) coronary arteries. Qaov and Qpv represent the aortic (left) and pulmonary (right) inflows respectively. (b) Electric circuit of the lumped model. The 14 blocks corresponding to the 14 arterial segments are highlighted in solid lines and include 1 resistor (R), 1 capacitor (C) and 1 inductor (L). The 8 blocks of vascular beds are highlighted in dashed lines and they consist of a resistor R_c in series with a capacitor C_p in parallel with a resistor R_p .

Table 2.1: Equations describing vessel's length and diameter as a function of gestational age (GA) in weeks, and Young's modulus (E) parameter for the 14 arterial segments included in the model.

Vessel	Length (mm)	Diameter (mm)	$E(\text{dyn}/\text{cm}^2)$
Ascending Aorta	$-8.61 + 0.88 \cdot GA$	$-2.10 + 0.27 \cdot GA$	$7.5 \cdot 10^5$
Aortic Isthmus	$-2.15 + 0.22 \cdot GA$	$-1.86 + 0.19 \cdot GA$	$7.5 \cdot 10^5$
Descending Aorta	$-34.25 + 3.57 \cdot GA$	$-2.22 + 0.22 \cdot GA$	$9.0 \cdot 10^5$
Ductus Arteriosus	$-2.41 + 0.31 \cdot GA$	$-2.09 + 0.21 \cdot GA$	$13.5 \cdot 10^5$
Main pulmonary artery	$-5.60 + 0.57 \cdot GA$	$-2.77 + 0.30 \cdot GA$	$7.5 \cdot 10^5$
R. pulmonary artery	$-4.00 + 0.41 \cdot GA$	$-1.71 + 0.18 \cdot GA$	$7.5 \cdot 10^5$
L. pulmonary artery	$-4.00 + 0.41 \cdot GA$	$-1.95 + 0.19 \cdot GA$	$7.5 \cdot 10^5$
Brachiocephalic Trunk	$-1.06 + 0.29 \cdot GA$	$-1.78 + 0.18 \cdot GA$	$7.5 \cdot 10^5$
L. subclavian artery	$-2.15 + 0.43 \cdot GA$	$-1.22 + 0.12 \cdot GA$	$9.0 \cdot 10^5$
R. subclavian artery	$-2.15 + 0.43 \cdot GA$	$-1.22 + 0.12 \cdot GA$	$9.0 \cdot 10^5$
L. Common Carotid artery	$-9.69 + 1.59 \cdot GA$	$-1.52 + 0.14 \cdot GA$	$9.0 \cdot 10^5$
R. Common Carotid artery	$-8.25 + 1.36 \cdot GA$	$-1.52 + 0.14 \cdot GA$	$9.0 \cdot 10^5$
L. Internal Carotid artery	$-8.25 + 1.36 \cdot GA$	$-1.22 + 0.11 \cdot GA$	$13.5 \cdot 10^5$
R. Internal Carotid artery	$-8.25 + 1.36 \cdot GA$	$-1.22 + 0.11 \cdot GA$	$13.5 \cdot 10^5$

$1 \text{ dyn} = 1 \text{ g} \cdot \text{cm} \cdot \text{s}^{-2}$. R, L denotes right and left respectively.

Equivalent electrical lumped model

The equivalent electrical lumped model of the fetal circulation was implemented in Simulink, *MATLAB (2013b, The MathWorks Inc., Natick, MA)*. It consists of a total of 64 electrical components (29 resistances, 21 capacitors and 14 inductors) and 2 inputs. The overall electrical circuit is displayed in Figure 2.1(b).

The electrical components of the blocks modelling the arterial segments were set up with the values calculated from the equations described in the first section, taking into account the physical properties listed in Table 2.1 and adjusted according to the gestational age of the fetus.

Due to the difficulty of measuring organ resistances and compliances in human fetuses, we used published data from other studies to calculate the different organ peripheral resistances (R_p) and compliances (C_p). Specifically, R_p were taken from Guettouche et al. [69] and adjusted to obtain a mean arterial blood pressure (MBP) appropriate to the gestational age of the fetus calculated as: $MBP(\text{mmHg}) = 0.87 \cdot GA + 10.33$ [80], where GA denotes the gestational age in weeks. The initial values of the organ compliances C_p were estimated from Pennati et al. [36] and van den Wijngaard et al. [40] and then they were adjusted. Details about the adjustment of peripheral resistances and compliances values are included in the following sections.

2.2. Methods

Boundary conditions

To provide the output of the heart as input boundary condition of the computational model, the measured aortic and pulmonary artery Doppler inflow velocities from the control and IUGR fetuses were used. Maximum blood velocities were delineated from spectral Doppler images using a custom program implemented in MATLAB, providing the peak blood velocity functions in aortic and pulmonary valves (V_{aoV} , V_{pV}). The final blood flow inputs (Q_{aoV} , Q_{pV}) were calculated as: $Q_{aoV} = V_{aoV} \cdot \pi \cdot r_{aoV}^2$ and $Q_{pV} = V_{pV} \cdot \pi \cdot r_{pV}^2$, where r_{aoV} and r_{pV} are the corresponding valve radius (aoV = aortic valve, pV = pulmonary valve).

As the fetal circulation model is not closed, venous pressure was considered 0 mmHg and therefore all the peripheral resistors and capacitors were connected to ground.

2.2.3 Simulations

Calibration of the equivalent lumped model in normal conditions

Firstly, in order to calibrate our computational model of the fetal circulation in a healthy situation, all the circuit component parameters were set up with the values calculated as indicated in the previous sections, using the data from the control fetus (gestational age and fetal weight). Accordingly, aortic and pulmonary inflows, measured with Doppler imaging of the control fetus, were used as input functions. Model-based waveforms from AoI, CA, ductus arteriosus and ascending aorta were compared to the measured ones at these locations. The PI (PI_{AoI}), IFI and percentage of reversed flow in the AoI, and also the PI in CA (PI_{CA}) and in descending aorta (PI_{dAo}) were calculated from model-based waveforms. Finally, the amount of blood flow that was distributed towards different fetal areas, including (1) the brain, (2) the upper body, (3) the lungs, (4) the lower body and placenta and (5) the coronary arteries was calculated as the percentage of combined cardiac output (CCO) and compared with data obtained from the literature [56, 81, 82]. CCO was calculated as the sum of right and left cardiac outputs.

The overall total vascular bed resistance was adjusted to obtain a *MBP* of 40 mmHg corresponding to a healthy fetus of 33.2 weeks of gestational age. Then, each peripheral vascular bed resistances (R_p) were adjusted so the percentage of blood flow towards each vascular bed was within its normal range of values according to the reported data [56, 81, 82].

Regarding the peripheral vascular bed compliances C_p , the initial values obtained from the literature [36, 40] were too high and reliable waveforms could not be obtained. Therefore, C_p values were estimated automatically using a constrained nonlinear optimization algorithm minimizing the rela-

tive error between the computed (denoted by \sim) and measured PI_{AoI} and PI_{CA} , implemented in MATLAB. An objective function J was therefore defined as the sum of both relative errors as: $J = |(\tilde{PI}_{AoI} - PI_{AoI})/PI_{AoI}| + |(\tilde{PI}_{CA} - PI_{CA})/PI_{CA}|$. Hence, the estimation problem consisted on searching the parameters set which minimizes J . This process was performed iteratively until the objective function J was less than a predefined value. The initial parameter set was chosen randomly within a physiological range. In order to avoid local minimum solutions, we repeated the procedure several times with different initial parameter sets, and we finally chose the parameter set with a minimum value of J . This way, the measured Doppler waveforms from the control fetus could be reproduced.

Parametric study of flow changes in the AoI and CA

Next, in order to evaluate how the increase in peripheral resistance (due to placental resistance increase and peripheral vasoconstriction) and how the cerebral vasodilation influences the blood flow redistribution, peripheral resistance ($Rp8$ of the electrical circuit of Figure 2.1(b)) was systematically increased up to a four-fold increase to simulate an increased placental resistance and peripheral vasoconstriction, and brain resistance ($Rp5$ and $Rp6$ of the electrical circuit of Figure 2.1(b)) was systematically decreased up to a four-fold decrease to represent cerebral vasodilation, keeping the remaining parameters unchanged. This range of resistance increase and decrease was chosen wide enough to cover all the possible physiological values both in normal and pathological conditions. In each simulation, IFI, PI and percentage of reversed flow in the AoI were calculated. Also, the PI_{CA} and PI_{dAo} were calculated and the PI_{dAo}/PI_{CA} ratio was obtained. Finally, the percentage of blood flow towards the brain and lower body and placenta was calculated to assess blood flow redistribution as a consequence of brain and peripheral resistance variation.

Patient-specific modelling

Finally, the model was personalized to the three fetuses at different severity stages of IUGR. For this, the model was initialized with the specific blood inflow functions measured from each IUGR fetus. The gestational age and fetal weight of each fetus were used to compute the model parameters. Specifically, the physical dimensions of all arterial segments were calculated following the equations shown in Table 2.1, taking into account the gestational age of each individual. The Young's modulus of the different arterial segments was not changed. Then, in order to describe the changes of length and diameter of the fetal arterial segments as a func-

2.3. Results

tion of fetal body weight, we scaled all the arterial dimensions according to the allometric equation: $Y_i = Y_0(W_i/W_0)^{0.33}$ as described by Pennati et al. [83], where W_0 is the reference weight calculated using the relationship between fetal weight and gestational age described by Gallivan et al. [84]: $\log_{10}(W_0) = 0.2508 + 0.1458 \cdot GA - 0.0016 \cdot GA^2$, where GA is the gestational age in weeks, W_i is the estimated fetal weight of the IUGR fetuses (see Table 2.2), Y_0 the reference arterial dimension calculated previously, and Y_i the scaled arterial dimension for the estimated fetal weight W_i . Vascular bed resistances and compliances were also scaled using the allometric equations: $R_p = R_{p0}(W_i/W_0)^{-1.0}$ and $C_p = C_{p0}(W_i/W_0)^{1.33}$ according to [83], where R_{p0} and C_{p0} were the vascular bed resistances and compliances calculated for the control fetus, respectively. Moreover, as R_{p0} values were calculated to obtain a MBP of 40 mmHg, corresponding to a fetus of 33.2 weeks of gestational age, the vascular bed resistances were also scaled to obtain a MBP appropriate for each IUGR fetus.

All these parameters were calculated for a healthy individual. However, in IUGR fetuses, some of them can be altered, such as brain and peripheral resistances. Additionally, due to the lack of data of organ compliances in human fetuses (the values reported by Pennati et al. [36] and van den Wijngaard et al. [40] were estimated from fetal sheep circulation) we decided to include them also in the set of parameters that need to be estimated. Therefore we defined a set of 6 model parameters to estimate: (1) brain and (2) peripheral resistances, and (3) brain, (4) upper body, (5) peripheral and (6) lungs compliances. To estimate these parameters we used the same constrained nonlinear optimization algorithm explained in the calibration section.

Finally, after retrieving the patient-specific parameters set, the individual IFI, PI and percentage of reversed flow in the AoI, PI_{CA} , PI_{dAo}/PI_{CA} and percentage of CCO towards to the brain and lower body and placenta were obtained.

2.3 Results

2.3.1 Characteristics of the study individuals

Ultrasonographic and perinatal data are shown in Table 2.2. As expected, IUGR cases showed a higher UA PI and AoI PI, together with lower MCA PI, cerebroplacental ratio and IFI values as compared to the control fetus. Also, as expected, IUGR cases delivered earlier and had lower birthweight and birthweight centile as compared with the control fetus. There were no perinatal deaths with the exception of the most severe IUGR case (REDF) who died in utero. Figure 2.2 shows the real measured flow velocity wave-

2.3. Results

forms in UA, MCA and AoI for the control and the 3 IUGR fetuses. Reversed diastolic flow in the AoI can be appreciated in IUGR cases with AEDF and REDF.

Table 2.2: Prenatal ultrasound and perinatal characteristics of the study population

	CONTROL	IUGR UA-PEDF	IUGR UA-AEDF	IUGR UA-REDF
Ultrasound data				
Gestational age at scan (weeks.days)	33.2	33.6	31.3	30.2
Estimated fetal weight (g)	2250	1500	950	500
Estimated fetal weight centile	77	< 1	< 1	< 1
Aortic inflow peak velocity ($cm \cdot s^{-1}$)	91	91	62	57
Pulmonary inflow peak velocity ($cm \cdot s^{-1}$)	67	87	58	47
Aortic valve diameter (mm)	6.0	6.0	5.0	3.2
Pulmonary valve diameter (mm)	6.6	7.1	7.5	5.7
Heart rate (bpm)	128	159	154	144
Umbilical artery PI	0.83	1.93	2.22	3.36
Umbilical artery PI (z-score)	-0.46	3.24	4.04	7.74
Umbilical artery end-diastolic flow	Present	Present	Absent	Reversed
Middle cerebral artery PI	2.82	1.54	1.45	1.18
Middle cerebral artery PI (z-score)	2.36	-1.05	-1.52	-2.30
Cerebroplacental ratio	3.40	0.80	0.65	0.35
Cerebroplacental ratio (z-score)	3.24	-2.89	-4.82	-3.62
Aortic Isthmus PI	3.39	4.25	6.19	27.96
Aortic Isthmus PI (z-score)	1.55	3.64	9.12	69.03
Isthmus flow index	1.36	1.26	0.52	-12.36
Isthmus flow index (z-score)	0.85	0.06	-6.64	-128.27
Perinatal outcome				
Gestational age at delivery (weeks.days)	39.3	34.6	31.5	30.3
Birth weight (grams)	3630	1648	1060	500
Birth weight centile	87	< 1	< 1	< 1
Gender	Female	Male	Male	Female
Fetal death	No	No	No	Yes
Cesarean section	No	No	Yes	Yes
5-minute Apgar score	10	10	8	-
Umbilical artery pH	7.28	7.28	7.20	-
Preeclampsia	No	No	No	Yes
Days in neonatal intensive care unit	0	15	10	-

IUGR, intrauterine growth restriction; UA, umbilical artery; PEDF, present end-diastolic flow; AEDF, absent end-diastolic flow; REDF, reversed end-diastolic flow; PI, pulsatility index.

2.3. Results

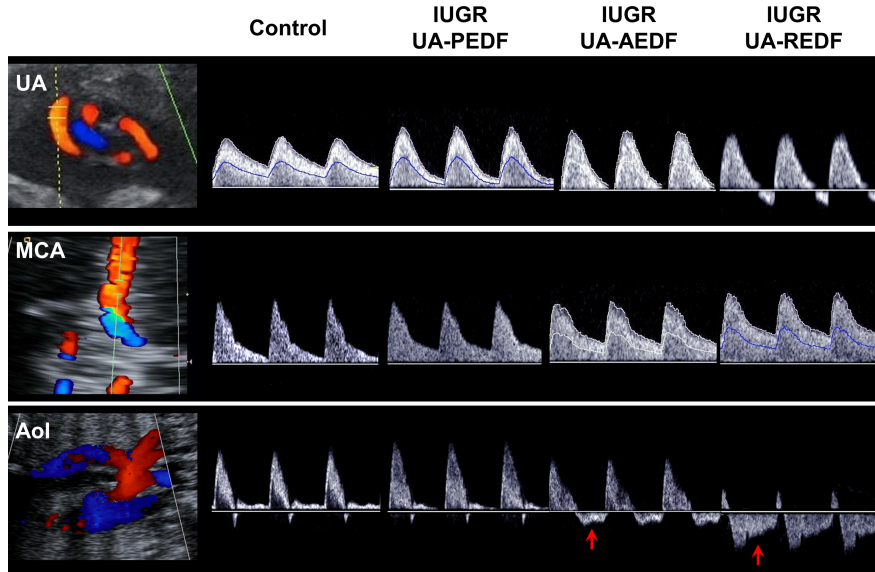


Figure 2.2: Doppler recordings from umbilical artery (UA) (top), middle cerebral artery (MCA) (middle) and aortic isthmus (AoI) (bottom) for the control and the three intrauterine growth restricted (IUGR) fetuses with present (PEDF), absent (AEDF) or reverse (REDF) umbilical artery end-diastolic flow. Red arrows indicated reversal flow in the AoI.

2.3.2 Calibration of the equivalent lumped model in normal conditions

Model-based and measured flow waveforms from the aortic and pulmonary inflows, ascending aorta, AoI, MCA and ductus arteriosus of the control fetus after calibration are displayed in Figure 2.3 highlighting their similarity. The model-based pressure waveform is displayed in the same figure (Figure 2.3(g)). Furthermore, we confirmed that the amount of blood flow distributed towards each vascular bed was within the range of normal values, as shown in Table 2.3. The parameters values of the vascular bed resistances and compliances are listed in Table 2.4.

2.3.3 Parametric study of flow changes in the AoI and CA

Figure 2.4 displays model-based AoI and CA traces for different combinations of peripheral and brain resistance values, modelling different severity degrees of IUGR. It shows that as peripheral resistance increases and/or brain resistance decreases, late-systolic and diastolic flow in the AoI is reversed while blood flow in the CA increases. The amount of reversal flow

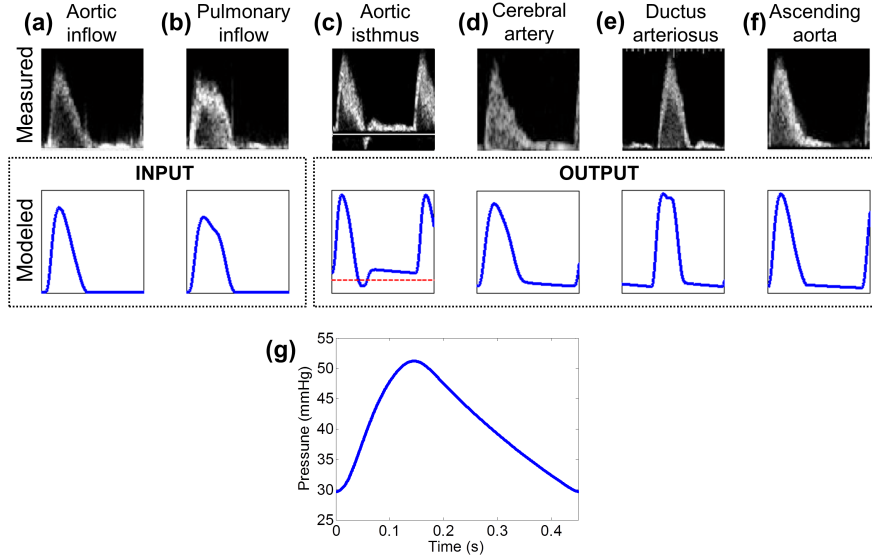


Figure 2.3: Comparison between measured and model-based blood flow waveforms in (a) aortic inflow (used as left input in our model (Q_{aoV})), (b) pulmonary inflow (used as right input in our model (Q_{pV})), (c) aortic isthmus, (d) cerebral arteries, (e) ductus arteriosus and (f) ascending aorta. Dashed line indicates a blood flow of $0 \text{ ml} \cdot \text{s}^{-1}$. (g) Model-based pressure waveform.

Table 2.3: Comparison between reported and model-based combined cardiac output (CCO) distribution in a control fetus of 33 weeks of gestational age.

	Reported CCO*	Model-based CCO
Anatomical segment		
Left cardiac output	40-60%	46%
Right cardiac output	60-53%	54%
Brain	15-16%	16%
Upper body	10-14%	11%
Lungs	13-25%	15%
Lower body & placenta	50-60%	52%
Coronary arteries	3-5%	4%

* As reported in the literature.

in the AoI (Figure 2.5(a)-(b)), PI in the AoI (Figure 2.5(c)-(d)) and IFI (Figure 2.5(e)-(f)) were plotted as a function of brain and peripheral resistances relative to their normal value. Both the individual increase in peripheral resistance and decrease in brain resistance seem to have similar effects on the AoI flow. PI_{CA} and the ratio PI_{dAo}/PI_{CA} were plotted in Figure 2.6 as a function of brain and peripheral resistances relative to their normal value. In the case of the CA, the decrease in brain resistance seems to have a big-

2.3. Results

ger influence on decreasing PI_{CA} than the increase in peripheral resistance (Figure 2.6(b)). Regarding PI_{dAo}/PI_{CA} , up to a two-fold increase/decrease in peripheral/brain resistance, its relation with the corresponding resistance variation is similar (Figure 2.6(d)). The increase in percentage of CCO towards the brain depends mainly on the reduction of brain resistance rather than peripheral changes, as shown in the graphs plotted in Figure 2.6(e). However the reduction of the amount of blood flow towards the lower body and the placenta was mainly produced by the increase in the peripheral resistance.

Table 2.4: Values of the initial peripheral resistances and estimated compliances of the 8 vascular beds used to model the control and 3 IUGR fetuses. The estimated brain and peripheral resistances after the nonlinear optimization algorithm are also displayed for the IUGR fetuses.

	CONTROL	IUGR UA-PEDF	IUGR UA-AEDF	IUGR UA-REDF
Peripheral Resistance (R_p) ($mmHg \cdot s \cdot ml^{-1}$) (initial values)				
Brain (Rp5-Rp6)	33.87	50.90	60.39	98.71
Upper body (Rp4-Rp7)	46.44	74.20	88.04	143.89
Lungs (Rp2-Rp3)	34.52	55.14	65.43	106.93
Peripheral (Rp8)	3.75	7.49	8.89	14.54
Coronary Arteries (Rp1)	68.75	109.33	130.31	212.98
Estimated Peripheral Compliances (C_p) ($ml \cdot mmHg^{-1}$)				
Brain (Cp5-Cp6)	0.0104	0.0052	0.0046	0.0024
Upper body (Cp4-Cp7)	0.0121	0.0083	0.0047	0.0017
Lungs (Cp2-Cp3)	0.0049	0.0038	0.0055	0.0011
Peripheral (Cp8)	0.0602	0.0242	0.0208	0.0049
Estimated Peripheral Resistances (R_p) ($mmHg \cdot s \cdot ml^{-1}$)				
Brain (Rp5-Rp6)	-	46.76	46.87	57.70
Peripheral (Rp8)	-	9.02	16.81	54.42

The name of the corresponding electrical component of the circuit displayed in Figure 2.1(b) is written in brackets.

2.3.4 Patient-specific modelling

The comparison between the measured and the patient-specific fitting of the AoI and CA blood waveforms are displayed in Figure 2.7(a)-(f) showing similar measured and model-based flow waveforms. Table 2.4 shows the values of vascular bed resistances and compliances and also the estimated peripheral and brain resistances after fitting for all individuals in the study. Table 2.5 shows the model-based parameters' values obtained for the four fetuses, which are similar to the clinical measurements shown in Table 2.2. The relative increase and decrease in peripheral and brain resistance respec-

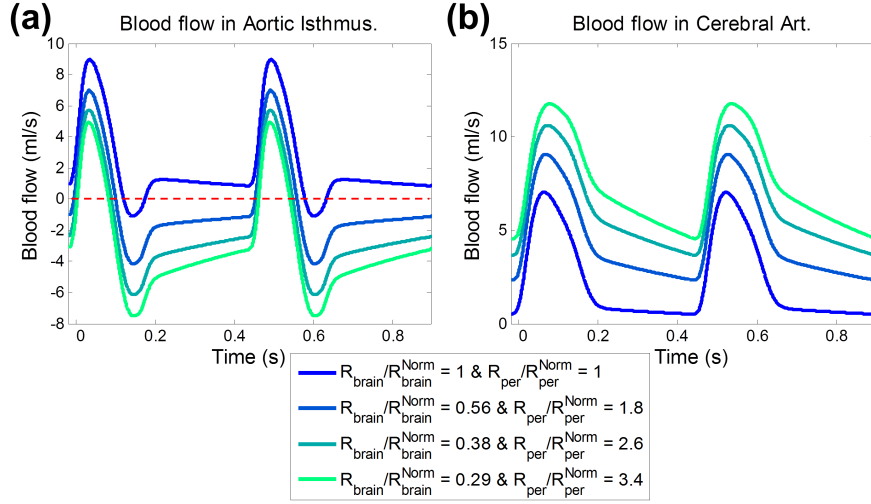


Figure 2.4: Model-based flow waveforms in the (a) aortic isthmus and (b) cerebral arteries for different degrees of peripheral and brain resistance changes. R_{per} and R_{brain} represent the peripheral and brain resistances respectively, and R_{per}^{Norm} and R_{brain}^{Norm} are their corresponding normal values. Dashed line indicates a blood flow of $0 \text{ ml} \cdot \text{s}^{-1}$.

tively, estimated for each modeled case is plotted in Figure 2.7(g). In the IUGR fetus with UA-PEDF, the peripheral resistance was increased by 20% ($\times 1.2$) while brain resistance remained almost equal ($\div 1.08$). In the most severe IUGR case, the peripheral resistance increased 274% ($\times 3.7$) with -41% ($\div 1.7$) decrease of brain resistance. Therefore, in all three IUGR fetuses, the estimated variation in peripheral resistance is much higher than the variation in the brain resistance. The estimated amount of blood flow towards the brain and the lower body and placenta for the four fetuses is plotted in Figure 2.7(h) showing that as the severity condition increases, the percentage of blood flow to the brain increases and the flow to the lower body and placenta is reduced.

2.4 Discussion

We developed a realistic computational model of the fetal circulation to study blood redistribution in IUGR enabling both parametric studies to determine individual contributors to remodelling as well as personalization to quantify changes in an individual fetus. Using this approach, we show that AoI flow changes depend both on brain vasodilation and peripheral resistance increase, while MCA flow is mainly affected by changes in cerebral resistance. Furthermore we showed that individual IUGR fetuses show

2.4. Discussion

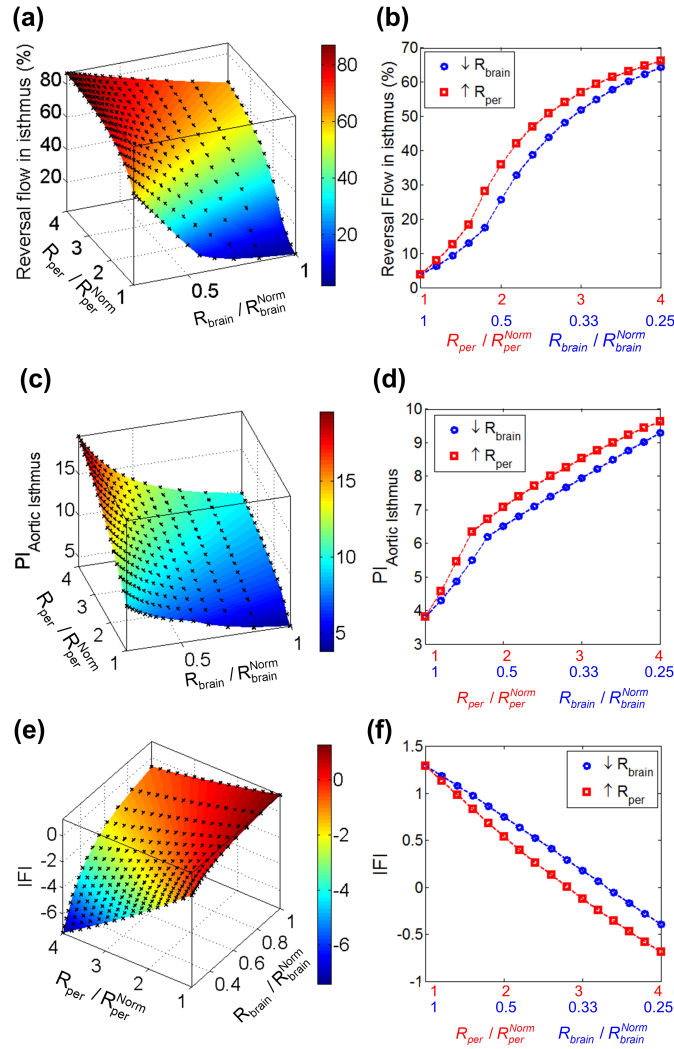


Figure 2.5: Plots illustrating the percentage of reversal flow (a,b), pulsatility index (PI) (c,d) and flow index (IFI) (e,f) in aortic isthmus (AoI) as a function of decrease and increase of brain (R_{brain}) and peripheral (R_{per}) resistances respectively, calculated as the ratio between the current and their corresponding normal values R_{brain}^{Norm} and R_{per}^{Norm} . The plots in the left (a,c,e) show the variation of the three indexes as a function of all the possible combinations of R_{per} increase and R_{brain} decrease. The plots in the right (b,d,f) shows the variation of the three indexes when only one of the resistances was changed and the other was kept unchanged.

marked differences in their vascular components with an exaggerated change in peripheral-placental resistance as major determinant for observed changes in measured Doppler flows.

Table 2.5: Modelling results for the control and the three IUGR fetuses.

	CONTROL	IUGR UA-PEDF	IUGR UA-AEDF	IUGR UA-REDF
Model-based parameters				
Reversal flow in aortic isthmus (%)	3%	7%	33%	91%
Isthmic flow index (IFI)	1.36	1.26	0.52	-12.35
Aortic isthmus PI	3.39	4.22	6.20	28.09
Cerebral Artery (CA) PI	2.82	1.54	1.45	1.18
Descending Aorta PI/CA PI	1.10	1.92	2.72	5.14

IUGR, intrauterine growth restriction; UA, umbilical artery; PEDF, present end-diastolic flow; AEDF, absent end-diastolic flow; REDF, reversed end-diastolic flow; PI, pulsatility index.

For this, we implemented and calibrated a lumped model of the fetal circulation taking into account the main arteries of the fetal circulation, including the ductus arteriosus and the aortic isthmus. Previous approaches to model the fetal circulation focused mainly on the (oxygen) exchange within the placenta [34,37,38] or have only modeled fetal circulation under normal conditions [35,36]. Some previous studies that investigated the influence of an increase in placental resistance on flow related indexes did not include the ductus arteriosus, thus limiting its comparison with in-vivo imaging and the translation to clinical practice [39,40]. Therefore, to our knowledge, ours is the first attempt to evaluate the effect of peripheral and cerebral resistances on AoI flow by using a computational model of the fetal circulation. Another important difference from previously published models is that we use data from individual clinical imaging as boundary conditions for each modeled subject, instead of considering a single flow input with fixed values calculated from the literature. The reliability of our model was ensured by comparing the model-based flow waveforms with Doppler velocity profiles recorded in the control fetus. Moreover, the fraction of cardiac output distributed to the different peripheral regions of the fetus obtained with our model agrees with the cardiac output distribution measured in human fetuses [56,81,82], and also estimated in other models [35,36].

We have comprehensively evaluated how the flow in AoI and CA are affected by changes in the vascular resistances. The increase in placenta vasculature resistance together with the vasoconstriction of the lower body arteries were modeled by increasing the peripheral resistance. The cerebral vasodilation that occurs as a compensatory mechanism to fetal hypoxia and undernutrition was modeled by decreasing brain resistance. We observed that, as increasing the modeled IUGR severity, diastolic flow in AoI decreases and, in very severe cases becomes markedly retrograde. This pattern of changes in AoI flow is consistent with the changes clinically described

2.4. Discussion

in IUGR cases [18, 19, 52, 55, 56]. We also found that the AoI flow changes observed in IUGR are influenced independently by both cerebral vasodilation and peripheral resistance increase. Previous reports suggested that the decrease in cerebral resistance plays a major role in determining the net AoI diastolic flow since MCA vasodilation precedes AoI flow abnormalization [54]. Other studies have described a correlation between the IFI and postnatal neurodevelopmental outcome [52, 53], supporting the impact of cerebral vasodilation in AoI flow changes. However, other studies [52] [55] indicated that since the AoI is connecting the two fetal circulations in parallel, AoI flow pattern reflects the existence of differences in vascular resistances, suggesting that both the increase in peripheral resistance and the cerebral vasodilation are responsible for AoI flow changes. Our results support this last hypothesis since we showed that not only cerebral vasodilation but also the increase in peripheral resistance altered the AoI flow pattern. These results are consistent with the consideration of AoI as a good predictor of not only the poor neurodevelopmental outcome [51, 52] but also of the high risk of adverse perinatal outcome and mortality [49, 53, 85].

Regarding the CA, we showed that the decrease in PI_{CA} is mostly related to cerebral vasodilation and much less influenced by changes in the periphery/placenta. This is also reflected in the amount of blood flow that is distributed towards the brain and towards lower body and placenta. For example, when brain resistance was decreased by 75%, the flow that went to the lower body and placenta was decreased by 57% but cerebral flow increased 150%, showing how cerebral vasodilation is the most responsible for the blood flow increase in CA. These results are in line with those previously reported by van den Wijngaard et al. [40] and consistent with MCA being a risk stratifying factor for suboptimal neurodevelopment in IUGR rather than perinatal complications [50] [85]. Finally, PI_{dAo}/PI_{CA} showed a linear increase with the severity of IUGR, starting from a value about 1.0 for the control fetus. This result was consistent with the data published by Makikallio et al. [55] that showed also a value of 1.0 in control fetuses and an increase in the IUGR group.

Next we constructed patient-specific models of three IUGR fetuses. We were able to reproduce the AoI and CA flow waveforms and also the model-based values for AoI PI, CA PI and IFI parameters were consistent with the measured ones, demonstrating that the developed lumped model of the fetal circulation not only is able to reproduce the hemodynamic changes that occur in fetuses under normal conditions, but also with increased peripheral-placental resistance and vasodilation. This is helpful to estimate parameters that cannot be measured clinically such as the relative variation of the upper and lower body resistances who might be more directly related to the staging of the disease than only the measurements of PI, currently used in clinical

practice.

However, the presented lumped model has some limitations. Firstly, 0D lumped models only consider the temporal variation of pressure, flow and volume variables, assuming no variation of these parameters in the spatial dimension. However, since the aim of the study was to evaluate the hemodynamic interactions among the different cardiovascular parts, without considering flow phenomena or wave reflections, we think that 0D lumped models were accurate enough for our purpose. Also, the model is a simplified version of the fetal arterial tree because it only considers one artery and one peripheral bed for the lower body. However since the goal was to study the flow changes in the AoI and brain we considered that including or not all the lower arteries and organs would have the same effect on the AoI and cerebral flows. Secondly, the increase in right ventricular predominance observed in IUGR fetuses [56, 86, 87] was not taken into account for the parametric study as we decided to focus on the resistance variation and used the measurement of a normal fetus as input rather than changing the input for each combination of resistances. Thirdly, the fetal heart was not modeled. Nevertheless, since we used patient-specific Doppler waveforms at the ventricular outputs as the input of the model, we were indirectly considering the cardiac changes that may affect the cardiac output when studying the individual cases. Fourthly, our model does not take into account the major biochemical disorders created by placental circulatory insufficiency, such as low pH, hypoxia and respiratory acidosis, that can interfere with the normal cardio circulatory function and play a significant role in the hemodynamic changes during IUGR [88]. Fifthly, considering a venous pressure of 0 mmHg could have an effect, but mainly on the pressure values. However, we were interested only in flow waveforms and we were able to reproduce the measured Doppler traces in all cases. Finally, although we are not estimating all the parameters that may change between subjects and/or under pathological conditions, we still can consider our approach as a patient-specific modelling. We are using patient-specific data to build the model and its boundary conditions (gestational age, fetal weight, heart rate, Doppler velocities and valve radius) to finally estimate the specific resistances variation for each individual.

2.5 Conclusions

In conclusion, the proposed equivalent lumped model seems to be a good approximation to assess hemodynamic changes in the fetal circulation under abnormal growth conditions. Further developments of the model can be useful for assessing further vessels and their interactions under various clinical conditions, and the impact of interventions. Our results suggested that AoI

2.5. Conclusions

flow is affected by peripheral-placental as well as cerebral resistances while CA flow mainly depends on cerebral resistance. Furthermore, when personalizing the model to IUGR fetuses we were able to estimate the specific vascular resistances variation, suggesting that the peripheral-placental resistance is the major determinant for observed changes in measured Doppler flows. This study supports the potential role of AoI as marker of adverse perinatal and neurological outcome since it is a central vessel connecting the two ventricular outputs and therefore its flow reflects the balance between ventricular output and upper/lower body vascular resistances. Personalizing the model shows promise to directly assess properties of the vascular bed rather than using indirect Doppler measurements.

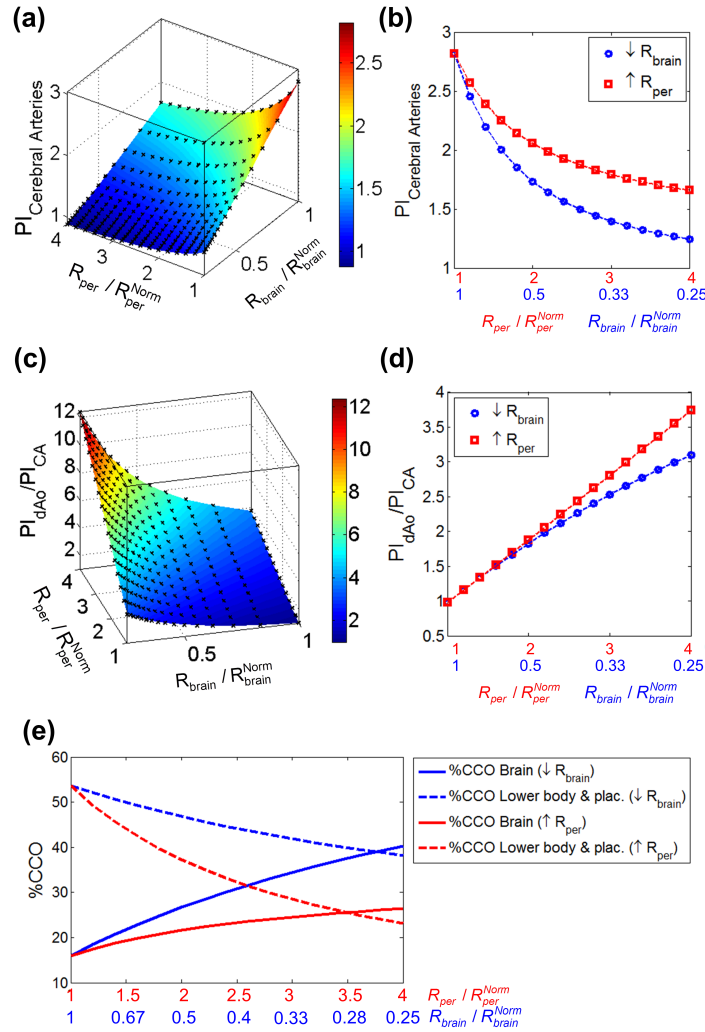


Figure 2.6: Plots illustrating the pulsatility index (PI) in cerebral arteries (a,b) and the ratio of PI in descending aorta (PI_{dAo}) and PI in cerebral arteries (PI_{CA}) (c,d) as a function of decrease and increase of brain (R_{brain}) and peripheral (R_{per}) resistances respectively, calculated as the ratio between the current and their corresponding normal values R_{brain}^{Norm} and R_{per}^{Norm} . The plots in the left (a,c) show the variation of the two indexes as a function of all the possible combinations of R_{per} increase and R_{brain} decrease. The plots in the right (b,d) shows the variation of the two indexes when only one of the resistances was changed and the other was kept unchanged. (e) Percentage of combined cardiac output (CCO) going towards the brain (solid line) and towards the lower body & placenta (dashed line) plotted as a function of decrease and increase of brain (R_{brain}) and peripheral (R_{per}) resistances respectively.

2.5. Conclusions

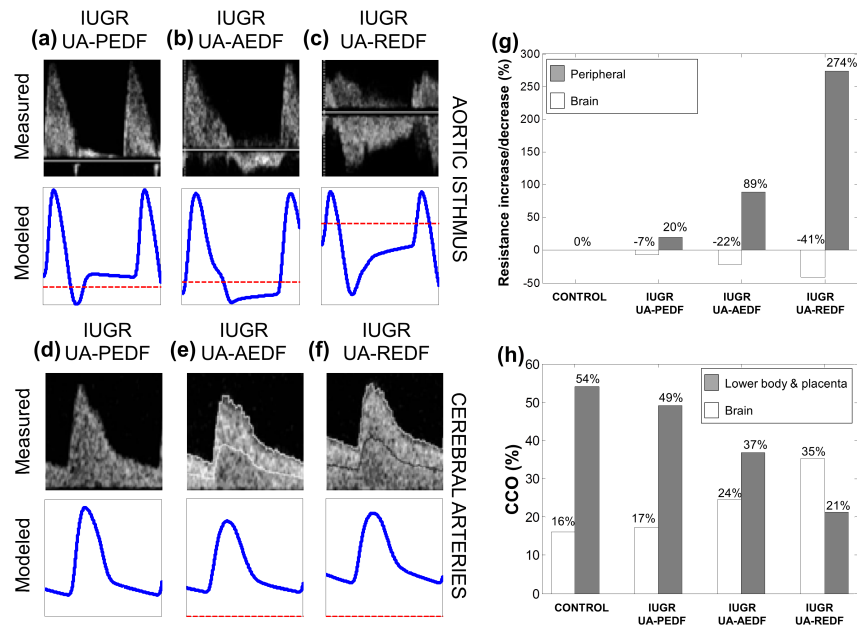


Figure 2.7: Comparison between measured (top) and model-based (bottom) blood flow waveforms in the aortic isthmus (a-c) and cerebral arteries (d-f) for the intrauterine growth restricted (IUGR) fetuses with umbilical artery (UA) present (PEDF), absent (AEDF) or reversed (REDF) end-diastolic flow. Dashed line indicates a blood flow of $0 \text{ ml} \cdot \text{s}^{-1}$. (g) Percentage of estimated increase in peripheral-placental resistance (grey bars) and decrease in brain resistance (white bars) calculated for each individual. (h) Estimated percentage of combined cardiac output (CCO) towards the brain and towards the lower body and placenta for each individual.



CHAPTER **3**

Understanding the aortic isthmus
Doppler profile, and its changes with
gestational age, using a lumped model
of the fetal circulation

Abstract — The aortic isthmus (AoI) plays an important role during prenatal life in the assessment of fetal hemodynamics since it connects both upstream and downstream circulations. The AoI (Doppler) blood flow has a characteristic shape with a small notch at the end of systole observed during the third trimester of pregnancy. However, what causes the appearance of this notch is not fully understood. We used a lumped model of the fetal circulation to study the individual contributions of possible factors causing the end-systolic notch/peak of reversal flow and the changes of AoI flow through the gestation. Firstly, a validation of the model was performed by fitting patient-specific data from two normal fetuses. Then, single and multi parametric analyses were performed to evaluate the major determinants of the appearance of the end-systolic notch in the AoI flow. Finally, the changes in the AoI flow profile through gestation were assessed. Our lumped model of the fetal circulation allows to adequately simulate the AoI waveform. The delay in the onset of ejection together with the longer ejection duration of the right ventricle are the most relevant factors in the origin of the end-systolic notch in the AoI flow. It appears around 25 week of gestation and becomes more pronounced with advancing gestation. We demonstrated that the characteristic notch on the AoI flow at the end of systole occurs mainly as a result of a delayed and longer ejection of the right ventricle. Our findings improve the understanding of hemodynamic changes in the fetal circulation and the interpretation of clinical (Doppler) imaging.

Adapted from: Garcia-Canadilla P, Crispi, F, Cruz-Lemini M, Valenzuela-Alcaraz B, Rudenick PA, Gratacos E, Bijmens BH. *Understanding the aortic isthmus Doppler profile, and its changes with gestational age, using a lumped model of the fetal circulation*. Submitted, 2015.

3.1 Introduction

The aortic isthmus (AoI) is the segment of the aorta located between the origin of the left subclavian artery and the junction of the ductus arteriosus to the descending aorta. During prenatal life, this aortic segment plays an important role since it connects both upstream (including brain) and downstream (including placenta) circulations. The AoI is also the only arterial segment that connects both ventricular outputs ejecting blood in parallel to the upper and the lower body of the fetus. Its unique disposition makes the AoI a good candidate for the assessment of the fetal hemodynamic condition. Under normal physiological conditions the AoI has a forward (cranio-caudal) direction of blood flow, both in systole and diastole. The AoI (Doppler) blood flow profile has a characteristic shape with a rapid systolic rise of the velocity, followed by a more gradual deceleration with a small notch (in some cases) at the end of systole, with forward flow during diastole. Some studies [17, 18] have reported that this small notch starts to appear at 25-30 weeks of gestation approximately with a progressive increase with the advance of gestation, resulting in a brief peak of reversal flow at the end of systole/beginning of diastole. However, the origin of this reversed peak is unclear. On the one hand, Acharya et al. [19] hypothesized that this brief peak of reversal flow at the end of systole occur as a result of delayed onset and longer acceleration time of the flow coming from the ductus arteriosus [89]. The same authors also stated that this late systolic brief peak of reversal flow could be explained by the longer pre-ejection period of the right ventricle, as observed in fetal lambs, resulting in an ejection delay that may affect the last milliseconds of systolic flow in the isthmus [90]. A recent study [91] has evaluated the appearance of the end-systolic notch in fetuses along the gestation by Doppler echocardiography. The authors found an inverse correlation between the amplitude of the end-systolic notch and the right ventricular output, explained by the major proportion of the right ventricular output that goes through the ductus arteriosus, which has a retrograde influence in the isthmus flow at late systole. However, the authors did not investigate the origin of this late and higher amount of flow from the right ventricle. They suggested three different mechanisms that could explain the appearance of the notch: (1) greater stroke volume with longer ejection time of the right ventricle, (2) a longer pre-ejection period of the right ventricle, and, in their opinion the most likely, (3) the variation in the compliance of the fetal pulmonary arterial network throughout gestation. However, on the other hand, Del Rio and colleagues considered this brief reversal of flow artifactual [20], since it is difficult to explain the detection of both forward and reversal flow at the same time and in the same arterial segment. Also this brief reversal flow is less recorded in the three-

vessel-trachea view even when it was observed in the longitudinal aortic arch plane [20]. Therefore, the origin of this end-systolic notch of the AoI is still not fully understood.

It has been described that the volume and direction of AoI is determined by the systolic performance of the left and right ventricles together with the peripheral vascular resistances. During systole, blood coming from the left ventricle causes forward flow through the AoI, whereas that from the right ventricle has the opposite effect. This suggests that the late-systolic flow in the AoI is influenced by the difference in the ejection onset and duration between ventricles, and also in the flow volume as well as the balance between upper and lower body resistances. Therefore, differences in timing and amount of flow between pulmonary artery and aortic flows could play a role in the origin of the AoI end-systolic notch. Acharya et al. reported that the pre-ejection period of the right ventricle is longer than the left [19,92]. The duration of the ejection of the right ventricle seems to be slightly longer than that of the left ventricle, as reported by Fouron et al [16]. Some authors have reported that the time-to-peak velocity or acceleration time in the aorta is longer compared to that in the pulmonary artery [93,94]. In the human fetus, the right ventricle ejects more blood than the left ventricle, and this dominance of the right ventricle increases with advancing gestation [56,95], reaching a maximum difference (60% versus 40%) at term [96]. The blood velocity profile of the right cardiac outflow clearly shows two periods of velocity decrease: the first slow and the second fast. In contrast, the blood velocity profile of the left outflow shows a homogeneous velocity decrease. Finally, as suggested recently [91], changes in the elastic properties of the pulmonary vasculature could also have an effect in the appearance of the notch. As far as we know, since it is very challenging in-vivo, there are no studies measuring the differential effect of each of these factors on the AoI flow profile and specifically in the appearance of the end-systolic notch. In the present study, we propose to use a computational model of the fetal circulation to evaluate the individual, as well as combined, influence of all these parameters on the AoI flow profile and their role in the appearance of the end-systolic notch.

Computational models are a useful tool for studying the fetal cardiovascular system and recreating hemodynamics changes in the fetal circulation [35,36,40,97–99]. In lumped models, the different parts of the fetal circulatory system are modeled by a set of equivalent electrical components such as resistors, capacitors and inductors. We have developed and validated a lumped model of the fetal circulation including the main arteries and vascular beds, which helped in better understanding the hemodynamics changes induced by intrauterine growth restriction [97]. In the present study, we aimed to use our lumped model to better understand the appear-

3.2. Methods

ance of the end-systolic notch in the AoI flow profile. For this, we first validated the model for its ability to reproduce the AoI end-systolic peak of reversal flow by personalizing it to 2 normal control fetuses with different gestational ages (one showing an end-systolic peak of reversal flow in the AoI blood Doppler waveform, and the other not) to demonstrate that our model is able to reproduce the appearance of the end-systolic notch in the AoI blood flow waveform, as measured by Doppler echocardiography. Next, different parametric studies were performed to evaluate what influenced the appearance of the notch. To do this, we constructed different aortic and pulmonary blood inflow functions mimicking different timing and amount of blood flow differences between both ventricular outflows that are believed to be relevant for the end-systolic notch appearance. Then, these blood flows were used as input of our lumped model to obtain the model-based AoI flows. The variation in the compliance of the pulmonary circulation and in the lung resistance was evaluated also. Different single and multi parametric studies were performed to quantify the influence of each variable in the AoI flow direction at the end of systole.

3.2 Methods

3.2.1 Lumped model of the fetal circulation

In this study, we used a previously published lumped model of the fetal circulation [97]. Briefly, the model consisted of 14 arterial segments, including the AoI and the ductus arteriosus, 8 vascular beds and 2 blood flow inputs: the aortic and pulmonary artery blood flow profiles, as shown in Figure 3.1. Arterial segments were modeled with a resistor to represent the local resistance of blood due to blood viscosity, a capacitor to represent the arterial compliance and an inductor to represent the blood inertia (Figure 3.1). Vascular beds consisted of a three-element Windkessel model, which included a resistor and a capacitor representing the peripheral resistance and compliance respectively. The values of all the electrical components were calculated according to the gestational age and the estimated fetal weight of the fetus, under normal physiological conditions. The variation of the arterial Young's modulus and the vascular bed compliances with the gestational age was included. Specifically, the arterial Young's moduli were scaled following the expression of van den Wijngaard et al. (Eq. 5 in [100]). Vascular bed compliances were scaled to their values at each corresponding gestational age, using the expression reported by van Gemert et al (Eq. 4k-4l in [101]).

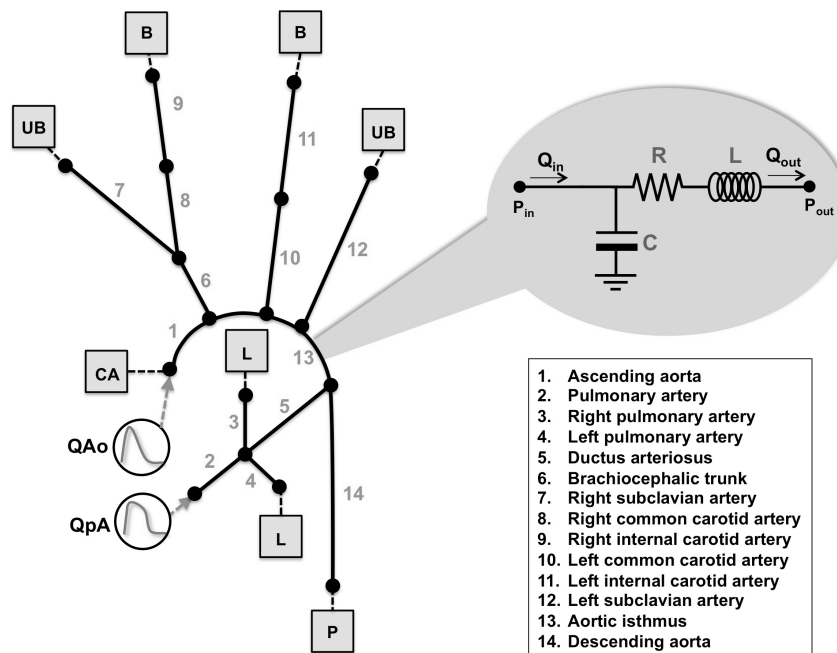


Figure 3.1: Anatomical configuration used to model the fetal circulation, composed of 14 arterial segments, 8 vascular beds (CA = coronary arteries, B = brain, UB = upper body, L = lung and P = peripheral) and 2 blood flow inputs. An example of the equivalent electrical lumped model of one of the arterial segments is also displayed.

3.2.2 Validation of the lumped model for assessing the AoI flow profile

In order to validate the lumped model of the fetal circulation for its ability to reproduce the AoI end-systolic peak of reversal flow, we used real Doppler data from 2 normal fetuses with different gestational ages (one > 30 weeks of gestation showing an end-systolic peak of reversal flow in the AoI blood waveform, and the other < 30 weeks of gestation not showing the peak). The detailed methodology of the validation procedure is described in Appendix (section: 3.A).

3.2.3 Single and multi parametric analysis to study what influences the AoI flow

Five variables determining aortic and pulmonary flows that could potentially affect the AoI waveform were chosen for the single and multi parametric analysis including: (1) difference in the duration of the slow deceleration of ejection (T_{sd}) between aortic and pulmonary artery flows, (2) difference

3.3. Results

between LV and RV ejection times (*ET*), (3) delay in the onset of RV and LV ejection or difference between pre-ejection periods (*PEP*), (4) difference between aortic and pulmonary artery time-to-peak velocities (*TPV*) and (5) relative cardiac output (*CO*). In each single parametric analysis, the aortic and pulmonary flows waveforms were changed in only one of the variables while keeping the rest of them equal between both blood flow profiles. Then, these blood flows (Figure 3.2) were set as input of the computational model. After each simulation, the model-based AoI flows were obtained in order to study the influence of each variable on the AoI flow separately. Additionally, two other variables of the pulmonary arterial network were chosen for single parametric analysis: (6) pulmonary vasculature compliance and (7) lung resistance. Details on the single parametric analysis can be found in section 3.B.4 of the supplementary methods. The next step was to perform a multi parametric study, including all the possible combinations between the different variables. Details on the multi parametric analysis can be found in section 3.B.5 of the supplementary methods. These different parametric studies were performed for a specific gestational age. However, some several variables change during gestation, such as the amount of blood ejected by both ventricles, the heart rate, the *TPV*, etc... as well as other hemodynamic variables such as vascular resistances and compliances. For this reason, the change of the AoI flow pattern with advancing gestation was also studied. Details on simulating the advance of gestation can be found in section 3.B.6 of the supplementary methods.

3.3 Results

3.3.1 Validation

Ultrasound and perinatal data of the both fetuses is shown in Table 3.1. The measured and model-based velocity waveforms in the AoI and middle cerebral artery (MCA) are displayed in Figure 3.3. The estimated patient-specific parameters after the optimization procedure are shown in Table 3.2, validating the good performance of the model in retrieving patient-specific data.

3.3.2 Single parametric studies

The aortic and pulmonary artery flows, as well as their difference, constructed for the 5 single parametric studies, together with the resulting model-based blood flows in the AoI, are plotted in Figure 3.4. The model-based AoI waveforms resulting from the single parametric analysis on the variation of pulmonary vasculature compliances and on the variation of lung re-

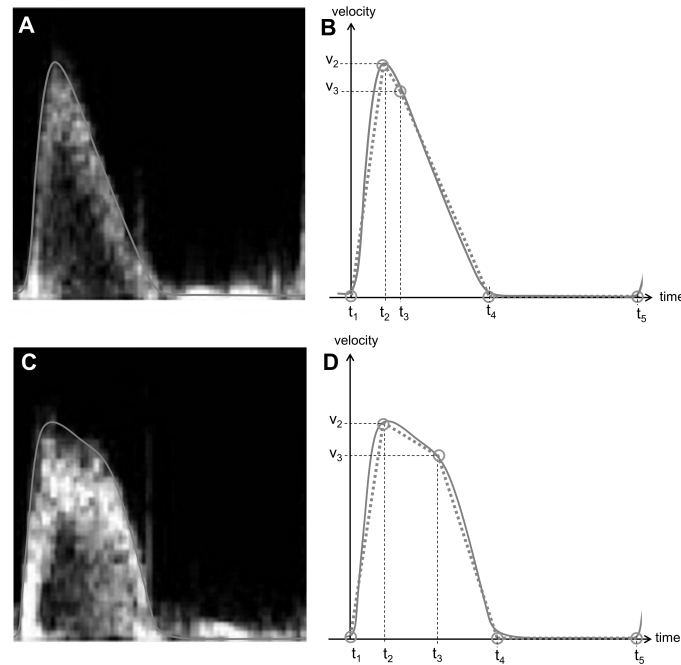


Figure 3.2: Doppler velocity waveforms from the (a) aortic and (c) pulmonary artery blood flows from a healthy fetus of 33.4 weeks of gestation. (b) And (d) characterization of the velocity profiles with 5 points (t_i, v_i) and 4 straight lines used to construct the custom velocity profiles from the aortic and pulmonary artery flows. t_i denotes the temporal points and v_i the velocity at each temporal point t_i .

sistance are shown in Figure 3.5. The graphs suggest that the delay in the onset of ejection (Figure 3.4(i)-(l)) and the longer ejection of the right ventricle (Figure 3.4(e)-(h)) are the factors that seem to have the major influence on the appearance of the end-systolic notch in the AoI blood flow (Figure 3.4(d, h, l, p, t)). Furthermore, looking at the graphs corresponding to the difference between aorta and pulmonary artery blood flows (Figure 3.4(c, g, k, o, s)), it seems that the appearance and amplitude of the end-systolic notch is explained by the difference between pulmonary artery and aortic flows in the last milliseconds of the ejection, so that as the flow difference increased the notch would be more pronounced.

3.3.3 Multi parametric study

The results of the linear multivariate regression analysis are shown in Table 3.3. The difference in the onset of ejection and the longer ejection of the right ventricle are the strongest factors to contribute to the appearance of the end-systolic notch in the AoI. The amount of flow of the difference between

3.3. Results

Table 3.1: Prenatal ultrasound and perinatal characteristics of the study individuals

	FETUS 29 weeks	FETUS 35 weeks
<i>Ultrasound data</i>		
Gestational age at scan (weeks.days)	29.2	35.6
Estimated fetal weight (g)	1481	2400
Estimated fetal weight centile	81	16
Aortic peak velocity (cm/s)	75	91
Pulmonary artery peak velocity (cm/s)	65	97
Aortic valve diameter (mm)	5.7	7.5
Pulmonary valve diameter (mm)	6.5	8.4
Left ejection time (ms)	171	172
Right ejection time (ms)	171	172
Aortic time to peak velocity (ms)	41	40
Pulmonary time to peak velocity (ms)	36	37
Relative cardiac output	1.20	1.60
Heart rate (bpm)	137	143
Umbilical artery PI	1.31	0.93
Umbilical artery end-diastolic flow	Present	Present
Middle cerebral artery PI	2.09	1.88
Cerebroplacental ratio	1.59	2.02
Aortic Isthmus PI	2.82	2.53
Isthmus flow index	1.25	1.52
<i>Perinatal outcome</i>		
Gestational age at delivery (weeks.days)	40.0	40.0
Birth weight (grams)	3350	2990
Birth weight centile	52	15
Gender	Male	Male
Cesarean section	No	No
5-minute Apgar score	10	10
Umbilical artery pH	7.27	7.12
Preeclampsia	No	No
Days in neonatal intensive care unit	0	0

IUGR, intrauterine growth restriction; UA, umbilical artery; PEDF, present end-diastolic flow; AEDF, absent end-diastolic flow; REDF, reversed end-diastolic flow; PI, pulsatility index.

pulmonary artery and aortic flows during the deceleration of ejection was highly correlated with the amplitude of the end-systolic notch of the AoI flow ($R = -0.7268$ with $p < 0.001$) showing that the higher the flow of the pulmonary artery at the last part of systole compared to the aortic flow, the more pronounced the notch would be.

3.3.4 Simulating the advance of gestation

Figure 3.6 shows the different aortic (Figure 3.6(a)) and pulmonary artery (Figure 3.6(b)) blood flows constructed for each gestational age, without

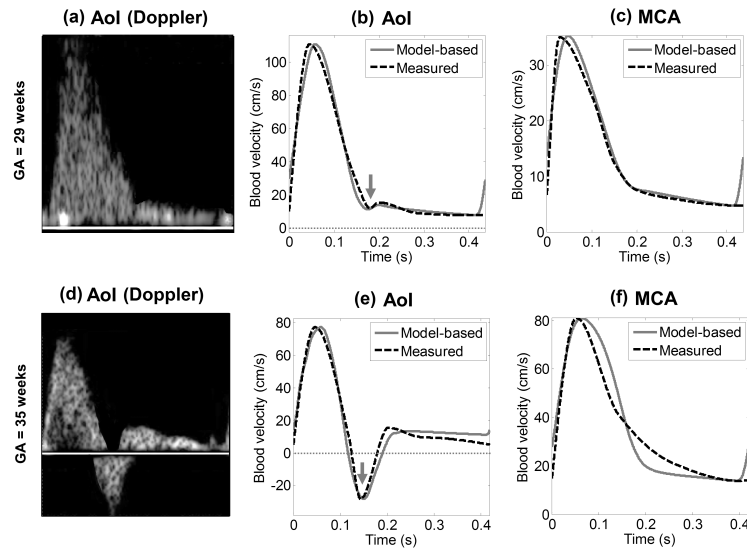


Figure 3.3: (a) Aortic isthmus (AoI) Doppler velocity waveform, (b) AoI and (c) middle cerebral artery (MCA) blood velocity model-based (in solid line) and measured (in dash line) waveforms for the fetus with 29 weeks of gestation. (d) AoI Doppler velocity waveform, (e) AoI and (f) MCA blood velocity model-based (in solid line) and measured (in dash line) waveforms for the fetus with 35 weeks of gestation. The red dashed line indicates a flow of 0ml/s . Red arrows point to the notch in the fetus of 29 weeks of gestation and to the peak of reversal flow in the fetus of 35 weeks of gestation, at the end of systole.

considering any difference in timing and with the same amount of blood ejected by both ventricles, together with the corresponding model-based AoI flow waveforms (Figure 3.6(c)). Figure 3.7 shows the different aortic (Figure 3.7(a)) and pulmonary artery (Figure 3.7(b)) blood flows constructed for each gestational age taking into account the timing and blood volume differences between both blood flows across gestation. This illustrates how, with advancing gestation, the dominance of the right ventricle becomes higher and therefore the relative CO increases. Also, the model-based AoI flow waveforms obtained for each gestational age were plotted together in Figure 3.7(c).

When both aortic and pulmonary artery blood flows were unchanged during the simulations, the AoI flow waveform did not show any notch or peak of reversal flow at the end of systole (Figure 3.6(c)-3.6(e)). Similarly, neither an increased (Figure 3.6(d)) or decreased (Figure 3.6(e)) variation in lung compliance throughout the gestation had an influence on the peak (Figure 3.6(d)). Only when both blood flows were constructed taking into account the differences in timing and blood volume, as was described for

3.4. Discussion

Table 3.2: Values of the estimated parameters after nonlinear optimization

	FETUS 29 weeks	FETUS 35 weeks
Peripheral Resistances ($mmHg \cdot s \cdot ml^{-1}$)		
Brain	57.93	56.09
Upper body	30.12	49.06
Lungs	29.08	29.54
Peripheral	3.13	7.89
Peripheral Compliances ($ml \cdot mmHg^{-1}$)		
Brain	0.0029	0.0095
Upper body	0.0135	0.0180
Lungs	0.0080	0.0145
Peripheral	0.0681	0.0741
E ($dyn \cdot cm^{-2}$)		
aAo, AoI and pA	$5.99 \cdot 10^5$	$6.16 \cdot 10^5$
Ductus Arteriosus	$10.79 \cdot 10^5$	$11.09 \cdot 10^5$
Descending Aorta	$7.26 \cdot 10^5$	$9.46 \cdot 10^5$
BCT, SCA and CCA	$5.47 \cdot 10^5$	$6.65 \cdot 10^5$
ICA	$9.84 \cdot 10^5$	$11.98 \cdot 10^5$
Delay of onset of ejection (ms)	0.086	3.84

E = Young's Modulus, aAo = ascending aorta, AoI = aortic isthmus, pA = pulmonary arteries, BCT = brachiocephalic trunk, SCA = subclavian arteries, CCA = common carotid arteries, ICA = internal carotid arteries.

Table 3.3: Results of the multivariate regression analysis

	Coefficient	SE	p
$Tds_{pA} - Tds_{Ao}$	-16.8	0.18	< 0.001
$ET_{pA} - ET_{Ao}$	-41.8	0.38	< 0.001
$PEP_{pA} - PEP_{Ao}$	-80.1	1.14	< 0.001
$TPV_{pA} - TPV_{Ao}$	-29.5	0.93	< 0.001
RCO/LCO	-1.6	0.02	< 0.001

Root Mean Squared Error: 0.215, R-squared: 0.908, p-value = 0.0

SE, standard error; Tds , Time of the slow deceleration of the ejection; ET , ejection time; PEP , pre-ejection period; TPV , time-to-peak velocity; RCO , right cardiac output; LCO , left cardiac output; pA , pulmonary artery; Ao , aorta.

each gestational age, the end-systolic notch started to appear around 31-32 weeks of gestation and became more pronounced with advancing gestation (Figure 3.7(c)).

3.4 Discussion

We have successfully used a lumped model of the fetal circulation to investigate the origin of the end-systolic notch observed in the AoI (Doppler)

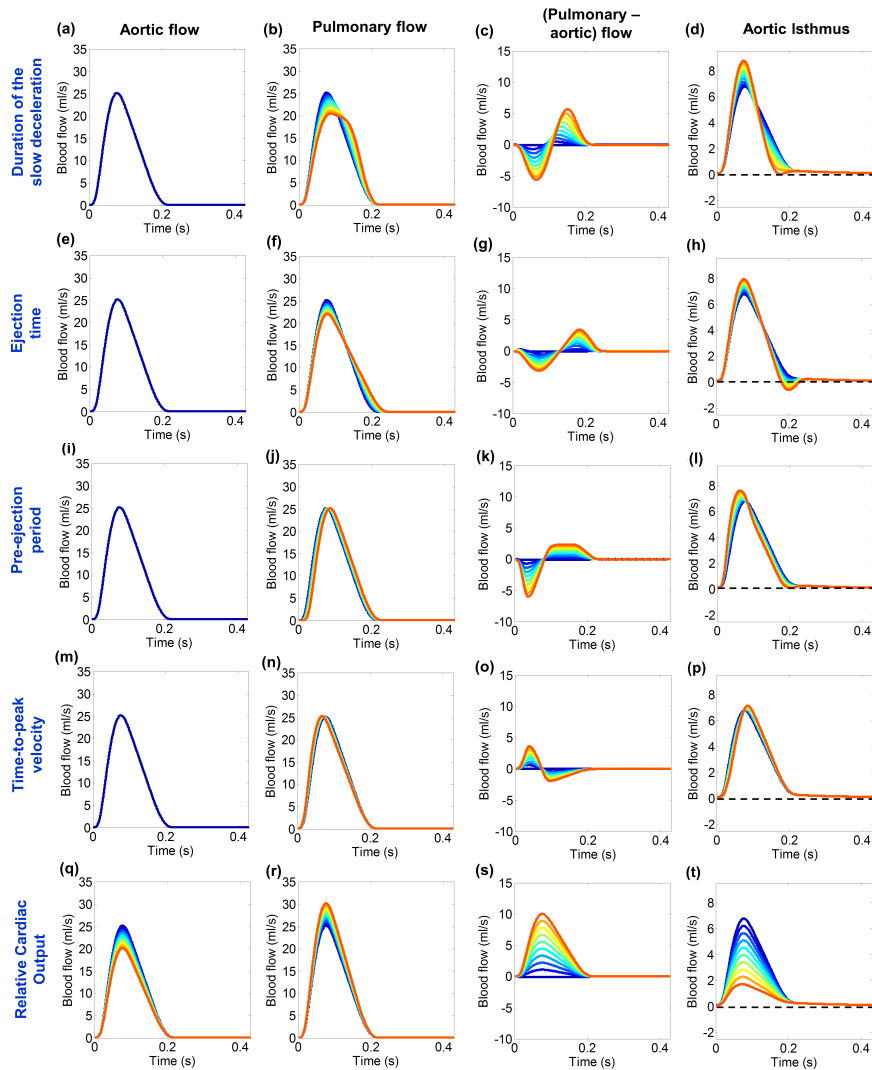


Figure 3.4: **From left to right:** Aortic flow, pulmonary artery flow, difference between pulmonary artery and aortic flows and aortic isthmus model-based flow waveforms. **From top to bottom:** resulting plots from the 5 single parametric studies (a)-(d) Duration of the slow deceleration of ejection phase, (e)-(h) Ejection time, (i)-(l) Pre-ejection period, (m)-(p) Time to peak velocity and (q)-(t) relative right and left cardiac outputs (RCO/LCO). The dashed line indicates a flow of 0ml/s .

blood flow waveforms in healthy fetuses at the end of gestation. With our approach we could demonstrate that the brief reversal of flow in the AoI at the end of systole occurs mainly as a consequence of the timing differences between pulmonary and aortic blood flows that cause a delay in the

3.4. Discussion

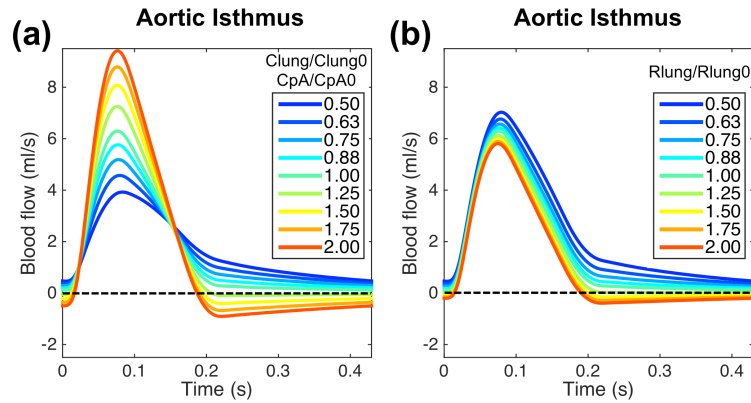


Figure 3.5: Model-based flow waveforms in the aortic isthmus resulting from the single parametric analysis on (a) the variation of pulmonary vasculature compliance and (b) the variation of lungs resistance. Both aortic and pulmonary artery blood flows were kept exactly equal. The dashed line indicates a flow of 0ml/s . Clung: lungs compliance, CpA: pulmonary arteries compliance and Rlung: lungs resistance.

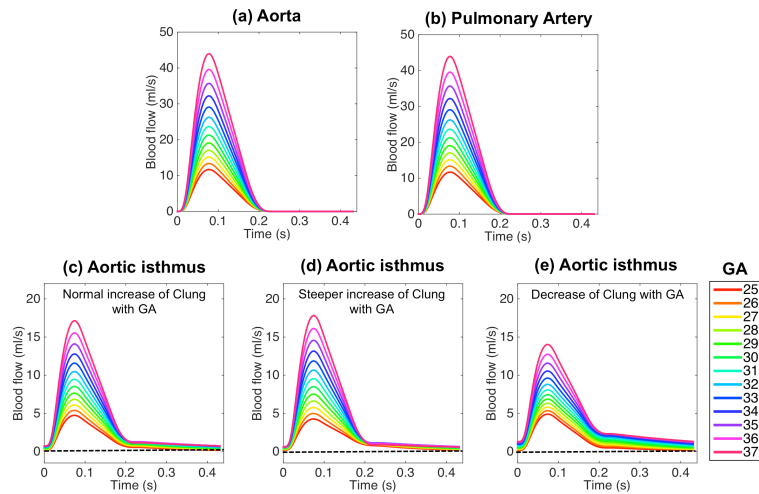


Figure 3.6: (a) Aortic and (b) pulmonary artery blood flows constructed for each gestational age with fixed timing parameters (not considering the changes throughout gestation of the timing variables of both pulmonary and aortic flows) and relative amount of flow of 1.0 (c)-(e) Model-based flow waveforms in the aortic isthmus obtained for each simulated gestational age using (c) normal (d) steeper and (e) decreasing scaling function for the lungs compliance. The dashed line indicates a flow of 0ml/s . GA denotes gestational age.

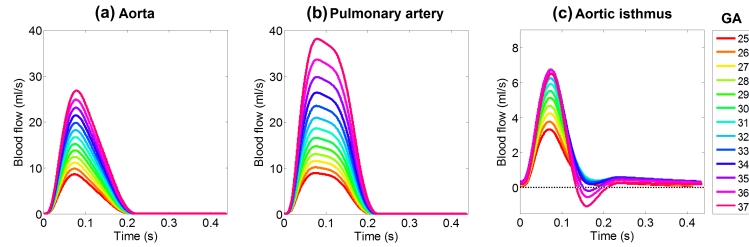


Figure 3.7: (a) Aortic and (b) pulmonary artery blood flows constructed for each gestational age with different timing variables (considering the changes throughout gestation of the timing variables of both pulmonary and aortic flows) and relative amount of flow between both flow functions. (c) Model-based flow waveforms in the aortic isthmus obtained for each simulated gestational age. The dashed line indicates a flow of 0ml/s . GA denotes gestational age.

flow going through the ductus arteriosus. Thus, the ejection delay between both ventricles may allow the right ventricle to affect the last milliseconds of systolic flow in the AoI, leading to a brief reversal of flow in late systole.

We first demonstrated that our lumped model was able to reproduce the real blood flow patterns in the AoI and MCA by performing a patient-specific fitting using the echocardiographic data of two normal fetuses, one of them showing an end-systolic peak of reversal flow in the AoI velocity waveform. The results demonstrated that our lumped model was able to reproduce the measured waveforms in both AoI (including end-systolic reversal peak when present) and MCA. Moreover, the delay in the onset of ejection between the aorta and pulmonary artery flows could be estimated. The estimated delay for the fetus showing reversal of flow in the AoI velocity trace was much bigger than for the fetus with forward flow in the AoI during the whole cardiac cycle. This result fits well with the experimental results of De Muylder et al. [90] showing that the pre-ejection period of the right ventricle was longer than that of the left, and suggested that this delay in the onset of right ventricular ejection could explain the reversal of AoI flow at late systole [19, 92].

This is the first study that has demonstrated *in silico* that the timing differences between pulmonary and aortic blood flows are the main determinants for the appearance of the end-systolic reversal flow in the AoI. Both single and multi parametric analyses showed that the delay in the onset of ejections and also the longer ejection duration of the right ventricle are the main factors determining the reversal of flow in the AoI at the end of systole. These findings are in agreement with previous studies, describing a longer ejection [16] and pre-ejection period [90] of the right ventricle in normal fetuses. In addition, the flow difference between pulmonary artery

3.4. Discussion

and the aorta during the deceleration of ejection was highly correlated with the amplitude of the end-systolic notch of the AoI flow. Thus, any change in timing or amount of flow which results in more flow coming from the right ventricle than from the left at the end of systole can lead to the reversal of flow in the AoI. These results agree with the previously formulated hypothesis by Acharya et al. [19, 92] that AoI flow reflects the balance between both ventricular outputs, meaning that any difference in ejection force duration or volume between both affects the shape of the AoI velocity waveform during systole. Chabaneix et al. have reported recently similar results [91]. The authors quantitatively evaluated the appearance and magnitude of the end-systolic notch in the AoI waveform through gestation, in normal pregnancies, by Doppler echocardiography and they found an inverse correlation between the right ventricular output and the amplitude of the notch. They stated that the major proportion of the elevated right ventricular output that goes through the ductus has a systolic retrograde influence in the AoI flow. They hypothesized that this can be explained by three different mechanisms: a longer ejection time of the right ventricle, a difference in the opening time of the semilunar valves and, a suggested by the authors as the most likely, the variation in the compliance of the fetal pulmonary arterial network. However they have not quantified the different possible causes. In this paper we demonstrated that the longer pre-ejection period of the right ventricle has the major influence on the end-systolic notch amplitude, and not the variation of the fetal pulmonary compliance as suggested by Chabaneix et al.

This study also provides insights in the AoI flow changes throughout gestation. In order to better understand these changes, we performed a parametric study in which, for each gestational age, the specific blood outflows were constructed taking into account the relationships reported in the literature between some of the variables, such as heart rate, acceleration time or the amount of flow, and the gestational age. Since our model was age-dependent, all the components were set with their values calculated for each gestational age. A small notch could be seen at the end of systole in the flow pattern of AoI corresponding to week 25 that progressively became more pronounced as gestation progressed into a short peak of reversal flow from week 34-35 onwards. These results are consistent with human data as Acharya et al. [19, 92] described that forward flow in the AoI is present during the first two trimesters of pregnancy, and around week 25 a small notch at the end of systole can be seen that becomes more pronounced as gestation advances, and also with the results from Chabaneix et al. [91]. Around 31 weeks of gestation, a brief reversal of AoI flow is seen at the end of systole in almost all fetuses [19, 92]. When the same procedure was performed considering the same flow profile for both ventricles (same timing

and amount of flow) these changes in the AoI flow throughout the gestation could not be reproduced, suggesting that the end-systolic notch occurs as a result of the differences in time and flow between the left and right ventricular outflows, rather than increased CO or changes in size and properties of the vasculature. The differences in right/left timing and amount of flow result in a higher amount of flow coming through the ductus arteriosus at the end of systole than through the ascending aorta. Since the blood coming from the ascending aorta causes forward flow through the AoI and that from the ductus arteriosus causes reduction in the forward flow, a brief peak of reversal flow can be seen under these circumstances. Reversal flow in the AoI waveform during late systole can be seen also under pathological conditions such as intrauterine growth restriction. However, this reversal flow is predominantly caused by the increase in placental resistance and the decrease of the cerebral resistance, as we demonstrated previously [97]. The aim of this study was to evaluate the end-systolic reversal flow in the AoI in normal pregnancies throughout the gestation. Therefore the values of the peripheral resistances were always kept within their normal range of values.

3.5 Conclusions

In conclusion, we demonstrated that the characteristic notch in the AoI at the end of systole, and at late gestation, occurs mainly as a result of a delayed and longer ejection of the right ventricle as compared to the left, and therefore is not artifactual as suggested by Del Rio et al. [20]. Additionally, we demonstrated that our lumped model is an useful tool that allows the estimation of patient-specific parameters that cannot be assessed clinically, helping to improve the understanding of the hemodynamic changes in the fetal circulation throughout gestation.

3.A. Appendix: Validation of the lumped model for assessing the AoI flow profile

3.A Appendix: Validation of the lumped model for assessing the AoI flow profile

3.A.1 Study individuals

Both fetuses underwent an ultrasound examination during the third trimester of gestation using a Siemens Sonoline Antares machine (Siemens Medical Systems, Malvern, PA, USA) which included estimation of fetal weight and umbilical artery (UA), middle cerebral artery (MCA), aortic isthmus (AoI), aorta and pulmonary artery Doppler waveforms. The UA pulsatility index (PI) was evaluated in a free loop of the umbilical cord. PI was calculated as: systolic velocity minus diastolic velocity divided by time-averaged maximum velocity. The MCA was evaluated in a transverse view of the fetal skull at the level of its origin from the circle of Willis [64]. The cerebroplacental ratio was calculated by dividing MCA and UA PI [63]. AoI flow velocity was obtained either in a sagittal view of the fetal thorax with a clear visualization of the aortic arch or in a cross section of the fetal thorax at the level of the 3-vessel and trachea view [20]. The AoI flow velocity was quantified by measuring the AoI PI and flow index (IFI). The IFI was calculated as: (systolic + diastolic)/systolic velocity integrals. The aortic waveform was obtained from an apical or basal 4-chamber view of the heart, and the pulmonary artery waveform was obtained from a right ventricular outflow tract view. Peak systolic velocity, ejection time and heart rate were measured from both aortic and pulmonary artery flows. The diameters of the aortic and pulmonary valves were measured in frozen real-time images during systole by the leading-edge-to-edge method [65]. The relative cardiac output (CO) was computed as the ratio between right (RCO) and left (LCO) CO. The angle of insonation was kept as close as possible to 0° and always below 30° . Upon delivery, gestational age, birth weight, birth weight centile, mode of delivery, Apgar scores, presence of preeclampsia and length of stay at the neonatal intensive care unit were recorded.

3.A.2 Patient-specific fitting

Patient-specific blood velocity waveforms from aorta, pulmonary artery, AoI and MCA were obtained by manual delineation of the envelope of the Doppler blood velocity traces (V_M) of the two normal fetuses using a custom graphical user interface (GUI) implemented in *MATLAB (2013b, The MathWorks Inc., Natick, MA)*. The flow rates (Q_{Ao} , Q_{pA} , Q_{AoI} and Q_{MCA} ; pA denotes pulmonary artery and Ao aorta) could be obtained from V_M taking into account the hemodynamic conditions and the shape of the velocity profile. Details on obtaining the flow waveforms from the Doppler recordings are explained in the section 3.B.1 of the supplementary methods.

3.A. Appendix: Validation of the lumped model for assessing the AoI flow profile

The lumped model was personalized to the two normal fetuses. To do this, the specific blood flows functions Q_{Ao} and Q_{pA} obtained from the measured aortic and pulmonary artery flows for each fetus were used as inputs of the model. The gestational age and the fetal estimated weight were used to compute the values of the different components of the model, as described in our previous work [97]. A set of 12 parameters to be estimated automatically were selected. These were: (1) the delay between the onset of pulmonary and aortic ejections, because this was impossible to accurately measure non-invasively by echocardiography; (2)-(5) the vascular bed resistances: brain, upper body, lungs and lower body & placenta resistances; (6)-(9) the vascular bed compliances: brain, upper body, lungs and lower body & placenta compliances; and the arterial Young's modulus of the (10) ascending aorta, pulmonary arteries, aortic isthmus and ductus arteriosus, (11) cerebral arteries and (12) descending aorta. These 12 parameters were estimated automatically using a constrained nonlinear optimization algorithm minimizing the error between the model-based and measured blood velocity waveforms of the AoI (V_{AoI}) and the MCA (V_{MCA}), implemented in *MATLAB*. Details on the optimization process can be found in the section 3.B.2 of the supplementary methods.

3.A.3 Results of the validation of the lumped model for assessing AoI flow profile

Ultrasound and perinatal data of the two normal fetuses used for the model validation are shown in Table 3.1. In both fetuses, the ejection time (ET) of the right ventricle was longer than that in the left ventricle, with a more pronounced difference in the fetus with an end-systolic peak of reversal flow in the AoI. In addition, the aortic time-to-peak velocity was longer than in the pulmonary artery. In both cases, the lumped model was able to reproduce the measured blood velocity waveforms in the AoI and MCA, as shown in Figure 3.3. The AoI blood velocity waveform of the fetus of 29 weeks of gestation showed a small (non-reversing) notch at the end of systole. However, a remarked peak of reversal flow at the end of systole can be observed in the AoI blood velocity waveform of the fetus of 35 weeks of gestation. This phenomenon was successfully reproduced by our lumped model. The estimated parameters after the nonlinear optimization are shown in Table 3.2. The estimated delay in the onset of ejection between pulmonary artery and aorta blood flows was larger in the fetus with end-systolic peak of reversal flow compared to the fetus showing only a small (non-reversing) notch in the AoI waveform at the end of systole (3.8 ms vs. 0.09 ms).

3.B Supplementary methods

3.B.1 Obtaining blood flow waveforms from Doppler recordings

Patient-specific blood velocity waveforms were obtained by manual delineation of the envelope of Doppler velocity traces (V_M). The flow rates (Q) could be obtained from V_M taking into account the hemodynamic conditions and the shape of the velocity profile (parabolic or flat) represented by the Womersley number (W). The Womersley number is a dimensionless parameter calculated as:

$$W = D \sqrt{\frac{f\pi}{2\nu}} \quad (3.1)$$

where D is the vessel diameter, ν the blood viscosity and f the frequency given by the heart rate. Flow rates could thus be computed as:

$$Q = V_M \pi (D/2)^2 k \quad (3.2)$$

where k depends on the Womersley number and was calculated as described by Ponzini et al [102]. In the case of the aortic (Q_{Ao}) and pulmonary (Q_{pA}) flows, k was considered 1.0.

3.B.2 Patient-specific fitting

A constrained nonlinear optimization algorithm minimizing the normalized root mean square error (NRMSE) between the model-based (denoted by \sim) and measured blood velocity waveforms of the AoI (V_{AoI}) and MCA (V_{MCA}), was implemented in *MATLAB* to automatically estimate the patient-specific set of parameters. To ensure that the model estimates correctly both systolic and diastolic values of the blood velocity waveforms, the relative error between model-based and measured systolic and diastolic values of each blood velocity profile was also minimized. Therefore, an objective function J was defined as the sum of individual relative errors as:

$$J = \sum_{i=AoI, MCA} \left[\frac{\sqrt{\frac{1}{N} \sum_{t=1}^N (\tilde{V}_i(t) - V_i(t))^2}}{\max(V_i(t)) - \min(V_i(t))} + \left| \frac{\tilde{V}_i(t_{sys}) - V_i(t_{sys})}{V_i(t_{sys})} \right| + \left| \frac{\tilde{V}_i(t_{dias}) - V_i(t_{dias})}{V_i(t_{dias})} \right| \right] \quad (3.3)$$

where i indicates one of the two locations of the fetal circulation where blood velocity were measured: AoI or MCA; N is the number of time points and t_{sys} and t_{dias} are the systolic and diastolic time points respectively. Model-based blood velocity waveforms were computed from the

model-based blood flow waveforms using the equation 3.2. Therefore, the estimation problem consisted on searching the parameters set which minimizes J (equation 3.3). The minimization algorithm was performed iteratively until the objective function J reached a predefined minimum. The initial parameter set was chosen randomly within a physiological range. Finally, to avoid local minimum solutions, we repeated the procedure several times with different initial parameter sets, and we finally chose the parameter set with a minimum value of J .

3.B.3 Aortic and pulmonary artery blood flows definition

Blood velocity profiles of the right and left ventricular outflows show different shapes. The left ventricular outflow velocity profile is characterized by a rapid rise of velocity and a slower and homogeneous decrease during systole (Figure 3.2(a)). However, the blood velocity profile of the right ventricular outflow has a faster rise of velocity compared to the left, with smaller systolic peak velocity followed by two well differentiated phases of deceleration of the velocity, the first one slower than the second (Figure 3.2(c)). Both velocity profiles could be described with five characteristic time points, as shown in Figure 3.2(b) and 3.2(d). The first point ($p_1 = (t_1, v_1)$) indicates the initiation of the ejection, and usually is set to $p_1 = (0, 0)$. The second one ($p_2 = (t_2, v_2)$) represents the peak systolic velocity and the time to peak velocity (TPV) or acceleration time; the third one ($p_3 = (t_3, v_3)$) corresponds to the end of the first deceleration of velocity phase; the fourth one ($p_4 = (t_4, v_4)$) indicates the end of the ejection and finally, the fifth point ($p_5 = (t_5, v_5)$) is determined by the heart rate. Then, left ($V_L(t)$) and right ($V_R(t)$) velocity functions could be defined as a set of four straight lines built from the 5 points described above ($t_{1..5}, v_{1..5}$) as follows:

$$V_i(t) = \begin{cases} a_1t + b_1 & t_1 < t < t_2 \\ a_2t + b_2 & t_2 < t < t_3 \\ a_3t + b_3 & t_3 < t < t_4 \\ 0 & t_4 < t < t_5 \end{cases} \quad (3.4)$$

where i denotes R or L for the left and right ventricular outflows, respectively. Time point t_1 defines the onset of ejection and therefore the pre-ejection period (PEP), $t_2 - t_1$ corresponds to the TPV , $t_4 - t_1$ to the ET , $t_3 - t_2$ is the duration of the slow deceleration of ejection and $t_5 - t_1$ is determined by the waveform period calculated from the heart rate (HR) as: $T = 60/HR$, where HR can be estimated according to the gestational age as follows [40]:

$$HR(bpm) = 0.67GA + 162 \quad (3.5)$$

3.B. Supplementary methods

TPV was calculated for both aortic (Ao) and pulmonary artery (pA) blood velocities using the following relationships estimated from DeVore [103]:

$$TPV_{Ao}(ms) = 0.31GA + 36.25 \quad (3.6)$$

$$TPV_{pA}(ms) = -0.33GA + 44.66 \quad (3.7)$$

where GA is the gestational age in weeks. ET was considered to be $0.41T$ as measured manually from the Doppler velocity profiles shown in Figure 3.2(a) and 3.2(c). Time points t_3 were measured also manually and were set to $0.36ET$ and $0.6ET$ for the aortic and pulmonary artery velocity profiles respectively. Since initial and diastolic velocities were $0cm/s$, v_1 , v_4 and v_5 were set to 0. Finally, the height of the third point (v_3) was also measured manually from the Doppler profiles shown in Figure 3.2(a) and 3.2(c) and considered to be $0.86v_2$.

After calculating the different coefficients for the three straight lines ($a_{1...3}$ and $b_{1...3}$) for both aortic and pulmonary artery velocity profiles, blood velocity functions were smoothed with a low pass filter. Then, blood flow functions were obtained from velocity functions as:

$$Q_i(t)(ml/s) = V_i(t) \frac{CO_i}{VTI(V_i(t))HR} \quad (3.8)$$

where CO_i is the cardiac output ($i = L$ or R), calculated according to the gestational age of the fetus using the following relationships defined by Kiserud et al [56]:

$$CO_L(ml/min) = \exp(6.25 - 974.15GA^{-2} + 8.08 \cdot 10^{-6}GA^3) \quad (3.9)$$

$$CO_R(ml/min) = \exp(5.83 - 722.67GA^{-2} + 2.36 \cdot 10^{-5}GA^3) \quad (3.10)$$

where GA is the gestational age expressed in weeks. $VTI(V_i(t))$ is the velocity time integral of the velocity function $V_i(t)$.

3.B.4 Single parametric studies

In the simulations, the model parameters were set with their corresponding nominal values calculated for a healthy fetus of 33.4 weeks of gestation and estimated fetal weight of 2200 gr. The HR was 139.62 bpm according to the expression of Van Den Wijngaard et al. [40] (equation 3.5). The nominal values of the 5 variables were: $Tsd_{pA} = Tsd_{Ao} = 16.7$ ms, $ET_{pA} = ET_{Ao} = 176.2$ ms, $PEP_{pA} = PEP_{Ao} = 0$ ms, $TPV_{pA} = TPV_{Ao} = 46.7$ ms and RCO/LCO

= 1.0. The blood flow waveforms used as inputs of the lumped model were constructed with four straight lines characterized by 5 points as shown in Figure 3.2. Details on the blood flows functions construction can be found in the previous section (supplementary methods 3.B.3). The variables under study were:

1. **Difference in the duration of slow deceleration of ejection.** This was defined as the difference between the pulmonary artery and aorta durations of the slow deceleration of ejection: $Tds_{pA} - Tds_{Ao}$. Manual measurements were performed to estimate Tds in both aortic and pulmonary artery flows. According to our manual measurements (Figure 3.2), Tds_{pA} was estimated in 59.0 ms and Tds_{Ao} in 16.7 ms. Therefore, 10 different blood flow inputs were constructed varying Tds_{pA} from its nominal value 16.7 ms to 80.1 ms, leading to a variation of $Tds_{pA} - Tds_{Ao}$ from 0 to 63.4 ms. The remaining variables were kept to their nominal value for both aortic and pulmonary flow functions.
2. **Difference in the duration of RV-LV ejection.** This was calculated as the difference in the ejection duration between pulmonary artery and aortic flows: $ET_{pA} - ET_{Ao}$. The average \pm std ejection duration of right and left ventricles was estimated in 174 ± 12 and 171 ± 11 ms respectively by Fouron et al. [16], so that the maximum difference in the ejection duration between both ventricles was 26 ms. Therefore, 10 different blood flow inputs were constructed varying the ET_{pA} from 176.2 ms to 206.2 ms, leading to a variation of $ET_{pA} - ET_{Ao}$ from 0 to 30 ms. The remaining variables were kept to their nominal value for both aortic and pulmonary flow functions.
3. **Delay in the onset of RV-LV ejection.** This was calculated as the difference in the initiation of the ejection between pulmonary artery and aortic blood flows: $PEP_{pA} - PEP_{Ao}$. The average value of the PEP of right and left ventricles reported by Acharya et al. was 57 and 48 ms respectively [19, 92], meaning a difference of 9 ms between right and left. Therefore, 10 different blood flow inputs were constructed varying $PEP_{pA} - PEP_{Ao}$ from 0 to 10 ms. The remaining variables were kept to their nominal value for both aortic and pulmonary flow functions.
4. **Difference between time-to-peak RV-LV velocities.** This was calculated as the difference between pulmonary artery and aorta time to peak velocities: $TPV_{pA} - TPV_{Ao}$. Machado et al. [93] documented that, between 16 and 30 weeks, the TPV was significantly shorter in

3.B. Supplementary methods

the pulmonary artery than in the aorta (32.1ms vs. 43.7ms), and Sutton, et al. [94] have confirmed these findings, and reported a mean TPV of 39.4ms and 44.6ms respectively in fetuses from 20 to 42 weeks of gestation. Therefore, 10 different blood flow inputs were constructed in which TPV_{Ao} remained unchanged and equal to its nominal value, and the TPV_{pA} was varied to obtain a variation of $TPV_{pA} - TPV_{Ao}$ from -12 to 0 ms. The remaining variables were kept to their nominal value for both aortic and pulmonary flow functions.

5. **Relative CO.** 10 different blood flow inputs were constructed in which RCO/LCO was varied from 1.0 to 1.5, without changing the total CO. The remaining variables were kept to their nominal value for both aortic and pulmonary flow functions.
6. **Pulmonary vasculature compliance.** 10 different scale factors were defined from 0.5 to 2.0. Main, right and left pulmonary arteries and lung compliances were scaled according to the defined scale factors. The rest of vascular parameters and the timing variables for both aortic and pulmonary flow functions were kept to their nominal value.
7. **Lung resistance.** 10 different scale factors were defined from 0.5 to 2.0. Lung resistances were scaled according to the defined scale factors. The rest of vascular parameters and the timing variables for both aortic and pulmonary flow functions were kept to their nominal value.

3.B.5 Multi parametric analysis

Similarly to the single parametric studies, the 5 selected variables: (1) $Tds_{pA} - Tds_{Ao}$, (2) $ET_{pA} - ET_{Ao}$, (3) $PEP_{pA} - PEP_{Ao}$, (4) $TPV_{pA} - TPV_{Ao}$ and (5) RCO/LCO ratio were varied between the same ranges of values as in the single parametric studies. However, to decrease the computational cost, 5 different values for each variable within the defined range were considered instead of 10, as was done before.

The model-based AoI flow waveforms obtained in each simulation were quantified by first detecting the presence or not of the end-systolic notch. Then, if the notch was present, the amplitude of the end-systolic notch (or brief end-systolic peak of reversal flow) was obtained. Also the difference of flow between aortic and pulmonary flows was computed, and the integral (the amount) of the blood flow during the deceleration of ejection was obtained. The correlation between this amount of differential flow and the end-systolic notch in the AoI flow was computed.

A linear regression model was constructed to evaluate the relationship between the AoI end-systolic notch and the 5 variables. The regression equation was:

$$Y = \beta_0 + \sum_{i=1}^5 \beta_i X_i + \varepsilon \quad (3.11)$$

where the dependent variable Y represents the AoI end-systolic notch amplitude and the independent variables X_i correspond the 5 variables under study, calculated as $X_1 = Tds_{pA} - Tds_{Ao}$, $X_2 = ET_{pA} - ET_{Ao}$, $X_3 = PEP_{pA} - PEP_{Ao}$, $X_4 = TPV_{pA} - TPV_{Ao}$ and $X_5 = RCO/LCO$.

3.B.6 Simulating the advance of gestation

The relationship between the appearance of the end-systolic notch in the AoI flow and the gestational age was also evaluated. Firstly, the influence on the AoI flow waveform of the change in total cardiac output, as well as growing fetal vasculature with gestational age was evaluated separately from any differential change in LV and RV outflows. To do this, we considered both aortic and pulmonary flow profiles equal and without changing any of the flow functions' variables with the gestational age, only the total amount of ejected blood for each gestational age as well as the properties and size of the vasculature was varied. Then, in order to evaluate if the scaling function used to describe the variation on the lung compliance throughout the gestation may affect the appearance of the end-systolic notch in the AoI waveform, two modifications of the scaling function were done:

1. A steeper (but still increasing with gestational age) scaling function.
2. A decreasing with gestational (inverse) scaling function.

Next, the differential changes in RV-LV output were added by constructing the specific blood flow inputs considering the expected values for the aortic and pulmonary amount of flow (equations 3.9 and 3.10), aortic and pulmonary TPV , (equations 3.6 and 3.9), and heart rate (equations 3.5) for each gestational age. As described in previous sections, the pulmonary artery velocity function was characterized by two differentiated deceleration periods, so we considered also this difference in the simulations. However, we did not find any data about the relationship between PEP , ET and the gestational age, so we kept ET_{pA} and ET_{Ao} equals to $0.41T$ (where T was $60/HR$), and did not consider any delay in the onset of ejection between both ventricles, so $PEP_{pA} - PEP_{Ao} = 0$ ms. The gestational age was varied from 25 to 37 weeks. In each simulation, the components of the lumped

3.B. Supplementary methods

model were set with their adequate values calculated according to the gestational age and normal fetal weight (W_0) for each gestational age. W_0 was estimated as $\log_{10}(W_0) = 0.2508 + 0.1458GA - 0.0016GA^2$ [84].



Patient-specific estimates of vascular
and placental properties in
growth-restricted fetuses based on a
model of the fetal circulation

Abstract — Intrauterine growth restriction (IUGR) due to placental insufficiency is associated with blood-flow redistribution in order to maintain perfusion to the brain. However, some hemodynamic parameters that might be more directly related to staging of the disease cannot be measured non-invasively in clinical practice. For this, we developed a patient-specific model of the fetal circulation to estimate vascular properties of each individual. A lumped model of the fetal circulation was developed and personalized using measured echographic data from 37 normal and IUGR fetuses to automatically estimate model-based parameters. A multivariate regression analysis was performed to evaluate the association between the Doppler pulsatility indices (PI) and the model-based parameters. The correlation between model-based parameters and the placental lesions was analyzed in a set of 13 IUGR placentas. A logistic regression analysis was done to assess the added value of the model-based parameters relative to Doppler indices, for the detection of fetuses with adverse perinatal outcome. The estimated model-based placental and brain resistances were respectively increased and reduced in IUGR fetuses while placental compliance was increased in IUGR fetus. Umbilical and middle cerebral arteries PIs were most associated with both placental resistance and compliance, while uterine artery PI was more associated with the placental compliance. The logistic regression analysis showed that the model added significant information to the traditional analysis of Doppler waveforms for predicting adverse outcome in IUGR. The proposed patient-specific computational model seems to be a good approach to assess hemodynamic parameters than cannot be measured clinically.

Adapted from: Garcia-Canadilla P, Crispi F, Cruz-Lemini M, Triumfo S, Nadal A, Valenzuela-Alcaraz B, Rudenick PA, Gratacos E, Bijmens BH. *Patient-specific estimates of vascular and placental properties in growth-restricted fetuses based on a model of the fetal circulation*. Submitted, 2015

4.1 Introduction

Intrauterine growth restriction (IUGR) from placental insufficiency is one of the leading causes of perinatal mortality/morbidity [8, 104]. IUGR is associated with blood-flow redistribution that involves several vessels of the fetoplacental circulation, such as the aortic isthmus (AoI), middle cerebral artery (MCA) and the umbilical artery (UA). This blood-flow redistribution due to IUGR is thought to be caused by the increase in the placental and peripheral resistances and the decrease of brain resistance due to cerebral arteries vasodilation, and is associated with worse perinatal, neurodevelopmental and cardiovascular outcome [14, 49, 51–53]. In clinical practice these fetal hemodynamic changes are evaluated by quantifying the Doppler flow-velocity waveforms using empirical indices such as the systolic to diastolic (S/D) ratio and the pulsatile indices (PI). However, in some small for gestational age (SGA) fetuses, placental histological changes compatible with placental under-perfusion were identified without changes in the Doppler indices [105, 106]. Moreover, signs of placental under-perfusion have been associated with an increased risk of neonatal morbidity [107, 108] and abnormal neurodevelopmental outcome [105].

It is commonly believed that an increase in the pulsatility of the arterial flow is caused by an increase in vascular resistance. Several studies in an IUGR sheep model [109–113], or using an electrical-analog model of the placenta circulation [40, 111, 113–115], have evaluated the association between different alterations in vascular structures and beds with the Doppler measurements in the umbilical and also in uterine artery (UtA). These studies supported that the UA–PI is directly related to high placental and low UA resistance or a combination of high placental resistance and UA wall abnormalities. However, in other studies, using vasoactive agents to increase resistance, a poor correlation between pulsatility and resistance was found. In the UtA, similarly to the UA, some fetal sheep studies [112] demonstrated that when the placental microcirculation was occluded, resistance was increased and abnormal Doppler waveforms were observed. However, UtA Doppler is also influenced by maternal factors [116], and therefore abnormal patterns could not be explained only by the changes in placental vasculature. Thus, there are several hemodynamic factors that can lead to abnormal Doppler waveforms in both UA and UtA, and not all changes originate from an increase in placental resistance.

All these studies were performed in animal models or using electrical equivalent models. However, it is not feasible to study, in-vivo and non-invasively, the underlying hemodynamic determinants of the Doppler waveforms in different vessels in human fetuses and alternative approaches need to be used. To better understand hemodynamic remodeling, a patient-

specific model of the fetal circulation can be used to estimate different vascular and hemodynamics properties of each patient that cannot be assessed during the ultrasonography evaluation. Despite that several models of the fetal circulation have been developed, only few of them were patient-specific [97,99]. Our purpose was to use a lumped model of the fetal circulation to estimate patient-specific vascular and placental properties of normal and IUGR fetuses. This might help in the understanding of IUGR and its underlying mechanisms and to compare the diagnostic performance of those variables for prediction of increased risk of adverse perinatal outcome.

4.2 Methods

4.2.1 Study population

Ultrasonographic data from IUGR and normally grown fetuses (controls) were used to fit the computational model. IUGR and control fetuses were selected from singleton pregnancies who attended for routine hospital visit in the third trimester of pregnancy at the Maternal-Fetal Medicine Department at BCNatal in Barcelona between January 2010 and April 2014. IUGR was defined as an estimated fetal weight (EFW) [61] and confirmed birth weight below the 10th centile according to local reference curves [62] together with a pulsatility index (PI) in the UA above 2 standard deviations [63]. Controls were selected among non-complicated pregnancies with EFW and birth-weight above 10th centile [104]. Pregnancies with structural/chromosomal anomalies or evidence of fetal infection were excluded from the study. The study protocol was approved by the local Ethics Committee and parents provided written informed consent.

In all fetuses, biometrics and feto-placental Doppler by ultrasound were performed using a Siemens Sonoline Antares machine (Siemens Medical Systems, Malvern, PA, USA). EFW was calculated from the biparietal diameter, head and abdominal circumference, and femur length using the Hadlock formula [61]. Feto-placental Doppler examination included the evaluation of flow velocities in the UA, UtA, MCA, AoI, right and left ventricle (RV and LV) outflow tracks. UA was evaluated in a free loop of the umbilical cord. MCA was measured in a transverse view of the fetal skull at the level of its origin from the circle of Willis [64]. For UtA assessment, the ultrasound probe was placed on the lower quadrant of the abdomen, angled medially, and color Doppler imaging was used to identify the UtA at the apparent crossover with the external iliac artery. Mean UtA-PI was calculated as the average PI of the right and left arteries. Cerebroplacental ratio was calculated by dividing MCA and UA PI. PI was calculated as: (systolic – diastolic) velocities divided by time-averaged maximum velo-

4.2. Methods

city. AoI flow velocity was recorded either in a sagittal view of the fetal thorax with a clear visualization of the aortic arch or in a cross section of the fetal thorax at the level of the 3-vessel and trachea view. The AoI-PI and flow index (IFI) were measured. The IFI was calculated as: (systolic + diastolic)/systolic velocity integrals. LV outflow was imaged in an apical or basal 5-chamber view of the heart at the aortic outflow tract, and RV outflow was obtained in a RV outflow tract view. Peak systolic velocities of both LV and RV outflow, ejection time and heart rate were measured. Doppler recordings were done in absence of fetal movements and, when required, with voluntary suspended maternal breathing. The angle of insonation between the vessel and the Doppler beam was kept as close as possible to 0° and always below 30° . Doppler parameters were obtained from three or more successive waveforms in each vessel. Finally, diameters of the aortic and pulmonary artery valves were measured in frozen real-time images during systole by the leading edge-to-edge method [65].

At delivery, gestational age, birth weight, birth weight centile, mode of delivery, Apgar scores, umbilical pH, presence of preeclampsia and length of stay at the neonatal intensive care unit were also recorded. Adverse perinatal outcome was defined as the presence of at least one of the following: umbilical artery pH < 7.15 , 5-min APGAR score < 7.0 , admission to neonatal care unit for a period of at least 25 days or intervention for fetal distress.

4.2.2 Patient-specific modeling

Lumped model of the fetal circulation

An improved version of our previous model of the fetal circulation [97] was implemented. New arterial segments and vascular beds of the downstream fetal circulation were included. Specifically, the descending aorta was replaced by a thoracic and abdominal aorta, two iliac and two umbilical arteries. The peripheral vascular bed was replaced by two kidneys, two lower body and two placental vascular beds. Therefore the model consisted of 19 arterial segments and 13 vascular beds as shown in Figure 4.1.

As described in Garcia-Canadilla et al. [97], the equivalent electrical lumped model was constructed by interconnecting two different building blocks: (1) the arterial segment, which included a capacitor (C), a resistor (R) and an inductor (L), representing arterial compliance, resistance of blood flowing in the arterial segment and blood inertia respectively; and (2) the vascular beds, consisting of a three-element Windkessel model, which included a resistor and a capacitor representing the vascular bed resistance and compliance respectively. Therefore, the equivalent electrical lumped

model of the fetal circulation consists of a total of 94 electrical components and 2 inputs, and was implemented in *Simulink MATLAB (2013b, The Math-Works Inc., Natick, MA)*.

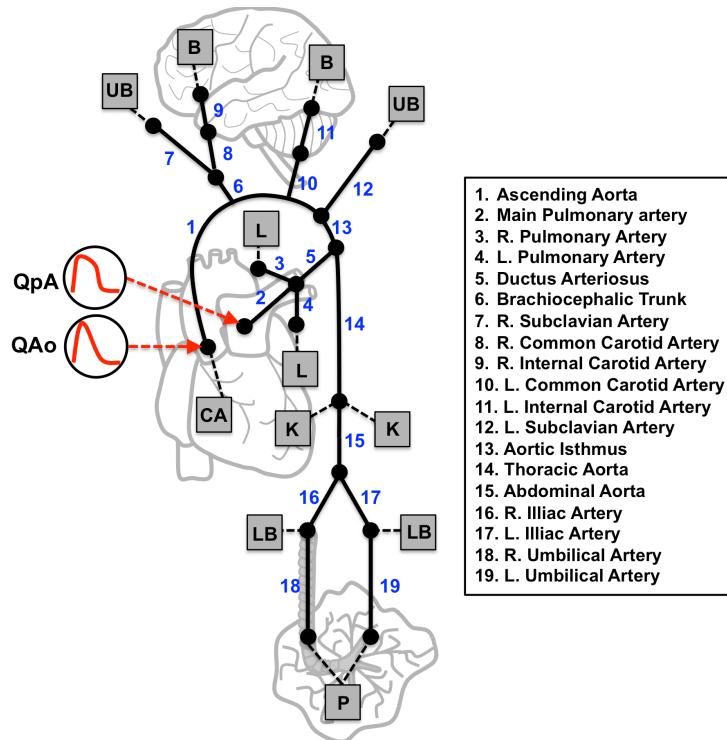


Figure 4.1: A schematic representation of the lumped model of the fetal circulation, composed of 19 arterial segments (black lines), 11 vascular beds (boxes) and 2 blood-flow inputs: QpA and QaAo.

Patient-specific input data

Patient-specific blood velocity waveforms from *RV* and *LV* outflow tracks (V_{RV} and V_{LV}), AoI (V_{AoI}), MCA (V_{MCA}) and UA (V_{UA}) were obtained by manual delineation of the envelope of the Doppler profiles. The corresponding blood flows: Q_{LV} , Q_{RV} , Q_{AoI} , Q_{MCA} and Q_{UA} were calculated. Details on the blood-flow calculation are described in Appendix A (section 4.A).

The gestational age (*GA*) and estimated fetal weight (*EFW*) were used to calculate the different electrical components of the equivalent circuit. The description of the calculation of the electrical components of the model is described in Appendix A (section 4.A).

4.2. Methods

Patient-specific fitting

A diagram of the patient-specific fitting algorithm is shown in Figure 4.2. The input of the model was the set of the patient-specific initial values of all electrical components, and two patient-specific blood-flow inputs: Q_{LV} and Q_{RV} . The output was the model-based blood velocities in the AoI (\tilde{V}_{AoI}), MCA (\tilde{V}_{MCA}) and UA (\tilde{V}_{UA}). In order to fit the model-based blood-flows to the measured ones, an optimization algorithm (implemented in *MATLAB*) was used to estimate a set of 13 model parameters. The set of parameters was estimated automatically for each patient, using a constrained nonlinear optimization algorithm minimizing the error between the model-based and measured blood velocity waveforms of the AoI, MCA and UA. Details on the optimization process can be found in the Appendix B (section 4.B).

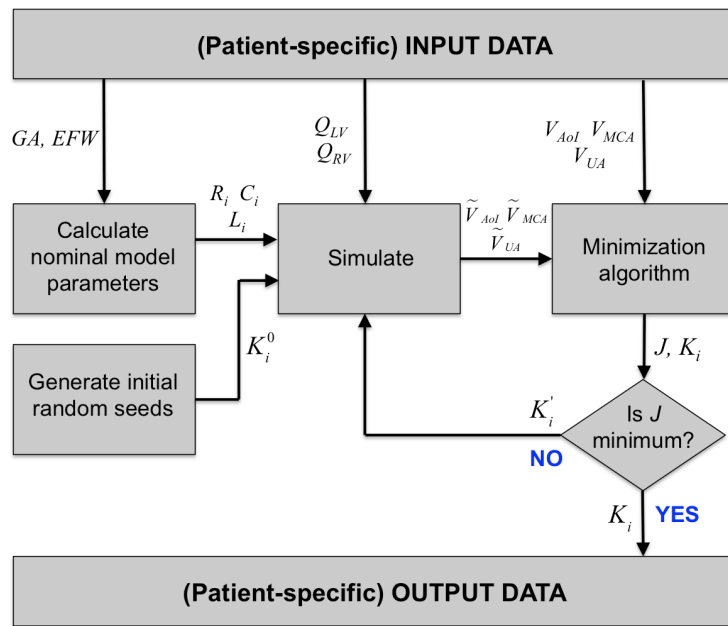


Figure 4.2: Block diagram of the implemented algorithm for the patient-specific fitting.

4.2.3 Placental evaluation

Placental examinations adhered to standard laboratory protocol. Fresh and trimmed (after removal of the membranes, cord, and any blood clots) placental weight was recorded. Trimmed placental weight centiles were assigned based on GA-specific placental weight charts [117]. The fetoplacental

weight ratio (birth weight: fresh placental weight) was also expressed as a percentile, drawn from GA-specific ranges [118].

Placentas were fixed in 10% buffered formalin. After gross examination, samples of each specimen were taken for routine processing: one transverse section of cord, one rolled strip of membranes, and three blocks of villous parenchyma. All macroscopic lesions were sampled as well. Finished slides were hematoxylin and eosin-stained. A single senior pathologist (AN) supervised all examinations.

Using a hierarchical and standardized classification system, as previously described by our group, histologic manifestations were further designated as maternal or fetal in origin, defined as placental under-perfusion (PUP) [119–121]. Among maternal vascular supply disruptions, specific vascular alterations qualifying for maternal vascular maldevelopment were: superficial implantation/decidual arteriopathy (acute atherosclerosis and mural hypertrophy [mean wall diameter >30% of overall vessel diameter of arterioles in the decidua parietalis]), undergrowth/distal villous hypoplasia (decrease in the number and modal diameter of distal villi at the center of the lobule after adjustment for plane of section and gestational age, in the lower 75% of a full-thickness section), excessive intervillous fibrin (basal layer of fibrinoid material involving >30% of the placental maternal surface) and migration disorders. Specific vascular alterations qualifying for maternal vascular obstruction were: syncytial knots involving terminal villi (affecting >50% of the terminal villi), villous agglutination (>50%), intervillous fibrin deposition (eccentric aggregates on intervillous fibrin on proximal and distal villi affecting >50% of the villi) and villous infarcts (>30% of villous loss). Specific vascular alterations qualifying for maternal vascular loss of integrity were: arterial rupture (abruption placenta), venous rupture (acute chronic marginal abruption). Among fetal vascular supply disruptions, lesions qualifying for maldevelopment were: chorioangioma, chorioangioma and distal villous immaturity. Lesions qualifying for obstruction were considered those secondary to vascular thrombo-occlusive disease (thrombosis of chorionic plate and stem villous channels and villous avascularity affecting large groups).

To address reliability, a sample of 7 placentas were randomly selected and blindly re-assessed by the same pathologist: overall agreement was 85% (6/7), underdiagnosis in the first relative to the second review occurred in only one case and overdiagnosis in none case.

4.2.4 Statistical analysis

A student's t-test and Pearson chi-square test were used to compare quantitative and qualitative data, respectively between groups. A multivariate re-

4.3. Results

gression analysis was performed to evaluate the association between Doppler parameters and different hemodynamic variables. Finally, associations between different Doppler and model-based parameters and IUGR and adverse perinatal outcome were analyzed by multiple logistic regressions using *SPSS 17.0*.

4.3 Results

4.3.1 Study population

A total of 48 fetuses were initially included in the study (median gestational age at fetal ultrasound: 31.4 weeks; range: 27.4-38.6). Patient-specific fitting was successfully performed in 37 fetuses, which represents a success rate of 77%, including 15 IUGR cases and 22 controls. Table 4.1 compares the fetoplacental ultrasonographic data and perinatal outcome by study group. As expected, birthweight and gestational age at delivery were significantly lower in IUGR with worse fetoplacental Doppler and perinatal outcome.

Table 4.1: Doppler parameters before delivery and perinatal characteristics of normally grown (control) and IUGR fetuses

	Control (n=22)	IUGR (n=15)	p*
Fetoplacental ultrasound			
AoI-PI (Z-score)	-0.32 ±	18.39 ±29.77	0.005
IFI (Z-score)	0.49 ± 0.87	-5.59 ± 7.50	0.001
MCA-PI (Z-score)	0.27 ± 0.96	-1.26 ± 0.95	<0.001
UA-PI (Z-Score)	-0.18 ± 0.57	2.33 ± 1.90	<0.001
CPR (Z-Score)	0.23 ± 1.00	-2.35 ± 0.99	<0.001
UtA-PI (Z-score)	-0.64 ± 1.25	2.01 ± 2.09	<0.001
Perinatal outcome			
Gestational age at delivery (weeks)	39.87 ± 1.81	34.29 ± 3.38	<0.001
Birth weight (grams)	3334 ± 536	1501 ± 556	<0.001
Birth-weight centile	55 ± 24	0 ± 1	<0.001
Pre-eclampsia	0	4 (26.7)	<0.001
1 min APGAR score ≤ 7.0	0	3 (20)	<0.001
UA or UV pH at delivery ≤ 7.15	3 (13.6)	0 (0)	<0.001
Stillbirth	0	0	-
Fetal distress	2 (9.1)	2 (13.3)	0.683
Days in NCIU	0 ± 0	25 ± 22	<0.001
Neonatal morbidity	0 (0)	8 (53.3)	<0.001
Neonatal mortality	0 (0)	1 (6.7)	<0.001

Data are given as mean ± SD or n (%). *Student's t-test for independent samples or Pearson test. IUGR, intrauterine growth restriction; AoI, aortic isthmus; IFI, isthmic flow index; MCA, middle cerebral artery; UA, umbilical artery; CPR, cerebroplacental ratio; UtA, uterine artery; PI, pulsatility index; UV, umbilical vein; NCIU, neonatal intensive care unit.

4.3.2 Model-based parameters and fetoplacental Doppler

Figure 4.3 shows the measured and model-based velocity waveforms in the AoI, MCA and UA for a control (4.3(a)-(f)) and IUGR fetus (4.3(g)-(l)). Table 4.2 shows the model-based parameters obtained for both groups after the minimization process. The estimated placental resistance and compliance were significantly increased in IUGR. On the other hand, coronary artery and brain resistances were significantly lower. There were no significant difference in other model parameters.

Table 4.2: Model-based parameters estimated for all the fetal population

Model-based parameters	Control (n=22)	IUGR (n=15)	p*
K_{RcorA} (coronary artery resistance)	1.11 ± 0.21	0.88 ± 0.24	0.003
K_{rAo} (aorta's radius)	1.02 ± 0.09	0.99 ± 0.16	0.448
K_{Cao} (aorta compliance)	2.60 ± 0.93	2.74 ± 1.10	0.698
K_{rba} (brain arteries' radius)	1.17 ± 0.20	1.08 ± 0.27	0.234
K_{Cba} (brain arteries' compliance)	0.80 ± 0.60	0.94 ± 0.86	0.554
K_{Rb} (brain resistance)	1.36 ± 0.30	1.01 ± 0.31	0.002
K_{Cb} (brain compliance)	0.46 ± 0.16	0.64 ± 0.56	0.168
K_{Rrest} (rest of peripheral resistance)	0.74 ± 0.24	0.85 ± 0.30	0.226
K_{Crest} (rest of peripheral compliance)	1.09 ± 0.64	1.38 ± 0.69	0.194
K_{ruA} (umbilical arteries' radius)	1.05 ± 0.16	1.08 ± 0.21	0.644
K_{CuA} (umbilical arteries' compliance)	1.65 ± 0.60	1.84 ± 0.70	0.397
K_{Rplac} (placental resistance)	1.04 ± 0.35	3.75 ± 2.23	< 0.001
K_{Cplac} (placenta compliance)	1.99 ± 0.99	3.79 ± 1.81	< 0.001

Data are given as mean ± SD. *Student's t-test for independent samples.

Table 4.3 shows the association between Doppler and model-based parameters by means of multivariate regression. While UA-PI, MCA-PI and CPR showed a significant association with both model-based placenta resistance and compliance, UtA-PI was only significantly associated with the model-based placenta compliance. AoI was significantly associated to coronary artery resistance.

4.3.3 Model-based parameters and placental evaluation

In a total of 13 IUGR placentas (74%), PUP-related histopathology was identified in 8 cases (Table 4.4). Placental weight mean was 313.8gr (± 88.71) and fetoplacental weight ratio 4.69 (± 1.30) respectively.

Figure 4.4 shows the model-based parameters of the 13 cases with placenta histological evaluation, classified in three different groups according to the PUP-related histopathology: normal (n=5), MUP (n=10) and MUP & FUP (n=3). The K_{Rplac} and K_{Cplac} model-based parameters were transformed to $1/K_{Rplac}$ and $1/K_{Cplac}$ respectively to have a normal distribution.

4.3. Results

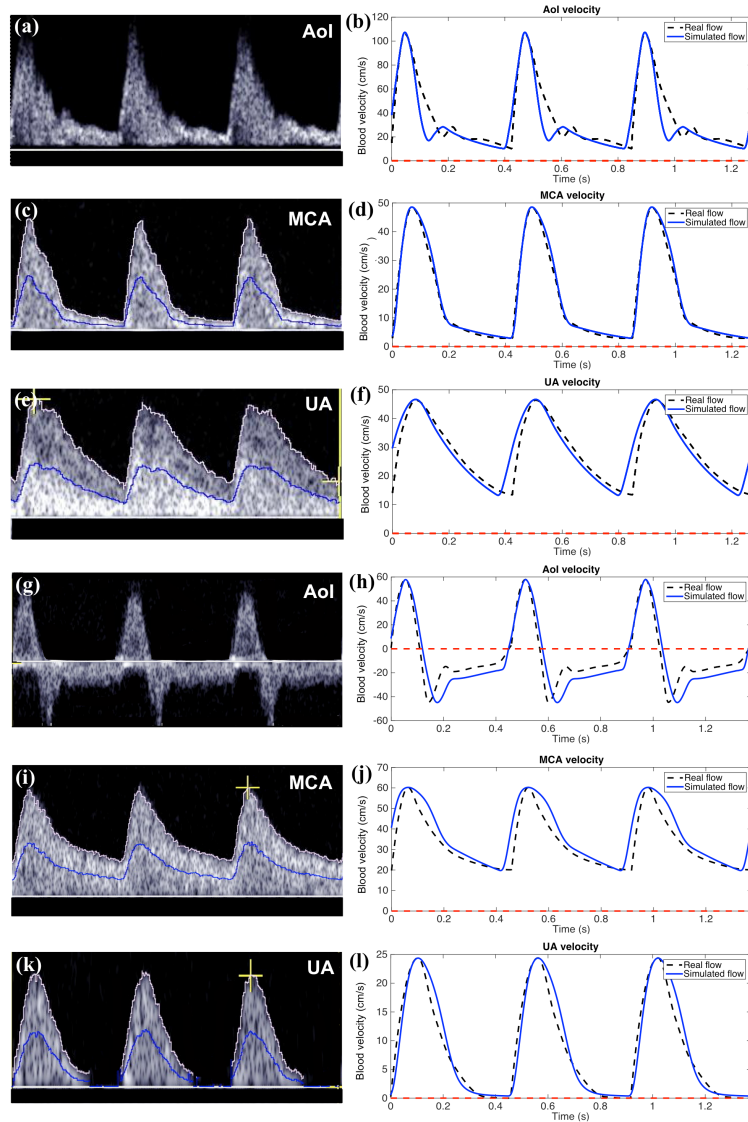


Figure 4.3: (a)-(f) **Left**: Doppler recordings from (a) aortic isthmus (AoI), (c) middle cerebral artery (MCA), and (e) umbilical artery (UA) for a control fetus; **Right**: comparison between estimated (solid line) and measured Doppler velocity waveforms (dash line) in the (b) AoI, (d) MCA and (f) UA. (g)-(l) **Left**: Doppler recordings from (g) AoI, (i) MCA and (k) UA for a IUGR fetus; **Right**: comparison between estimated (solid line) and measured Doppler velocity waveforms (dash line) in the (h) AoI, (j) MCA and (l) UA.

Although the differences between groups were not statistically significant due to the low sample size, those placentas with signs of MUP as well as

FUP showed a linear tendency to have decrease values of both $1/K_{Rplac}$ and $1/K_{Cplac}$. However, the placentas with only signs of MUP showed a linear tendency to have a decrease in K_{Rplac} and not in $1/K_{Cplac}$. Finally, both PUP groups showed a linear tendency to have a decrease in K_{RcorA} .

Table 4.3: Multiregression analysis between the Doppler and the model-based parameters.

	K_{RcorA}	K_{Rb}	K_{Rplac}	K_{Cplac}	R^2
IFI	0.349*	0.117	0.365	0.001	0.464**
MCA-PI	0.021	-0.216	0.569**	-0.382*	0.503**
UA-PI	0.004	-0.20	-0.41*	0.351*	0.555**
CPR	0.105	0.019	0.484**	-0.426**	0.669**
UtA-PI	-0.175	-0.014	-0.220	0.413*	0.402**

* $p < 0.05$ and ** $p < 0.01$. AoI, aortic isthmus; IFI, isthmic flow index; MCA, middle cerebral artery; UA, umbilical artery; CPR, cerebroplacental ratio; UtA, uterine artery; PI, pulsatility index.

Table 4.4: Categories/subcategories of placental attributes (n=13) consistent with under-perfusion in study population.

Categories of placental injury n (%)	Subcategories of placental injury n (%)
Maternal vascular supply 10 (76.9)	Maldevelopment 2 (20)
	Obstruction 8 (80)
	Loss of integrity 0 (0)
Fetal vascular supply 3 (23.1)	Maldevelopment 0 (0)
	Obstruction 1 (33.3)
	Loss of integrity 2 (66.7)

4.3.4 Model-based parameters and perinatal outcome

The results of the logistic regression analysis showed that with model-based parameters, the accuracy, sensitivity and specificity of detecting IUGR fetus was 100%.

Next, the fetal population was classified to have or not have adverse perinatal outcome. Table 4.5 shows the main perinatal data, Doppler indices before delivery and the model-based parameters for both groups. Again, GA at delivery and birth-weight were significantly lower in those fetuses

4.4. Discussion

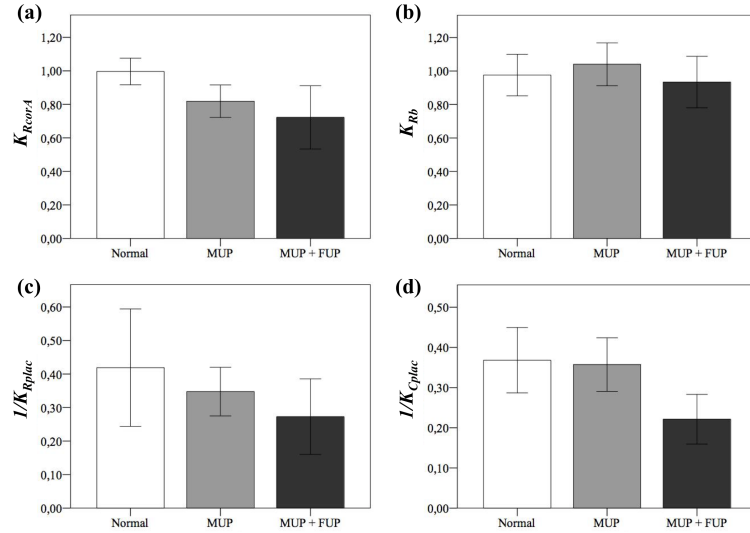


Figure 4.4: (a) Coronary artery resistance (K_{RcorA}), (b) brain resistance (K_{Rb}), (c) placental resistance ($1/K_{Rplac}$) and (d) placenta compliance ($1/K_{Cplac}$) model-based parameters of the 13 cases with placenta histological evaluation. MUP: maternal under-perfusion; FUP: fetal under-perfusion.

that had adverse perinatal outcome. Model-based placental resistance and compliance were significantly higher and brain and coronary resistances were significantly lower in fetuses with poorer perinatal outcome. Figure 4.5 shows the four model-based parameters that were significantly different between the different groups: controls, IUGR and fetuses with adverse perinatal outcome. Table 4.6 shows the results from the logistic regression performed with different sets of Doppler and model-based parameters. Using the Doppler parameters alone, the sensitivity was 72%. On the other hand, GA alone showed a better predictive capacity than Doppler parameters, with a sensitivity of 81.8%. When the estimated model-based parameters were included the detection of adverse perinatal outcome was considerably improved up to a sensitivity of 90%.

4.4 Discussion

We presented a lumped model of the fetal circulation for estimating patient-specific vascular and placental properties. The model was successfully used for evaluating a cohort of 37 control and IUGR fetuses. The results shown that UA and MCA PIs were most associated with both placental resistance and compliance, while UtA-PI was more associated with the placental compliance. Also we demonstrated that adding the model-based parameters to

Table 4.5: Doppler and model-based parameters of the fetal population classified to have or not an adverse perinatal outcome.

	Non-adverse outcome (n=26)	Adverse outcome (n=11)	p*
Doppler parameters			
AoI-PI (Z-Score)	2.31 ± 9.23	18.99 ± 33.55	0.023
IFI (Z-Score)	-0.38 ± 3.92	-5.75 ± 3.92	0.006
MCA-PI (Z-score)	-0.05 ± 1.06	-1.07 ± 1.29	0.016
UA-PI (Z-score)	0.18 ± 1.20	2.41 ± 1.07	<0.001
CPR (Z-Score)	-0.30 ± 1.33	-2.04 ± 1.61	0.002
UtA-PI (Z-score)	-0.05 ± 1.58	1.44 ± 2.69	0.047
Model-based parameters			
K_{RcorA} (coronary artery resistance)	1.08 ± 0.21	0.87 ± 0.26	0.015
K_{Rb} (brain resistance)	1.33 ± 0.33	0.96 ± 0.20	0.001
K_{Rplac} (placental resistance)	1.39 ± 0.92	3.92 ± 2.60	<0.001
K_{Cplac} (placental compliance)	2.32 ± 1.15	3.65 ± 2.21	0.022

Data are given as mean ± SD. *Student's t-test for independent samples. AoI, aortic isthmus; IFI, isthmic flow index; MCA, middle cerebral artery; UA, umbilical artery; CPR, cerebroplacental ratio; UtA, uterine artery; PI, pulsatility index.

Table 4.6: Accuracy, sensitivity and specificity of the logistic regression analysis for detecting adverse perinatal outcome.

	Accuracy	Sensitivity	Specificity
Doppler set	88.6%	72.7%	95.8%
GA	89.2%	81.8%	92.3%
Doppler set + GA	91.4%	81.8%	95.8%
Doppler set + Model set	94.3%	90.9%	95.8%
GA + Model set	94.6%	90.9%	96.2%
Doppler set + GA + Model set	97.1%	90.9%	100%

GA, gestational age at birth; Doppler parameter set includes: UA-PI, MCA-PI, CPR and UtA-PI, all in Z-scores. Model parameter set includes: K_{RcorA} , K_{Rb} , K_{Rplac} and K_{Cplac} .

the conventional Doppler parameters improve the detection of fetuses with adverse perinatal outcome.

Several computational models [35–40, 97, 99, 122] have been developed and used to improve the understanding of the Doppler changes observed in IUGR at different locations in the fetal circulation, such as umbilical and uterine artery. However only few [97, 99] were patient-specific and allow estimation of an individual set of hemodynamic parameters. Our extended lumped model was used to estimate a set of thirteen vascular parameters in a cohort of 22 controls and 15 IUGR fetuses. From this set of estimated parameters, only four were significantly different between groups: placental resistance and compliance were higher and brain and coronary artery resis-

4.4. Discussion

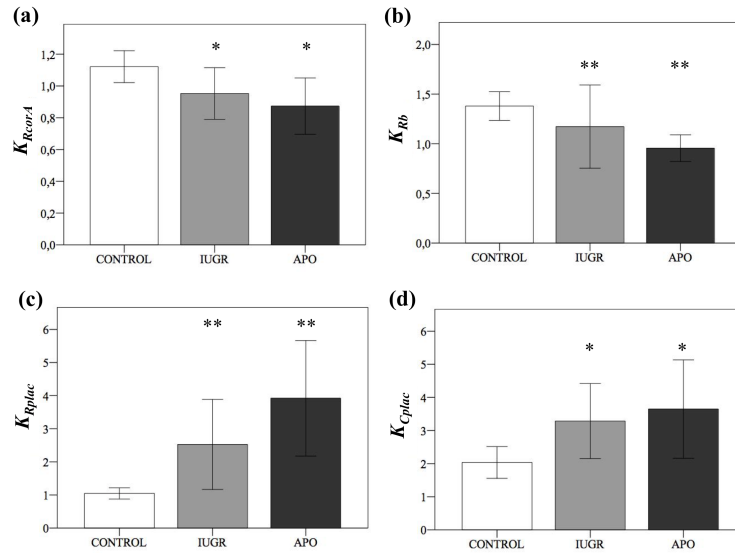


Figure 4.5: (a) Coronary artery resistance (K_{RcorA}), (b) brain resistance (K_{Rb}), (c) placental resistance (K_{Rplac}) and (d) placenta compliance (K_{Cplac}) model-based parameters for the three groups of fetuses: controls, intrauterine growth restriction (IUGR) and with adverse perinatal outcome (APO) fetuses. *p value < 0.05 compared with the control group; **p value < 0.01 compared with control the group.

tances were lower in IUGR fetuses compared to controls. We have shown that while UA-PI, MCA-PI and CPR showed a significant association with both model-based placental resistance and compliance, UtA-PI was only significantly associated with the model-based placenta compliance. This suggests that different Doppler parameters are describing different placental substrates. While UA and MCA most probably reflect an initially abnormal placenta with less developed vasculature (reflected by increased placental resistance), UtA most probably reflects the maternal-fetal interaction that determines placental compliance.

Placental insufficiency can be caused by different patterns of placental changes, such as villous infarcts, villous fibrosis, villous hypovascularity, etc [123, 124]. In fact, when we evaluated the correlation between the model-based parameters and the maternal and/or fetal signs of placental under-perfusion we found that placental compliance showed a tendency to increase only in those cases with both fetal and maternal under-perfusion while the placental resistance showed a tendency to linearly increase with the number of placental lesions. These results support the hypothesis that placental vascular properties' changes are different depending on the origin (maternal and/or fetal) of the lesion. However, in order to further investigate

this, a more detailed model of the placenta would be needed.

We also evaluated the added value of patient-specific model-based parameters in the detection of fetuses with adverse perinatal outcome in comparison to currently used Doppler parameters. When Doppler indices were used alone, the sensitivity and specificity obtained was 72.7% and 95.8% respectively. However, the addition of a set of model-based parameters improved sensitivity for the detection of adverse perinatal outcome to 90%. In a similar study [99], in which four hemodynamic parameters were estimated by a patient-specific fitting in a cohort of 42 fetuses, the addition of these parameters to the conventional Doppler indices also improved the detection of IUGR fetuses. In our study, we used a different set of hemodynamic parameters that seems to perform better in the detection of IUGR fetuses with poorer perinatal outcome. This can be explained by the fact that our set of parameters are more directly related to the disease, placental insufficiency, than the set used by Luria et al. [99], who used parameters more related to blood-flow redistribution.

We acknowledge that our current model has some limitations. Apart from the ones already mentioned in our previous published model [97] this study has some additional limitations. Firstly, a set of only a few parameters was personalized for each fetus, assuming that the rest of parameters were unchanged. This simplification was necessary to make a compromise between complexity and efficiency of the model, and therefore the number of parameters is limited to reduce the number of possible solutions of the inverse problem. In our case, the most relevant parameters that describe the hemodynamics of each patient were included. Secondly, a more complex model of the placental circulation would be required to further evaluate the specific hemodynamic changes in the placenta, and to take into account the maternal factors that can influence the fetal circulation. However, evaluation of the detailed hemodynamic properties of the feto-maternal circulation of the placenta was beyond the scope of this study. Finally, the amount of patients in the study was small. Nevertheless the results look promising to directly assess hemodynamic properties of the fetal circulation rather than using Doppler measurements and to improve the detection of fetuses with adverse perinatal outcome.

4.5 Conclusions

In conclusion, we presented a patient-specific lumped model of the fetal circulation that successfully estimated a set of fetal vascular and hemodynamic properties. Placental and coronary compliance/resistance strongly correlate with feto-placental Doppler parameters, show an association with placental maternal/fetal under-perfusion, and correlate with adverse perinatal

4.5. Conclusions

outcome in IUGR. Therefore, the proposed patient-specific computational model seems to be a good approach to assess hemodynamic and placental parameters than cannot be measured non-invasively in clinical practice.

4.A Appendix A

Patient-specific blood velocity waveforms from right and left output tracks (V_{RV} and V_{LV}), MCA (V_{MCA}), AoI (V_{AoI}) and UA (V_{UA}) were obtained by manual delineation of the envelope of the Doppler blood velocity profiles. The corresponding blood flows: Q_{LV} , Q_{RV} , Q_{MCA} , Q_{AoI} and Q_{UA} were calculated considering the shape (parabolic or flat) of the velocity profiles. This property is described by the Womersley number (W), a dimensionless parameter calculated as: $W = D\sqrt{\pi f/2\mu}$, where D is the vessel diameter, μ is the blood viscosity and f the frequency given by the heart rate. Then, blood flows were calculated accordingly as: $Q_i = V_i\pi(D/2)^2k$, where k is a factor that depends on the Womersley number as described by Ponzini et al. [102].

The gestational age (GA) and the estimated fetal weight (EFW) were used to calculate the different electrical components of the equivalent circuit. Firstly, arterial radius, length and thickness were calculated using the equations described in the Table 4.7, which depends on the GA . Then, in order to describe the changes in the vessel dimensions as a function of EFW , the dimensions of all the arterial segments were scaled according to the following equation: $Y_i = Y_0(EFW/W_0)^{0.33}$ as described by Pennati et al. [83], where W_0 is the reference EFW calculated using the following relationship between the GA and EFW : $\log_{10}(W_0) = 0.2508 + 0.1458 \cdot GA - 0.0016 \cdot GA^2$ [84] with GA in weeks. Blood viscosity was calculated as: $\mu = (1.15 + 0.075 \cdot GA)/100$ [40] with the GA in weeks. The variation of the arterial Young's moduli of each arterial segment with the GA was considered as described by van den Wijngaard et al. [40]. Regarding the vascular bed components, compliances were scaled to their values at each corresponding GA , following the expression reported by van Gemert et al. [101]. Resistances were scaled to obtain a mean blood pressure (MBP) adequate for each GA and calculated as: $MBP(mmHg) = 0.87 \cdot GA + 10.33$ [80].

Then, vascular bed resistances and compliances were also scaled to take into account the body weight, following the equations described in [83] $R_p = R_{p0}(EFW/W_0)^b$ and $C_p = C_{p0}(EFW/W_0)^b$ respectively, where b is the scaling factor that depends on the vascular bed, and R_{p0} and C_{p0} were the vascular bed resistances and compliances respectively, calculated for the specific GA . The scaling factors for the different vascular beds are shown in Table 4.8.

4.B. Appendix B

Table 4.7: Equations describing the dimensions and Young's moduli (E) of the different arterial segments of the fetal circulation included in the lumped model.

Arterial segment	Length (mm)	Diameter (mm)	E (dyn/cm^2)
Ascending Aorta	$-8.61 + 0.88t$	$-2.10 + 0.27t$	$1.57f(t)$
Aortic isthmus	$-2.15 + 0.22t$	$-1.86 + 0.19t$	$1.57f(t)$
Thoracic Aorta	$-19.65 + 2.05t$	$-2.38 + 0.24t$	$1.89f(t)$
Abdominal Aorta	$-14.59 + 1.52t$	$-2.07 + 0.21t$	$4.19f(t)$
Ductus Arteriosus	$-2.41 + 0.31t$	$-2.09 + 0.21t$	$2.83f(t)$
Main pulmonary artery	$-5.60 + 0.57t$	$-2.77 + 0.30t$	$1.57f(t)$
R. pulmonary artery	$-4.00 + 0.41t$	$-1.71 + 0.18t$	$1.57f(t)$
L. pulmonary artery	$-4.00 + 0.41t$	$-1.95 + 0.19t$	$1.57f(t)$
Brachiocephalic Trunk	$-1.06 + 0.29t$	$-1.78 + 0.18t$	$1.89f(t)$
L. subclavian artery	$-2.15 + 0.43t$	$-1.22 + 0.12t$	$2.83f(t)$
R. subclavian artery	$-2.15 + 0.43t$	$-1.22 + 0.12t$	$2.83f(t)$
L. Common Carotid artery	$-9.69 + 1.59t$	$-1.52 + 0.14t$	$2.83f(t)$
R. Common Carotid artery	$-8.25 + 1.36t$	$-1.52 + 0.14t$	$2.83f(t)$
L. Internal Carotid artery	$-8.25 + 1.36t$	$-1.22 + 0.11t$	$4.61f(t)$
R. Internal Carotid artery	$-8.25 + 1.36t$	$-1.22 + 0.11t$	$4.61f(t)$
L. Common Iliac artery	$-3.11 + 0.55t$	$1.28 - 0.09t + 0.004t^2$	$6.39f(t)$
R. Common Iliac artery	$-3.59 + 0.59t$	$1.39 - 0.11t + 0.004t^2$	$6.39f(t)$
L. Umbilical artery	$60t/40$	$0.0082 + 0.0094t$	$12.67f(t)$
R. Umbilical artery	$60t/40$	$0.0082 + 0.0094t$	$12.67f(t)$

$f(t) = 3.8 \cdot 10^2 t^2 + 4.7 \cdot 10^3 t + 1.5 \cdot 10^4$; t represents the gestational age in weeks; $1 \text{ dyn} = 1 \text{ g} \cdot \text{cm} \cdot \text{s}^{-2}$; R, L denotes right and left respectively.

Table 4.8: Exponents "b" of the allometric equations for scaling vascular bed resistances and compliances.

Scaling factors b	Vascular bed resistances R_p	Vascular bed compliances C_p
Brain	-1.10	1.47
Upper body	-1.00	1.33
Lungs	-1.20	1.60
Lower body	-1.00	1.33
Kidneys	-1.00	1.33
Placenta	-1.00	1.33

4.B Appendix B

The input of the model was defined as the set of the initial values of all the electrical components, calculated for each fetus as described in the Appendix A (4.A), and the two patient-specific blood flow inputs: Q_{RV} and Q_{LV} . The output was defined as the model-based blood velocities in the AoI (\tilde{V}_{AoI}), MCA (\tilde{V}_{MCA}) and UA (\tilde{V}_{UA}). In order to fit the model-based blood velocities to the measured ones, some of the model parameter needed to be

estimated, and therefore, an optimization algorithm was defined.

Since the number of total parameters in the model is to large, in order to obtain an efficient solution of the patient-specific modeling, a reduction in the number of model parameters to be estimated was necessary and, therefore, a subset of only few parameters was defined. The selection criteria were: (1) those parameters that are relevant in the adaptation mechanisms of IUGR fetuses and (2) those parameters that when varied, the output of the model varied significantly also. The factors (K_i) indicating the variation of the model parameters with respect to their nominal values were estimated ($K_i = I/I_0$). Therefore, a set of 13 factors (K) were defined: $K = K_{RcorA}$, K_{rAo} , K_{CAo} , K_{rbA} , K_{CbA} , K_{Rb} , K_{Cb} , K_{Rrest} , K_{Crest} , K_{ruA} , K_{CuA} , K_{Rplac} , K_{Cplac} ($RcorA$: coronary artery resistance, rAo : radius of the whole aorta (aortic arch + ascending, thoracic and abdominal aorta), CAo : compliance of the aorta, rbA : radius of the brain arteries, CbA : compliance of the brain arteries, Rb : brain's resistance, Cb : brain's compliance, $Rrest$: the resistance of the rest of vascular beds (lungs, upper body, kidneys and lower body), $Crest$: compliance of the rest of vascular beds (lungs, upper body, kidneys and lower body), ruA : radius of the umbilical artery, CuA : compliance of the umbilical artery, $Rplac$: placenta's resistance and $Cplac$: placenta's compliance).

To estimate the variation factors of the model parameters we used a constrained nonlinear optimization algorithm minimizing the normalized relative root mean square error (NRMSE) between the model-based (denoted by \sim) and measured velocity waveforms. To ensure that the model estimates correctly both systolic and diastolic extreme values of the blood velocities waveforms, we also included in the minimization objective function the relative error between model-based and measured values of each of these. Therefore, the objective function J was defined as the sum of individual relative errors as:

$$J = \sum_{i=AoI, MCA, UA} \left[\frac{\sqrt{\frac{1}{N} \sum_{t=1}^N (\tilde{V}_i(t) - V_i(t))^2}}{\max(V_i(t)) - \min(V_i(t))} + \left| \frac{\tilde{V}_i(t_{sys}) - V_i(t_{sys})}{V_i(t_{sys})} \right| + \left| \frac{\tilde{V}_i(t_{dias}) - V_i(t_{dias})}{V_i(t_{dias})} \right| \right] \quad (4.1)$$

where i indicates one of the three places of the fetal circulation where blood velocity were measured: AoI, MCA or UA; N is the number of time points and t_{sys} and t_{dias} are the systolic and diastolic time points respectively. To do this, the model was initialized with the nominal model parameters that describe a normal fetus with same GA and EFW , and with an initial set of K_i

4.B. Appendix B

factors. Then, the estimation problem consisted on searching the parameter set that minimizes J . The initial set of K_i factors ($K = \{K_i\}$) were randomly defined within a physiological range. Then, to avoid local minim solutions, the optimization procedure was repeated several times with different initial factors sets K , and we finally chose the factors set K with the minimum J value.



CHAPTER **5**

Automated cardiac sarcomere analysis
from second harmonic generation
images

Abstract — Automatic quantification of cardiac muscle properties in tissue sections might provide important information related to different types of diseases. Second harmonic generation (SHG) imaging provides a stain-free microscopy approach to image cardiac fibers that, combined with our methodology of the automated measurement of the ultrastructure of muscle fibers, computes a reliable set of quantitative image features (sarcomere length, A-band length, thick-thin interaction length, and fiber orientation). We evaluated the performance of our methodology in computer-generated muscle fibers modeling some artifacts that are present during the image acquisition. Then, we also evaluated it by comparing it to manual measurements in SHG images from cardiac tissue of fetal and adult rabbits. The results showed a good performance of our methodology at high signal-to-noise ratio of 20 dB. We conclude that our automated measurements enable reliable characterization of cardiac fiber tissues to systematically study cardiac tissue in a wide range of conditions.

Adapted from: Garcia-Canadilla P, Gonzalez-Tendero A, Iruretagoyena I, Crispi F, Torre I, Amat-Roldan I, Bijnens BH, Gratacos E. *Automated cardiac sarcomere analysis from second harmonic generation images*. J Biomed Opt.19(5):056010, 2014

5.1 Introduction

Sarcomeres are the elementary contractile units in cardiac and skeletal muscles and are composed of three basic structural elements as shown in Figure 5.1. Two transverse structures: the Z-discs, anchoring the (actin) thin filaments and the M-band that crosslinks the (myosin) thick filaments in the center. The elastic titin filaments connect both structures in the longitudinal plane. Interaction of sarcomere thin and thick filaments generates the force necessary for contractile function. The expression of sarcomeric proteins is well documented to respond to physiological activity or disease, making the sarcomere a prime candidate for a visible indicator of myofiber integrity [125–127]. The study of sarcomere morphometry provides information about the sarcomere's structure and function and thus about cardiac contractility [128]. For this, end-diastolic sarcomere length (SL) has been widely used as a feature of sarcomere morphometry [129, 130]; however, reliable and automated techniques for measuring these sarcomeric features in living intact tissue are limited.

Second harmonic generation (SHG) microscopy has shown an enormous potential for providing information with high resolution and contrast of certain unstained structures such as collagen, myosin, microtubulin, starch, and cellulose, which are of interest for many biomedical applications [131–137]. This unique contrast mechanism combined with recent technological advances in multiphoton microendoscopes/fibers [138–140] and ultrashort pulse laser sources [141], suggests that SHG might find clinical applications as an optical biopsy tool [133]. In this line, SHG has been studied in many applications related with collagen, [134, 142, 143] as it is a highly efficient frequency doubling biomaterial that can be detected by standard multiphoton microscopes. Myosin, a molecule present in all types of muscle, shows a smaller harmonic signal [133, 134, 144] and has been studied less.

The SHG signal along a muscle fiber presents a biperiodical pattern [129, 137] as shown in Figure 5.1(d)-(e) and the two periods are associated with characteristic sarcomeric lengths that provide information of the ultrastructure of the cardiac tissue [129, 145, 146]. Particularly, the shortest period corresponds to the A-band length (ABL) and the longest period to SL (distance between Z-discs). Recently, the Fourier transform (FT) has been used to compute the periodicity and the preferred orientation from SHG in biological tissues [142, 143] and it was demonstrated how image-processing techniques can extract quantitative information from this imaging modality. However, the generalization of this approach is limited and there is a need to develop more automated and accurate methodologies. Recent papers have shown that pattern analysis of striated muscle correlates with physiological

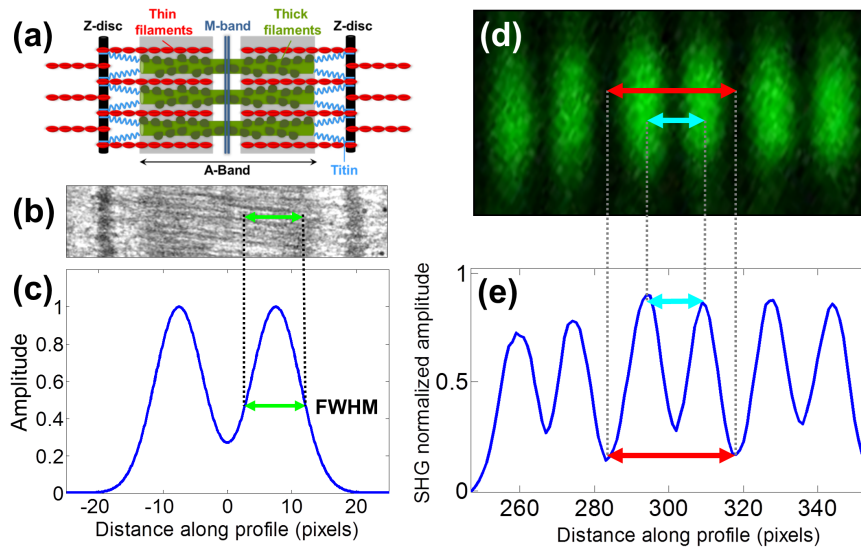


Figure 5.1: (a) Schematic representation of the elementary parts of the sarcomere, (b) Transmission electron microscopy image from a sarcomere acquired from a young adult rabbit heart using a JEM-1010 electron microscope (Jeol, Japan) equipped with a CCD camera Megaview III and the ANALYSIS software (Soft Imaging System GmbH, 1998), at 60000x magnification, (c) ideal SHG signal intensity profile along a sarcomere, (d) SHG image of a muscle fiber and (e) SHG intensity profile along the muscle fiber. Sarcomere Length (SL) is indicated by a red arrow, intrasarcomeric A-band length (ABL) by a blue arrow and Thick-thin interaction length (TTIL) by a green arrow, calculated as the full width at half maximum (FWHM) of the Gaussian and defined as $2\sqrt{2\ln 2}\sigma$, where σ is the width of the Gaussian.

function, and this might be useful for developing tools that assist diagnosis and possibly to monitor chronic diseases [24, 147, 148]. However, the pioneering work of Plotnikov et al. was related to abstract image features providing no supportive information to clinicians and biomedical researchers. More recently, these image features have evolved towards describing more comprehensive concepts of biology that allow a multidisciplinary exchange of ideas among experts. Our prior research reported that automated quantification of the average fiber orientation (FO), SL and ABL in cardiac tissue was more reliably computed by means of a method based on the analysis of the autocorrelation rather than a Fourier approach [24]. Another recent paper, focused on skeletal muscle tissue, developed a technique to quantify local disruption of the regular sarcomere lattice (verniers) that was associated with diseased muscle [147]. These papers show that SHG is indeed a promising stain-free image modality for assessing muscle and cardiac tis-

5.2. Methods

sue as it is highly specific for myosin thick filaments and targets one of the major actors of the contractile machinery. Under some circumstances, SHG from collagen can be also found (i.e. in fibrotic or adult hearts) but this can be filtered out by different means, like post processing in combination with optical methods [134, 149] by taking advantage of the differences from the SHG signal generated by these two structures. Apart from that, there are no other major interference effects when detecting SHG signal from myosin in most of tissues.

This paper extends the prior study of our model to understand the use and limitations of the proposed algorithm and set some of the imaging conditions required to achieve a given level of accuracy. Our goal is to evaluate the robustness of our algorithm for measuring morphometric features of cardiac tissue in SHG images. For this, we first performed numerical simulations to evaluate the performance of our methodology in one and two dimensional computer generated muscle fibers, by adding different artifacts that can influence the measurements such as noise, depth of modulation and fiber bending and twisting. Secondly, automatic measurements of sarcomere ultrastructure and fiber orientation of cardiac tissue samples were compared with manual measurements. Finally, we applied our algorithm to analyze the morphometric features of cardiac tissue in a set of SHG images from fetal and adult rabbit hearts, acquired at different signal-to-noise ratio (SNR) to evaluate the practical applications of our study in the biomedical research.

5.2 Methods

5.2.1 Image processing

The proposed image processing algorithm is explained elsewhere in detail [24]. In summary it consists of: (1) estimation of local fiber orientation, (2) tracking of muscle fibers, (3) muscle fiber profiling, (4) correlation of muscle fibers SHG signal and (5) model fitting and parameter extraction. Briefly, local fiber orientation is estimated by computing the local autocorrelation of small blocks of pixels, followed by direct binarization of the autocorrelation and principal component analysis. The major axis orientation of the muscle fiber is computed as the first principal component. Once the local fiber angle is estimated, the muscle fiber tracking is performed. After obtaining the intensity profile for every tracked muscle fiber, the autocorrelation is calculated and fitted with a parametric model. After the model fitting, the mean of the ultrastructure sarcomere measurements within a muscle fiber is obtained for each fiber in the image. Therefore, distributions of FO, SL, ABL and Thick-thin Interaction Length (TTIL) for a SHG image of cardiac

tissue were the quantitative descriptors obtained as output parameters of our algorithm. Finally, the mean \pm standard deviation (SD) of the four features were calculated from the distributions, rejecting all the values outside the range $\pm 2.7SD$, since they were considered as outliers.

5.2.2 Simulation of computer generated muscle fibers

SHG intensity signal from a sarcomere can be modeled by two gaussian functions [24, 129] In this manner, the whole cardiac muscle fiber $f(z)$ can be defined as (Figure 5.2(a)):

$$f(z) = \sum_{n=1}^M \alpha_+^k \exp \left[- \left(\frac{z - T_1/2 - nT_2}{\sqrt{2}\sigma_k} \right)^2 \right] + \alpha_-^k \exp \left[- \left(\frac{z + T_1/2 - nT_2}{\sqrt{2}\sigma_k} \right)^2 \right] \quad (5.1)$$

where T_1 corresponds to the ABL, T_2 to the SL and σ_k to the TTIL. $\alpha_{+,-}^k$ accounts for the illumination variation when imaging the k -th sarcomere (see Figure 5.1(c)). M denotes the number of sarcomeres in the muscle fiber.

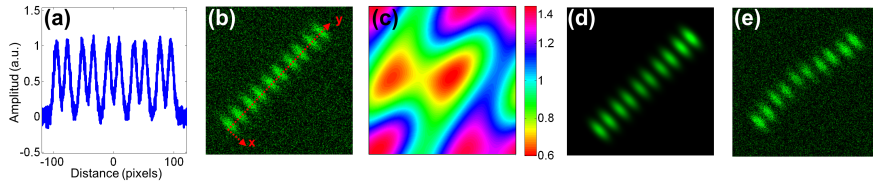


Figure 5.2: (a) 1D straight muscle fiber at signal-to-noise ratio (SNR) of 20 dB, (b) 2D straight noisy fiber at SNR of 10 dB, with the y -axis and x -axis aligned to the long and short axis of the fiber, (c) modulating image $(1 + (I_{mod} - 0.5)mx)$ with a depth of modulation (DOM) of 80% ($mx = 0.8$), (d) modulated image (I_M) with DOM of 80% of a 2D straight fiber and (e) 2D wavy noisy fiber at SNR of 10 dB with a DOM of 80%.

Artificial cardiac muscle fibers were numerically generated according to Equation 5.1 varying the different ultrastructural morphometric features: (1) TTIL, (2) ABL and (3) SL, in one dimension (1D). However, this calculation skips many steps of our methodology that adds error. For this, we included the two dimensional (2D) generation of muscle fibers, as shown in Figure 5.2(b). Similarly to 1D, the two dimensional SHG signal from a sarcomere can be modeled by two 2D gaussians. Therefore, the whole 2D muscle fiber $f(x,y)$ can be defined as:

5.2. Methods

$$f(x,y) = \sum_{n=1}^M \alpha_+^k \exp \left[- \left(\frac{y - T_1/2 - nT_2}{\sqrt{2}\sigma_{k,y}} \right)^2 - \left(\frac{x}{\sqrt{2}\sigma_{k,x}} \right)^2 \right] + \alpha_-^k \exp \left[- \left(\frac{y + T_1/2 - nT_2}{\sqrt{2}\sigma_{k,y}} \right)^2 - \left(\frac{x}{\sqrt{2}\sigma_{k,x}} \right)^2 \right] \quad (5.2)$$

where the y-axis and x-axis are aligned to the long and short axis of the muscle fiber respectively (see Figure 5.2(b)). $\sigma_{k,y}$ corresponds to the TTIL and $\sigma_{k,x}$ to the thickness of the muscle fiber assumed to be $2.5\sigma_{k,y}$, according to the estimated fiber thickness measured manually in a SHG image from cardiac tissue (Figure 5.5(a)).

Also we considered the addition of White Gaussian Noise (WGN) in both 1D and 2D computer generated muscle fibers, as shown in Figure 5.2(a)-(b). Besides noise, many illumination changes occur during acquisition as a consequence of many factors like non-uniform illumination and tissue bending in and out of the focal plane. This has been modeled as a slowly varying image that modulates the image, as shown in Figure 5.2(c)-(d). The proposed methodology is finally challenged by simulating the natural fiber bending within the 2D plane (or fiber twisting) as shown in Figure 5.2(e). Therefore, the artifacts that were modeled are: (1) addition of WGN of zero mean and variance σ_N^2 in 1D and 2D muscle fibers, (2) amplitude modulation of the SHG signal: illumination artifacts and 3D fiber bending for 2D data, and (3) fiber twisting: in-plane fiber bending for 2D data. The WGN power was varied to obtain an estimated SNR ranging from 0dB to 50dB. Amplitude modulation was simulated by generating a modulating image (I_{mod}) composed of two different cosines of unitary frequency (f_x and $f_y = 1$) and two cosines of frequencies $2f_x - f_y$ and $2f_y - f_x$, with random amplitude and phase. With this combination of cosines a random slow intensity variation modulating image, with a longitudinal component in the same direction as the muscle fibers was generated. An example of a modulating image is displayed in Figure 5.2(c). Modulated image (I_M) was obtained as $I_M = I \cdot [1 + (I_{mod} - 0.5) \cdot m_x]$ where m_x denotes the depth of modulation factor and varies from 0 to 1. Fiber twisting was modeled by varying the local orientation of each sarcomere within the muscle fiber randomly, but limiting this angular change to a maximum of 15° . The maximum angular change within a fiber was chosen after estimating the maximum local angle variation in SHG images from cardiac tissue (see Figure 5.5(a)-(b)). Muscle fibers of five sarcomeres were considered in all the simulations.

The different simulated scenarios were: (1) 1D and WGN with SNR from 0 to 50 dB; (2) 2D and WGN with SNR from 0 to 50 dB; (3) 2D,

WGN with SNR from 0 to 50 dB, and depth of modulation with $m_x = 0.2, 0.4, 0.6$ and 0.8 ; (4) 2D, WGN with SNR from 0 to 50 dB, fiber twisting and depth of modulation with $m_x = 0.2, 0.4, 0.6$ and 0.8 . One hundred computer generated muscle fibers with different morphometric dimensions (T_1, T_2 and σ) were generated for each simulated scenario. The performance of the method was evaluated by computing the success rate, calculated as the ratio between the number of computer generated fibers measured successfully and the total number of computer generated muscle fibers, and the relationship between the experimentally estimated SNR of the signal and the ground truth using the root mean square error (RMSE) of the T_1, T_2 and values from the model of muscle fiber based on Equation 5.1. The SNR was estimated as $SNR = E\{I_W^2\}/E\{(I_N - I_W)^2\}$ where I_W corresponds to the wiener filtered image, with a window's size of 5 pixels, and I_N corresponds to the noisy image ($I_N = I + WGN$).

5.2.3 Analysis of biological samples

Fetal and adult hearts from New Zealand White rabbits were analyzed to illustrate the practical implications of our study in biomedical research. Animals were provided by a certified breeder. Animal handling and all procedures were performed in accordance to applicable regulations and guidelines, and with the approval of the Animal Experimental Ethics Committee of the University of Barcelona. Hearts from these animals were obtained one day prior birth (fetal) and 70 postnatal days (adult) following previously reported protocols [21, 23]. Briefly, hearts were fixed by immersion in 4% paraformaldehyde in phosphate buffered saline (PBS), for 24 hours at 4°C. The tissue was then dehydrated and embedded in paraffin, and 30 μm thick transversal heart sections were cut in a microtome. Finally, sections were mounted onto silane (Sigma-Aldrich) coated thin slides. Tissue sections were deparaffinized with xylene and decreasing concentrations of ethanol (100° / 96° / 70°), and finally covered with Mowiol 4-88 mounting medium (Sigma-Aldrich).

A Leica TCS-SP5 laser scanning spectral confocal multiphoton microscope (Leica Microsystems Heidelberg GmbH, Mannheim, Germany) equipped with a Near Infrared laser (Mai Tai Broad Band 710-990 nm, 120 femtosecond pulse) and DMI6000 inverted microscope, from the Advanced Optical Microscopy Unit from Scientific and Technological Centres from University of Barcelona was used to acquire SHG images from unlabeled heart tissues. A 25x water immersion objective (HCX IR APO L), with a numerical aperture (NA) of 0.95 and an oil immersion condenser (NA 1.40 OilS1), both from Leica Microsystems were used to acquire SHG images. The images were sampled at a pixel size of 40 nm. Samples were identified

5.3. Results

to contain mostly cardiomyocytes and no collagen. Cardiac longitudinal fibers were oriented at 45 degrees to maximize SNR of SHG from muscle fibers. The image size was 2048 x 2048 pixels.

Firstly, manual measurements of sarcomere morphometry and local muscle fiber orientations were performed in 30 different regions within an SHG image of cardiac tissue acquired at high SNR. Moreover, the automatic measurement of the muscle fiber morphometry was performed in the same image and both manual and automatic measurements were compared by calculating the mean \pm SD. Finally, we evaluated the automatic measurement of muscle fiber morphometric features (SL, ABL, TTIL and FO) in cardiac tissue, in two sets of 10 images each one, acquired at two different SNR, by calculating for each image the mean \pm SD of each of the four features.

5.3 Results

5.3.1 Rubustness analysis with numerical simulations

The computed success rate in retrieving measurements from computer generated 1D muscle fibers obtained is above 90% at 15dB and RMSE of SL, ABL and TTIL is below 1 pixel for all three measurements at SNR of 7dB (see Figure 5.3(a)-(b)). In the case of computer generated 2D muscle fibers, the computed success rate is above 90% also at 15dB. Additionally, the computed RMSE of SL, ABL and TTIL is below 1 pixel for all three measurements at a SNR of 15dB (see Figure 5.3(c)-(d)).

Results with a depth of modulation of 40% show already an effect at SNR below 15dBs and in this context the RMSE is almost doubled (see Figure 5.3(e)-(f)). However, at a SNR of 15dBs the RMSE is still below 1 pixel. Higher depth of modulation shows increased errors but beyond 17dB the RMSE is always maintained below 1 pixel and success rate is above 90%.

The results of the natural fiber bending within the 2D plane simulation in combination with all the prior artifacts, shows that, with a depth of modulation of 40%, a SNR of 20dB should produce an error below one pixel (see Figure 5.3(g)-(h)).

Finally, in order to illustrate the effect of WGN together with the other artifacts on the average and variability of the measurements, real SL were plotted against the corresponding estimated value in Figure 5.4, at three different SNR: 12dB, 17 dB and 20 dB, and for each of the four simulated scenarios: 1D, 2D, 2D with a depth of modulation of 40% and 2D with twisted fibers and a depth of modulation of 40%.

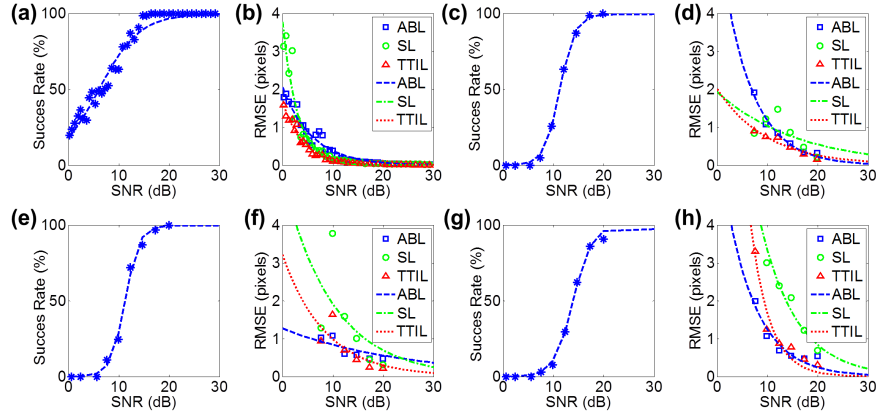


Figure 5.3: (a) Success rate and (b) root-mean square error (RMSE) of Thick-tin interaction length (TTIL), A-band length (ABL) and Sarcomere length (SL) at different SNR for 1D straight muscle fiber; (c) Success rate and (d) RMSE of TTIL, ABL and SL at different SNR for 2D straight muscle fiber; (e) Success rate and (f) RMSE of TTIL, ABL and SL at different SNR for 2D straight muscle fibers with a depth of modulation (DOM) of 40% and (g) success rate and (h) RMSE of TTIL, ABL and SL at different SNR for 2D twisted muscle fibers with a DOM of 40%.

5.3.2 Manual vs. automatic quantification of muscle fibers

Automatic measurement of sarcomere ultrastructure shows excellent agreement with 30 manual delineations in different regions of the image shown in Figure 5.5(a) and it offers a similar uncertainty, as shown in Table 5.1. The absolute difference between manual and automated measurements was less than one pixel for two of the morphometric features (ABL, SL). TTIL was not measurable manually. Measurement of local fiber orientation also shows excellent agreement with the manual delineations of different image regions as shown in Table 5.1. An example of the local fiber orientation estimation is shown in Figure 5.5(c)-(d), which also illustrates the good performance of the algorithm computing the local fiber angle. Finally, the distributions of FO, SL, ABL and TTIL for the same SHG cardiac tissue sample shown in Figure 5.5(a) are plotted in Figure 5.6 to illustrate the output of our algorithm.

5.3.3 Quantification of sarcomeres at different SNRs and status

We show in this section the results comparing images from an animal model at two different SNR. SNR was estimated after the image acquisition. The estimated SNR of the first set of images corresponding to young adult rabbit

5.3. Results

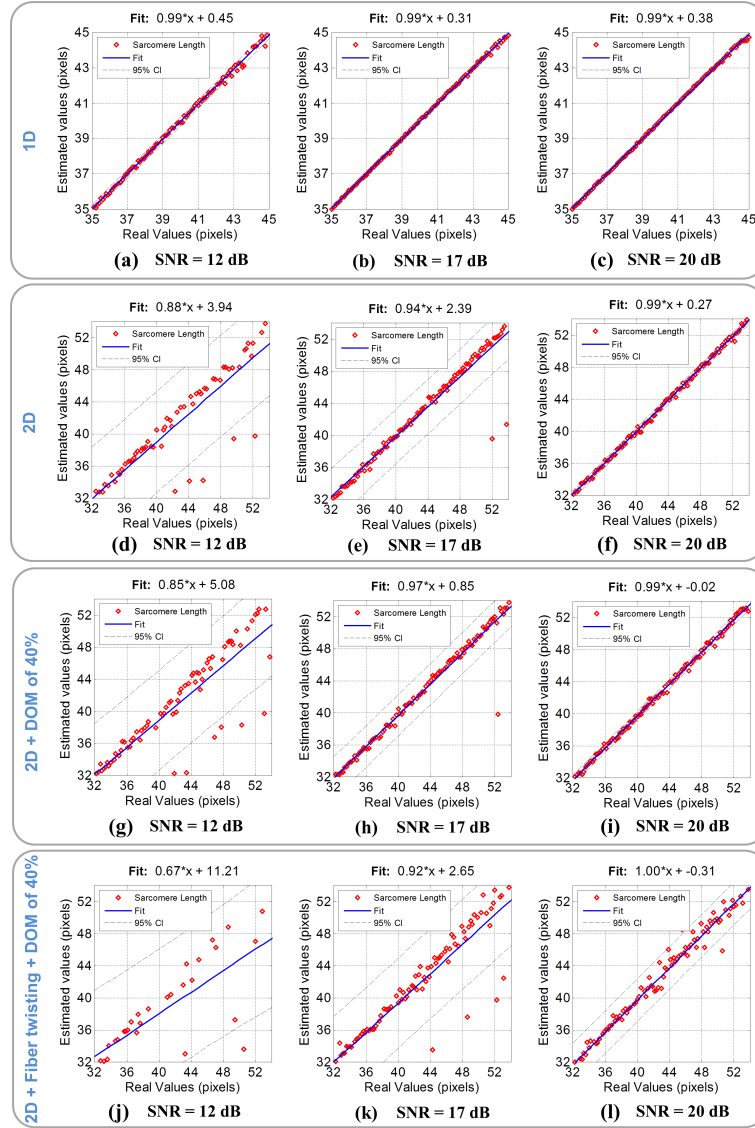


Figure 5.4: Real values of the sarcomere length (SL) of the simulated computer generated muscle fibers plotted against the corresponding estimated values, for four different simulated scenarios and at three different SNR; (a)-(c): 1D at (a) SNR = 12 dB, (b) 17 dB and (c) 20 dB; (d)-(f): 2D at (d) SNR = 12 dB, (e) 17 dB and (f) 20 dB; (g)-(i) 2D + depth of modulation (DOM) of 40% at (g) SNR = 12 dB, (h) 17 dB and (i) 20 dB; and (j)-(l): 2D + fiber twisting + DOM of 40% at (j) SNR = 12 dB, (k) 17 dB and (l) 20 dB. CI denotes Confidence Interval. The blue line corresponds to the linear fitting with the function $y = a \cdot x + b$.

Table 5.1: Comparison of muscle fibers morphometric measurements (mean \pm standard deviation) calculated with our algorithm against manual measurements in 30 different regions within the same image.

Morphometric feature	Manual	Automated
A-Band length (T_1) (pixels)	20.57 ± 2.97	21.39 ± 1.63
Sarcomere length (T_2) (pixels)	45.51 ± 2.67	44.60 ± 2.66
Thick-thin interaction length (σ) (pixels)	*	2.66 ± 0.37
Fiber orientation (degrees)	38.97 ± 9.22	36.46 ± 5.57

*Thick-thin interaction length was not measurable manually.

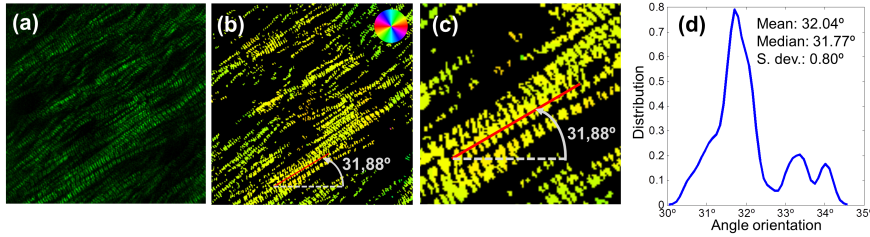


Figure 5.5: (a) Original standard SHG image acquired with a resolution of 40 nm/pixel and a SNR of 25.66 dB; (b) local fiber orientation estimation. Color wheel represents angles between 0° and 180° . (c) Zoom in of post processed image (b). Manual delineation of local fiber angle is plot in a red line. (d) Distribution of angles within the delineated red line.

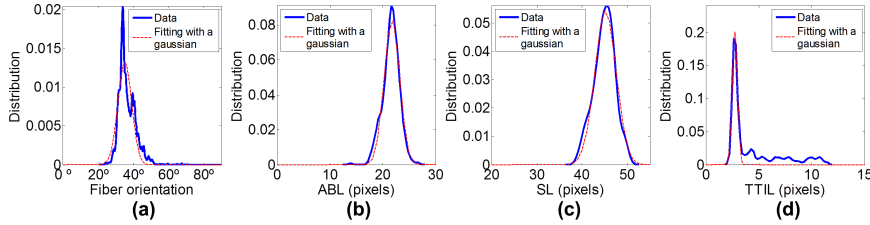


Figure 5.6: Output of the algorithm: (a) Fiber Orientation, (b) A-Band Length (ABL), (c) Sarcomere Length (SL) and (d) Thick-Thin Interaction Length (TTIL) distributions in a SHG image. The dashed red line indicates the fitting with a gaussian function.

cardiac tissue was 23.21 ± 0.95 dB. The estimated SNR of the second set of images corresponding to fetal rabbit cardiac tissue was 16.72 ± 0.21 dB. The mean and SD of the four morphometric features measured automatically are shown in Table 5.2. The estimated depth of modulation for the set of images from fetal rabbit hearts was 0.88, and 0.59 for the set of images from young adult rabbit hearts. Two representative images from both sets of SHG images are displayed in Figure 5.7. It can be appreciated that the

5.4. Discussion

fetal cardiac muscle fibers are more twisted compared to the young adult ones. Also it can be observed the higher depth of modulation in the image corresponding to fetal cardiac tissue. The higher influence of both artifacts and also the lower SNR in the set of fetal cardiac tissue images account for the higher variability obtained in the measurements of the muscle fibers morphometry.

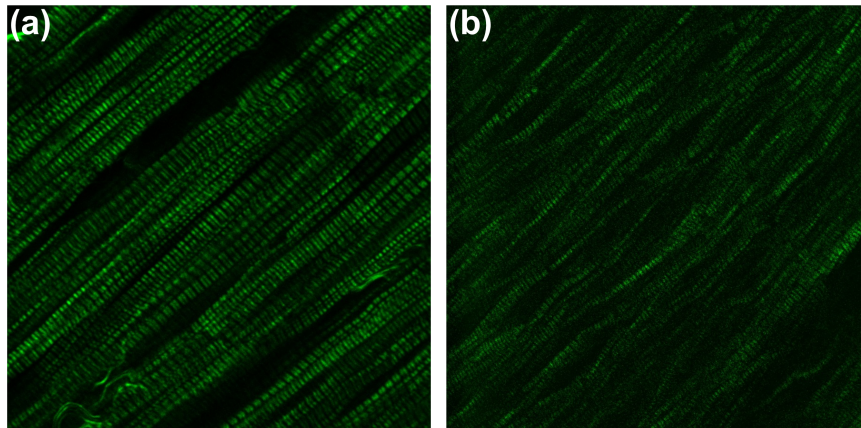


Figure 5.7: Examples of SHG images from (a) young adult rabbit cardiac tissue with a SNR of 23 dB and (b) fetal rabbit cardiac tissue with a SNR of 17 dB.

Table 5.2: Results of the automatic measurement of muscle fibers morphometry in two sets of 10 images each one, acquired at different SNR. For each image the mean \pm standard deviation (SD) of the four morphometric features and of the SNR was computed, and it is reported here the average of the mean and of the SD for all the images

SNR dB	A-band length (pixels)		Sarcomere length (pixels)		Thick-thin interaction length (pixels)		Fiber angle ($^{\circ}$)	
	mean	SD	mean	SD	mean	SD	mean	SD
23.21 \pm 0.95	22.53	1.26	46.34	1.40	4.66	0.40	49.22	3.64
16.72 \pm 1.66	16.20	3.29	34.38	5.82	3.53	0.99	49.19	5.26

5.4 Discussion

In the present paper we have shown the good performance of our methodology to assess morphometric features of cardiac fibers in SHG images of cardiac tissue.

Many times, sample preparation, storage, microscope alignment, maintenance and other issues related to image acquisition limit the quality of the tissue and the delivered images for the analysis. For this reason, we analyzed the performance of our method by including numerical simulations in 1D and 2D computer generated muscle fibers. We modeled different artifacts that are present during the image acquisition process, including noise, depth of modulation, fiber bending or twisting. The best performance of the system is found at 20 dB as it obtains a high success rate (above 90%) and high accuracy (RMSE below one pixel of 40 nm).

The manual validation performed on a subset of images enables us to ensure the good performance of our method at high SNR values (above 20dB). In this context, we propose our methodology to extract quantitative image features from SHG microscopy to characterize cardiac tissue in the form of distributions of FO, SL, ABL and TTIL as shown in Figure 5.6. These features are highly reproducible because they are related to ultrastructural morphology of the tissue and are not purely based on local signal ratios. The average value of FO is certainly arbitrary, but its distribution or standard deviation is related to fiber disruption, and this is related to muscle atrophy [147]. End-diastolic SL is widely used as a feature of sarcomere morphometry [129, 130]; however, reliable and automated techniques for measuring these sarcomeric distances in living intact tissue are limited. Similarly, ABL and TTIL should also provide valuable information about the cardiac status, but they are sub-micron structures, which are highly difficult and tedious measurements to be performed manually and thus there are no studies using them. Systematic analysis with our methodology provides an objective manner to quantify numerous unstained histological sections of cardiac tissue (or muscle tissue) that is not available by other means. The representation of the cardiac tissue in the form of four distributions offers a way to compare many samples and look for statistical differences within large datasets. Furthermore, statistical means can be used to reject spurious results that might occur at the tails of the distributions.

The condition of a minimum SNR of 20 dB is very strict and is recommended when studying small groups of subjects to obtain reliable conclusions. Automated analysis of real images of animals at different SNR provided evidence that for a particular experiment, with similar conditions, concerns on the SNR can be reduced, as the averaging among many samples will converge to the right measurement. Also, the variability obtained in the automated analysis of both set of real images is consisted with the expected variability obtained in the numerical simulations of computer generated fibers. For example, according to the simulation results, the 95% confidence interval (CI) for the SL measurement in twisted fibers, with a depth of modulation of 60% and with a SNR of 20 dB is ± 3.68 pixels (data

5.5. Conclusions

not shown), and the SD for the SL measurements in real SHG images from young adult cardiac tissue was ± 1.40 pixels. On the other hand, the 95% CI for the SL measurement in twisted fibers, with a depth of modulation of 80% and with a SNR of 17 dB is ± 5.68 pixels (data not shown), and the SD for the SL measurements in real images from fetal rabbit cardiac tissue was ± 5.82 pixels, which means a 95% CI of ± 3.61 pixels. These results reflect the good performance of our algorithm in measuring the morphometry of cardiac muscle fibers in SHG images and also how the numerical simulations can help us to improve the design of our experiments and also the posterior analysis by addressing some type of correction like image exclusion, bias correction or image re-acquisition when possible. Developments in this direction aim to bring together recent advances in biophotonics to clinical applications as this enables to reproduce experiments objectively, many times and in different locations, as well as, set the new advances to develop robust image processing tools that extract relevant information for biomedical researchers and clinically driven applications. Additionally, our methodology was used to evaluate sarcomere ultrastructural differences in a control-case study of human fetuses, and reporting shorter cardiac sarcomere length in fetuses with intrauterine growth restriction [21].

5.5 Conclusions

To conclude, our approach based on automated autocorrelation analysis shows similar results to manual delineations and is a robust technique provided a sufficient SNR in the images. We have evaluated the impact of noise, amplitude modulation and fiber twisting and minimal errors are found for images beyond 20dB, which is a realistic amount for automated histology analysis. We further supported our numerical results of computer generated data with real experiments based on two different acquisition conditions. Finally, the results showed that our technique for measuring the sarcomere distances is accurate and allows to reproduce changes previously described, concerning changes in the SL under pathological conditions [26–28]. Our methodology was successfully applied to measure sarcomere distances in a fetal human control-case study [21] and also in an animal model of intrauterine growth restriction (IUGR) [22], reporting shorter cardiac sarcomere length in rabbits and human fetuses with IUGR.



CHAPTER **6**

A two dimensional electromechanical
model of a cardiomyocyte to assess
intra-cellular regional mechanical
heterogeneities

Abstract — Experimental studies on living cardiomyocytes, the contractile cardiac cells, from different animal species and human hearts have demonstrated that there are regional differences in the structure and function of cardiomyocytes. Specifically, heterogeneities in the Ca^{2+} release, Ca^{2+} decay and local sarcomere contraction have been described. Local deformation heterogeneities can be due to a combination of factors: (1) differences in Ca^{2+} release and/or re-uptake, (2) intra-cellular differences in elasticity, (3) differences in the resting sarcomere length or (4) different distribution of the intracellular organelles. In order to investigate the possible causes of these mechanical heterogeneities, a finite-element model of a cardiac cell was constructed. Most published cardiac cells models considered an isotropic electro/mechanical behavior of the cardiomyocyte. In this paper we present a two-dimensional finite-element electromechanical model of a cardiomyocyte that takes into account the heterogeneities in the mechanical properties of the cell. A multi-parametric analysis was performed to analyze the specific influence of the different mechanical properties that could explain the local differences in the amount and duration of cell contraction. Local cytosolic Ca^{2+} transients and local deformation along the longitudinal direction of the cell were measured by confocal line-scan microscopy, in three electrically stimulated rat cardiac cells. The experimentally measured local Ca^{2+} transients were used to define the local Ca^{2+} -dependent activation functions of the electro-mechanical coupling that induces the cell contraction in the model. The cell-specific local Young's moduli were estimated by solving an inverse problem minimizing the error between the experimentally measured and simulated local deformation by the finite-element model.

We found that local heterogeneities in the deformation during contraction were determined mainly by the local elasticity and the amount of force generated by the sarcomeres rather than the amount of Ca^{2+} . On the other hand, time of local sarcomere re-lengthening was mainly determined by the time for Ca^{2+} re-uptake, as was previously reported from experimental work. Our simplified electromechanical model was able to successfully estimate local elasticity along the longitudinal direction in three different cardiac cells.

In conclusion, our proposed electromechanical model of a cardiomyocyte seems to be a good approximation to assess the heterogenous intracellular mechanical properties.

Adapted from: Garcia-Canadilla P, Rodriguez JF, Palazzi MJ, Schonleitner P, Balicevic V, Loncaric S, Antoons G, Cripi F, Gratacos E, Bijnens B. *A two dimensional electromechanical model of a cardiomyocyte to assess intra-cellular regional mechanical heterogeneities*. In preparation, 2015

6.1 Introduction

Cardiomyocytes are the contractile cells that constitute the myocardial wall. They consist of myofibrils that, in turn, consist of long chains of sarcomeres, the fundamental cardiac contractile units. They can contain one or more nuclei and have a high mitochondrial density. The contraction-relaxation process within a cardiomyocyte is mediated principally by Ca^{2+} . The release of Ca^{2+} after the electrical activation induces the contraction of the cardiomyocyte (excitation-contraction coupling). The Ca^{2+} influx through sarcolemmal voltage-dependent channels triggers the Ca^{2+} release from the sarcoplasmic reticulum (SR) (Ca^{2+} induced- Ca^{2+} release). This increase in cytosolic Ca^{2+} activates the myofilaments that induces cell shortening. To allow cell relaxation Ca^{2+} is extruded from the cytosol, mainly by the Ca^{2+} pump (SERCA) into the SR, and by the Na^+/Ca^{2+} exchanger (NCX) to the extracellular space. In cardiomyocytes, coordinated Ca^{2+} release from the SR determines cellular contraction. Ca^{2+} -induced Ca^{2+} release is regulated locally in subcellular microdomains. There are studies that provided quantitative evidence for regional differences in the subcellular regulation of $[Ca^{2+}]$ release [150]. The areas of delayed Ca^{2+} release were related to regional absence of T-Tubules. Regional differences in $[Ca^{2+}]$ re-uptake during diastole were also reported [33]. In the same study, heterogeneities in the sarcomere relaxation/re-lengthening time were reported and, furthermore, the local sarcomere re-lengthening time correlated with the local $[Ca^{2+}]$ decay time, indicating that dyssynchrony of the decay of cytosolic $[Ca^{2+}]$ contributes to dyssynchronous intracellular sarcomere re-lengthening. All these findings demonstrate the existence of functional heterogeneities in healthy cardiac cells and also suggest that these heterogeneities can change under pathological conditions. Regional heterogeneities in the cell contraction/deformation can be due to several factors: (1) differences in Ca^{2+} release and/or re-uptake (timing and amount of Ca^{2+}), (2) intra-cellular differences in elasticity (3) differences in the local resting sarcomere length and/or (4) different spatial distribution of the intracellular organelles.

The spatial distribution of the mechanical properties of cardiac cells have been conventionally measured using atomic force microscopy (AFM), demonstrating the existence of regional differences in the elastic modulus [151–155]. However this technique is tedious, time-consuming and has high measurement variability. For example, the values of the measured Young's modulus in the same cell type reported in the different studies differ from each other [151]. For this reason, finite-element models based on constitutive laws have emerged as an alternative to assess the mechanical cell properties. Moreover, electromechanical models of cardiac cells can help in

the better understanding of the functional and structural differences between healthy and pathological cells.

Several two and three dimensional models of cardiomyocytes based on a continuum mechanical framework in which mechanical properties are described by strain energy functions, have been published during the last two decades [45–47], from the simplest to the most detailed ones, which included for example, the T-tubule network and some organelles such as mitochondria [45]. However, in all of these, an homogeneous distribution of these mechanical properties in the whole cell has been assumed, whereas experimental studies in living cardiomyocytes have demonstrated regional heterogeneities in the mechanical cell properties. Our proposed simplified two-dimensional electromechanical cell model overcomes this limitation by taking into account the experimentally measured local deformation and cytosolic Ca^{2+} concentration to locally define the different variables of the constitutive equations which describe the electro/mechanical behavior of the cell.

The aim of this work was to develop a finite-element electromechanical model of a cardiomyocyte considering the heterogeneities in the mechanical properties of the cell. The relationship between the cell contraction and the different mechanical properties that could explain the local differences in the amount and duration of cell contraction, such as elasticity, amount of active force generated by the sarcomeres and cytosolic Ca^{2+} , was assessed by a multiparametric analysis. Finally, local cytosolic Ca^{2+} transients and local deformation along the longitudinal direction of the cell were measured by confocal line-scan microscopy, in three electrically stimulated rat cardiac cells. This data was used to personalize the model and to estimate the local Young's modulus along the longitudinal axis of the cell by solving an inverse problem minimizing the error between the experimentally measured and cell-specific simulated local deformation.

6.2 Methods

6.2.1 Cardiomyocyte imaging and quantification

Cardiomyocytes were provided by the *Dept. of Cardiology, Medical University of Graz, Austria*. Freshly isolated cardiomyocytes were obtained from a rat left ventricle. The cells were loaded with Fluo-4 to simultaneously record confocal cytosolic $[Ca^{2+}]$ transients. The sarcolemma, including the T-tubules, was stained with Alexa Fluor 594 wheat germ agglutinine (10 $\mu\text{g}/\text{mL}$ for 40 minutes). Confocal line-scan images were obtained by repetitive scanning. A scan line was selected parallel to the longitudinal axis, extending across the full length of the cardiomyocyte in the focal plane and

6.2. Methods

orthogonal to the Z-lines. In line-scan images, the T-tubule signal appeared as a regular spaced pattern marking the Z-lines of the sarcomeres. Cardiomyocytes were stimulated in an electric field at a frequency of 1Hz until steady state. Sequential line-scans were stacked over time and are shown as 2D line-scan images. Line-scan images of 5 to 10 successive beats were recorded.

Quantification of local sarcomere and Ca^{2+} relaxation

The distance between adjacent sarcomeres (local sarcomere length) was measured in Alexa594-wheat germ agglutinine line-scan images. Local sarcomere length was quantified at 15 spaced time points between the initiation of local contraction and the maximal local re-lengthening, always measuring the maximal local contraction, similar to Hohendanner et al. [33]. The time constant of local re-lengthening, τ_{sl} , was calculated by fitting an exponential to the time course of the local strain at different positions along the scan-line. The maximum contraction/deformation (minimum sarcomere length) ϵ_l^{max} , was obtained at the same locations.

The local Ca^{2+} transients (F) were obtained for the same points of the line-scan where sarcomere contraction was measured, from the $[Ca^{2+}]$ -dependent fluorescence intensity line-scan images. Ca^{2+} transients were normalized to the fluorescence intensity at rest (F_0) as F/F_0 . All normalized Ca^{2+} transients were quantified by calculating the maximum $[Ca^{2+}]$ amplitude Ca_{max}^{2+} , and the time constant of $[Ca^{2+}]$ decay τ_{Ca} , obtained by means of fitting an exponential to the decay of the normalized $[Ca^{2+}]$ transient (from 90% amplitude to end of cycle).

Then, both τ_{sl} and ϵ_l^{max} were compared to local τ_{Ca} and Ca_{max}^{2+} respectively of the $[Ca^{2+}]$ transient simultaneously recorded at the same position.

Analysis of the local strain profiles

Since the number of pixels of the full line-scan were high and therefore, manual quantification would be tedious and time consuming, we developed an automatic tool to estimate the local strain at all the single time points along the line-scan.

For this, local cellular deformation was measured in transmitted laser light line-scan images by automatic image processing, using a custom Graphical User Interface (GUI) implemented in *MATLAB (2013b, The Math-Works Inc., Natick, MA)*. With this tool, an estimation of the local strain could be obtained at each time frame. Briefly, the cross-correlation of transmitted laser light line-scan images was performed to obtain the local velocities. Then, the velocity gradient was computed to obtain the strain rate.

Finally, strain was computed as the integral of the strain rate.

The tracking of each pixel of the line-scan across time was also performed. To do this the corresponding position of each pixel at every time point was estimated from the calculated local velocities.

Local strain curves as a function of time were obtained for each pixel of the line-scan. Then, all the local strain curves were averaged and the temporal moment corresponding to the maximum cellular contraction was identified. Finally, a curve of the local strain at maximum contraction along the line-scan was also obtained.

Analysis of the local Ca^{2+} transients

The local Ca^{2+} transients (F) were obtained for all the points of the line-scan from the $[Ca^{2+}]$ -dependent fluorescence intensity line-scan images, taking into account the variation in the pixel's position across time due to cell contraction. Also, the global Ca^{2+} transient was obtained as the average of all the local Ca^{2+} transients. All global and local Ca^{2+} transients were normalized to the fluorescence intensity at rest (F_0). The maximum $[Ca^{2+}]$ amplitude was obtained for all the normalized Ca^{2+} transients.

In order to quantify the Ca^{2+} re-uptake in a similar way as done in [33], all normalized Ca^{2+} transients were quantified by calculating the time constant of $[Ca^{2+}]$ decay τ_{Ca} , obtained by means of fitting an exponential to the decay of the normalized $[Ca^{2+}]$ transient (from 90% amplitude to end of cycle).

Then, to later construct the excitation-contraction functions that will be introduced in the model, all normalized Ca^{2+} transients (F/F_0) were fitted with a sum of two Boltzmann functions (Equation 6.1), to construct the global and local cytosolic calcium functions $Z(t)$.

$$Z(t) = a \cdot t \cdot \exp\left(-\frac{bt^2}{2}\right) + c \cdot t \cdot \exp\left(-\frac{dt^2}{2}\right) \quad (6.1)$$

6.2.2 Description of the model

Passive mechanical properties of the cardiomyocyte

Similarly to other cardiac myocytes models [47], the cell was assumed to behave as an inhomogeneous nearly-incompressible hyperelastic Mooney-Rivlin medium, characterized by a strain-energy function given by:

$$W = C_{10}(\bar{I}_1 - 3) + C_{01}(\bar{I}_2 - 3) + D_1(J - 1)^2 \quad (6.2)$$

where \bar{I}_1 and \bar{I}_2 are the first and second invariants of the modified right Cauchy-Green strain tensor, $\bar{\mathbf{C}} = J^{-2/3}\mathbf{C}$, with J the local volume change.

6.2. Methods

C_{10} , C_{01} and D_1 are material constants. The shear modulus (G) is $G = 2(C_{10} + C_{01})$. The material constants can be related to the elastic Young's modulus (E) and poisson ratio (ν) through the following relationships: $E = 9\kappa G / (3\kappa + G)$ and $\nu = (3\kappa - 2G) / 2(3\kappa + G)$. ν was set to 0.49 and D_1 is half the finite bulk modulus of a nearly incompressible material: $\kappa = 2D_1$.

In one of the simulated cells, the nucleus was visible and therefore it was additionally modeled. The nucleus was considered as a linear elastic and nearly-incompressible medium with Poisson's ratio $\nu_{nucleus} = 0.49$.

Active mechanical properties of the cardiomyocyte

The active stress (\mathbf{S}_{act}) generated by the active fibers within the cell was modeled as an active tension (T_{act}) generated along the direction given by the sarcomeres orientation in the reference configuration (\mathbf{d}^k) calculated as: $\mathbf{S}_{act} = T_{act} \mathbf{D}^k$, where the tensor $\mathbf{D}^k = \mathbf{d}^k \otimes \mathbf{d}^k$ is defined by the fibre system direction vector \mathbf{d}^k (unit). Then, (T_{act}) was computed as:

$$T_{act} = A \cdot f_{max} \exp \left\{ - \left(\frac{\varepsilon - \varepsilon_{opt}}{s} \right)^2 \right\} \quad (6.3)$$

where $\varepsilon = \frac{1}{2}(\bar{\mathbf{C}} : \mathbf{D}^k - 1)$ is the Green strain along the fiber direction \mathbf{d}^k , ε_{opt} is the optimal deformation and was set to 0.01 and s represents the sensitivity of the actin-myosin overlaps, assumed to be 1.0. f_{max} is the maximal tension that can be delivered by the sarcomere. Only fibers in the longitudinal direction were considered so $k = 1$. A is a calcium concentration-dependent function modeling the excitation-contraction coupling.

Coupling active stress with calcium concentrations

It is known that the amount of active stress that can be generated by the sarcomeres (T_{act}) depends on the amount of cytosolic Ca^{2+} available. Therefore, A was defined as an activation function modeling the Ca^{2+} -dependent contraction process. This process was described by the Hill function as follows:

$$A(Z(t)) = \frac{Z^{nH}}{Z_{50}^{nH} + Z^{nH}} \quad (6.4)$$

where nH is the Hill coefficient ($nH > 0.0$), $Z(t)$ represents the cytosolic Ca^{2+} and Z_{50} the half-maximum concentration of cytosolic Ca^{2+} .

Initial conditions of Young's modulus

In order to define the initial values for the local Young's modulus E within the cell domain, a relationship between the local strain and the local Young's

modulus was obtained. To do this, a two dimensional rectangular mesh with rectangular elements was constructed to mimic a cardiac cell of size $100\mu m \times 25\mu m$. f_{max} was set to obtain a global cell shortening of about 8-10% with an E equal to 30kPa, according to the values reported by Pustoc'h et al for adult rat cardiac cells [47]. For simplicity, A was modeled as a gaussian function with a width equal to the 25% of the whole contraction period, as measured in [47] and a maximum amplitude of 1.0. The E of the rectangular cell was varied from 10 to 100kPa, chosen to cover all the possible Young's moduli within a cardiomyocyte. The maximum strain along the longitudinal direction of the rectangular mesh (ϵ_l^{max}) was obtained. Then, the $\epsilon_l^{max} = f(E)$ relationship was computed using only some of the simulated values of E (10, 30, 50, 70 and 100kPa). To do this, the data was transformed to a logarithmic scale and the regression equation (f) was computed after 3rd degree polynomial fitting of the data ($\ln(\epsilon_l^{max}) = f(\ln(E))$). Using the calculated equation f , the estimated maximum longitudinal strain ($\hat{\epsilon}_l^{max}$) for the remaining E values (that were not used to calculate f) was estimated. Finally, the relative error between the simulated ϵ_l^{max} and the estimated $\hat{\epsilon}_l^{max}$ strains was computed as: $100 * (\hat{\epsilon}_l^{max} - \epsilon_l^{max}) / \epsilon_l^{max}$, to evaluate the goodness of fit equation.

6.2.3 Multi-parametric analysis of the local strain

The relationship between the different active and passive mechanical properties that are involved during the excitation-contraction process, and the strain was analyzed by multiparametric analysis. The set of input variables were:

- Ca^{2+} transient amplitude (Ca_{max}^{2+}).
- Time constant of Ca^{2+} transient decay (τ_{Ca}).
- Young's Modulus (E).
- Maximal active force (f_{max}).

The output variables were:

- Maximum contraction amplitude (or minimum longitudinal strain) (ϵ_l^{max}).
- Time constant of sarcomere re-lengthening (τ_{sl})

Five different possible values within their physiological range were defined for each input variable. All the possible combinations between the input variables were simulated and the output variables were obtained for all of them. A multivariate linear regression analysis was performed to evaluate the relationship between all the input and output variables.

6.2.4 Cell-specific finite-element simulation of a cardiomyocyte contraction

The transmitted light image from the rat cardiomyocytes were manually delineated to obtain the cell boundary. Then, 2D meshes with triangular elements were built with Gmsh [156] (see Figure 6.7(a)). In all the cells, a region of 0 displacement could be observed (see region highlighted with a red rectangle in Figure 6.2(b)). The corresponding locations of this region within the cells were also identified.

In those cells where the nucleus was visible, it was delineated and meshed too, and defined as a subdomain inside the 2D cell whole domain.

Defining cell-specific input data

The activation function $A(t)$ were defined using the equation 6.4, where $Z(t)$ were calculated from the fitting of the experimentally measured Ca^{2+} transients with the equation 6.1. The Hill coefficient nH was set to 4, and Z_{50} was calculated from the global Ca^{2+} transient.

Two possible scenarios were considered. The first one assuming an homogeneous global Ca^{2+} -dependent activation in the whole cell (calculated from the experimentally measured global Ca^{2+} transient), and a second one considering all the different local Ca^{2+} -dependent activation functions, calculated from the experimentally measured local Ca^{2+} transients.

Then, the initial values for the local Young's modulus E_0^i were calculated for each position along the line-scan using the equation that describes the relationship between the maximal longitudinal strain ϵ_l^{max} and E , calculated in section 6.2.2). In order to reduce the computational complexity, a piecewise linear variation of the elastic Young's modulus was assumed along the longitudinal axis of the cell. Therefore, the measured strain along the line-scan at maximum contraction point, was segmented in small regions with approximately a linear variation of the strain. Then, the $E^i(x)$ inside each region was approximated as:

$$E^i(x) = \frac{E_0^{i+1} - E_0^i}{x_{i+1} - x_i} (x - x_i) + E_0^i \quad \forall x \in [x_i, x_{i+1}] \quad (6.5)$$

where x_i and x_{i+1} define the beginning and end of the region i , and E_0^i and E_0^{i+1} the estimated E_0 corresponding to these positions.

Finally, the maximum active tension f_{max} was manually fixed to obtain a simulated global cell shortening equal to the observed one.

Numerical equations and boundary conditions

The equilibrium equation to solve was defined as:

$$\int_{\Omega^{(0)}} (\mathbf{S}^{eff}(\mathbf{u}) + K(J-1)J\mathbf{C}^{-1}) : d\boldsymbol{\varepsilon}(\mathbf{v})dV \quad (6.6)$$

where $\mathbf{S}^{eff}(\mathbf{u})$ is the effective stress calculated as the sum of the passive (\mathbf{S}_{pas}) and the active (\mathbf{S}_{act}) stress $\mathbf{S}^{eff} = \mathbf{S}_{pas} + \mathbf{S}_{act}$.

S_{pas} was calculated as:

$$\begin{aligned} \mathbf{S}_{pas}(\mathbf{u}) = & \mu J^{-\frac{2}{3}} (\mathbf{I} - \frac{1}{3} tr(\mathbf{C}) \mathbf{C}^{-1}) \\ & + \kappa J^{-\frac{4}{3}} (tr(\mathbf{C}\mathbf{I} - \mathbf{C} - \frac{2}{6} ((tr\mathbf{C})^2 - tr(\mathbf{C}^2))) \mathbf{C}^{-1}) \end{aligned} \quad (6.7)$$

and $\mathbf{S}_{act} = T_{act} \mathbf{D}^k$ where T_{act} was calculated as described in equation 6.3.

The equilibrium equation was numerically solved using a finite element method implemented in *Python, SfePy* [157] in the 2D domain.

The Robin boundary condition $\mathbf{S} \cdot \mathbf{n} + \alpha \cdot \mathbf{u} = 0$ was imposed on the cell boundary: Γ_0 , where \mathbf{n} is the normal vector to cell membrane Γ_0 and α is a parameter representing the elastic response due to the presence of surrounding fluid hindering and constraining the motion of the cell, and equal to $\alpha = 1 \times 10^{-2}$ as done in similar cell models [46]. This kind of boundary conditions seems to be the more suitable for modeling free cardiac cells according to Ruiz et al. [46]. Additionally, a Dirichlet boundary condition (zero displacement condition) was imposed in the cell region with 0 displacement identified in the line-scan transmitted light image (see Figure 6.2(b)).

Inverse problem solution to estimate the local elastic parameters

The local elastic Young's moduli (E^i) along the line-scan were estimated by a constrained nonlinear optimization algorithm minimizing the root mean square error (RMSE) between the simulated and measured strain profiles along the line-scan at maximum contraction time point. Additionally, in those cases where the cell nucleus was included, the elastic modulus of the nucleus was also estimated.

6.3 Results

6.3.1 Evaluation of the experimentally measured relationship between local calcium and contraction

Local maximal contraction ε_l^{max} and time of local sarcomere re-lengthening τ_{sl} were quantified manually in the T-tubule stained line-scan images at 11

6.3. Results

± 2 different positions along the line-scan and compared to Ca_{max}^{2+} and τ_{Ca} respectively of the local Ca^{2+} transient simultaneously recorded at the same position, in three different cardiomyocytes. In the three cells, a negative linear correlation was found between Ca_{max}^{2+} and ϵ_l^{max} ($R=-0.61 \pm 0.02$) (see Figure 6.1(b)). Moreover, τ_{sl} was positively correlated with τ_{Ca} . ($R=0.57 \pm 0.13$) (see Figure 6.1(a)).

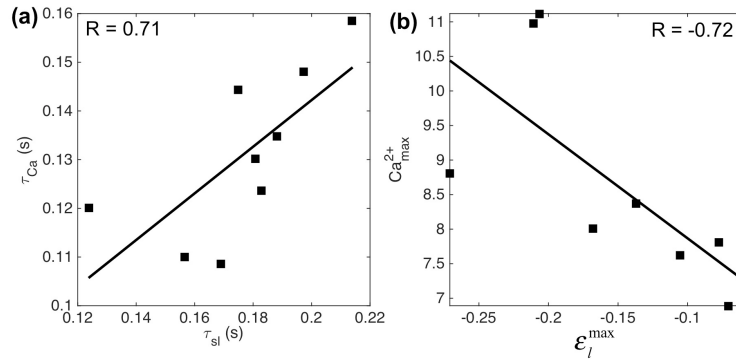


Figure 6.1: (a) Correlation between local time of sarcomere re-lengthening (τ_{sl}) and local time of Ca^{2+} decay (τ_{Ca}) in one of the three cardiac cells. (b) Correlation between local maximal contraction (ϵ_l^{max}) and local maximum Ca^{2+} amplitude (Ca_{max}^{2+}) in one of the three cardiac cells.

6.3.2 Quantification of the local strain and Ca^{2+} transients

In Figure 6.2, the different images recorded during the cardiomyocyte electrical stimulation experiments are depicted. The cell morphology and the line-scan along the longitudinal direction of the cell can be seen in Figure 6.2(a). On the Right panel of Figure 6.2, the two line-scan images: the transmitted light image where the sarcomeres are visualized (Fig. 6.2(b)), and the confocal Fluo-4 image, corresponding to cytosolic $[Ca^{2+}]$ (Fig. 6.2(c)), are plotted for two consecutive beats. The stimulation frequency was 1Hz. The vertical axis corresponds to the line-scan (blue arrow) and the horizontal axis to time.

Local and global Ca^{2+} transients are depicted in Figure 6.3(a)-(b). A high variability in the local Ca^{2+} transients can be observed. The global Ca^{2+} transient fitted with the two Boltzmann functions is also plotted, showing a good fitting. All the activation functions $A_i(t)$ calculated from the local Ca^{2+} transients are plotted in 6.3(c).

The estimated local strain from the transmitted light line-scan image of Figure 6.2(b) together with the local and averaged strain curves for all the points along the line-scan for one beat are shown in Figure 6.4.

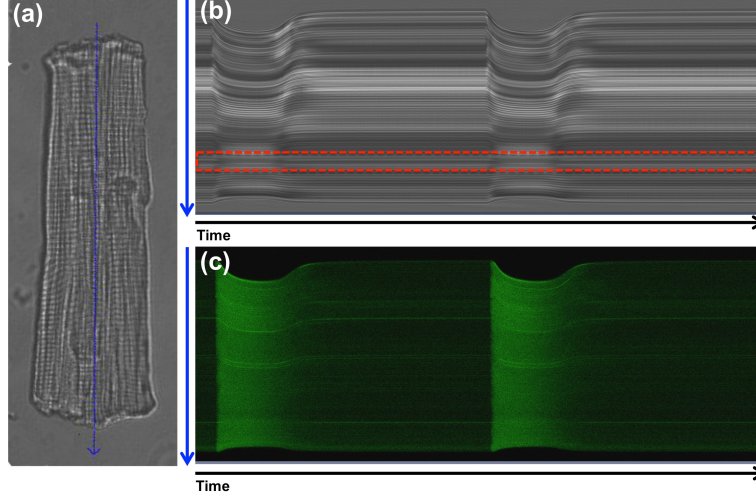


Figure 6.2: (a) Transmitted light image of the whole cell. The blue arrow corresponds to the line-scan where the images acquisition was performed. (b) Line-scan transmitted light image and (c) confocal Fluo-4 image corresponding to cytosolic $[Ca^{2+}]$. The vertical axis corresponds to the line-scan (blue arrow) and the horizontal one to the time. The red box indicates the zone with 0 displacement.

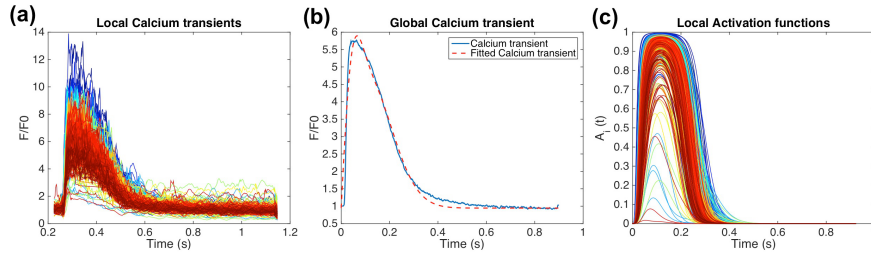


Figure 6.3: (a) Local Ca^{2+} transients. (b) Global measured (solid line) and fitted with two Boltzmann functions (dash line) Ca^{2+} transients. (c) Activation A_i functions calculated from the local Ca^{2+} transients in (a).

6.3.3 Initial conditions for Young's modulus: relationship between elasticity and strain

The longitudinal strain at maximum contraction (or minimum longitudinal strain) (ϵ_l^{max}) was plotted against the different Young's modulus E . The polynomial equation obtained after the curve fitting was:

$$\ln(\hat{\epsilon}_l^{max}) = -0.0706 \cdot \ln(E)^2 - 0.327 \cdot \ln(E) - 0.5461 \quad (6.8)$$

The estimated maximum longitudinal strain $\hat{\epsilon}_l^{max}$, was calculated using the equation 6.8 for the rest of simulated E values not used in the curve

6.3. Results

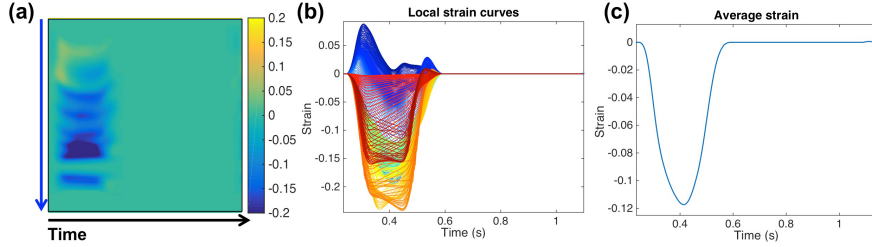


Figure 6.4: (a) Image with the estimated local strain calculated from the image shown in Figure 6.2(b). The vertical axis corresponds to the line-scan (blue arrow) and the horizontal represents the time. (b) All the local strain curves along the line-scan for the first beat. (c) Average of all the local strain curves.

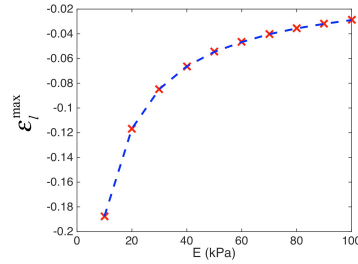


Figure 6.5: Maximum longitudinal strain (ϵ_l^{max}) plotted against the different Young's modulus E .

fitting (20, 40, 60, 80 and 90 kPa). The mean relative error between $\hat{\epsilon}_l^{max}$ and ϵ_l^{max} was 0.31%. Therefore, given a specific longitudinal maximum strain, the corresponding Young's modulus E can be obtained by solving the inverse of the Equation 6.8.

6.3.4 Multi-parametric analysis of the local strain

The results of the multivariate linear regression analysis are shown in Table 6.1 for both the amplitude of maximum contraction (minimum longitudinal strain) ϵ_l^{max} , and the time of relaxation or re-lengthening time τ_{sl} . The maximum deformation not only depends on the amount of available Ca^{2+} and on the maximum force generated by the sarcomeres, but also depends on the passive elasticity of the cell. In fact, the maximum correlation for ϵ_l^{max} is obtained for the maximum force generated by the sarcomeres and the passive elasticity of the cell. On the other hand, the time for relaxation depends mainly on how fast the Ca^{2+} is re-uptaken and/or extruded from the cytosol.

Table 6.1: Results from the multivariate regression analysis for the maximum contraction amplitude and the time of re-lengthening.

	ϵ_l^{max}		τ_{sl}	
	Coefficient	p	Coefficient	p
Ca_{max}^{2+}	-0.366	< 0.001	-0.035	0.09
τ_{Ca}	-0.002	0.909	0.843	< 0.001
E	0.564	< 0.001	-0.102	< 0.001
f_{max}	-0.585	< 0.001	0.093	< 0.001

R-squared (S_{max}): 0.79, p-value = 0.0.R-squared (τ_{sl}): 0.73, p-value = 0.0

ϵ_l^{max} , maximum contraction amplitude (minim longitudinal strain); τ_{sl} , time of re-lengthening, τ_{Ca} , time constant of the Ca^{2+} decay; E , Young's modulus; f_{max} , maximum active force developed by the sarcomeres.

6.3.5 Cell-specific simulation of a cardiomyocyte contraction

The cell-specific finite-element simulations of three different cardiomyocytes contractions were successfully performed for both homogeneous and heterogeneous activation conditions. The cell meshes contained in averaged 6090 cells and 3169 nodes. The RMSE of the cell-specific fittings was below 0.02 in all cases, with homogeneous and heterogeneous activation, as detailed in Table 6.2. Figure 6.6(a) shows one of the 2D cell meshes corresponding to the cardiomyocyte illustrated in Figure 6.2(a), together with the deformed mesh at maximum contraction time, for the heterogeneous activation. Colormap indicates the local longitudinal strain. Figure 6.6(b) shows the measured longitudinal strain along the line-scan (dash black line) together with the simulated one at a maximum contraction time frame for both activation types: homogeneous (red line) and heterogeneous (blue line). The two simulated strain curves were quite similar compared to the measured one. The local estimated Young's modulus along the line-scan was plotted for both simulated situations in Figure 6.6(c), showing almost identical results in both cases. A very similar behavior was also observed in the other two cells.

The RMSE, percentage of total cell shortening and mean and nuclear Young's modulus for both simulated scenarios and for the three cells are shown in Table 6.2. Also the Pearson's correlation between the estimated local E and the local maximum contraction was calculated (Table 6.2). In all the simulations a significant positive correlation between E and strain was obtained and it was very similar to the correlation coefficient obtained from the multiparametric analysis.

Finally, a virtual line-scan image was created by plotting the local displacements of the cell points along the line-scan across time. Figure 6.7

6.4. Discussion

Table 6.2: Results of the cell-specific simulations performed for three different cardiomyocytes.

Cell	Activation	RMSE	% cell shortening	mean (E)	$E_{nucleus}$	ρ
Cell 1	Local	0.0141	11.32%	65.06kPa	-	0.43**
	Global	0.0137	11.54%	65.14kPa	-	0.46**
Cell 2	Local	0.0138	11.41%	56.84kPa	-	0.60**
	Global	0.0128	11.61%	45.31kPa	-	0.53**
Cell 3	Local	0.0132	7.88%	84.29kPa	30kPa	0.68**
	Global	0.0138	7.82%	81.24kPa	30kPa	0.70**

ρ denotes Pearson's correlation coefficient; ** $p < 0.001$.

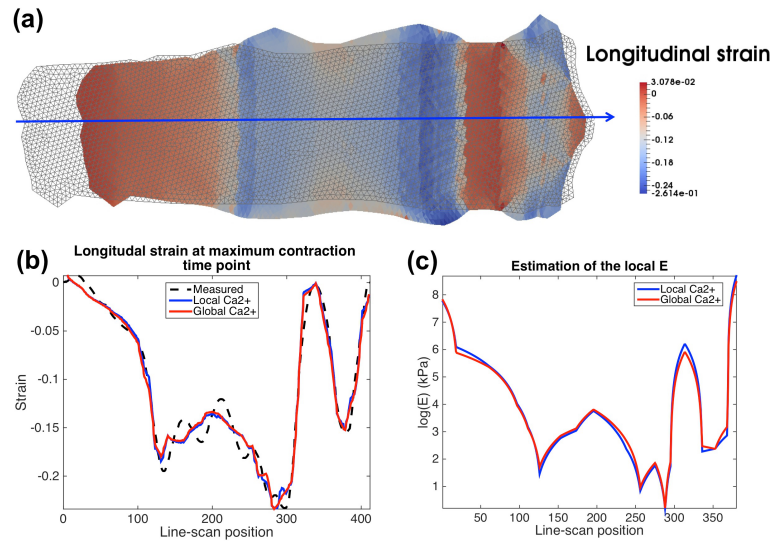


Figure 6.6: (a) Undeformed (grey) and deformed cell mesh in the maximum contraction time frame. Colormap indicates the simulated longitudinal strain. (b) Measured (black dash line), and simulated strain curves obtained along the line-scan (blue arrow) at maximum contraction time frame, for an homogeneous (red line) and heterogeneous (blue line) activation. (c) Logarithm of the estimated Young's modulus (E) for an homogeneous (red line) and heterogeneous (blue line) activation.

illustrates the high similarity between the real line-scan image and the virtual one.

6.4 Discussion

We presented a simplified two-dimensional electromechanical model of a cardiomyocyte that considered the heterogeneity in the mechanical properties of a cardiac cell. Finite-element modeling has emerged as an alternative

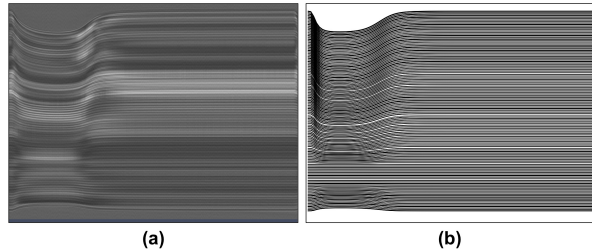


Figure 6.7: Comparison between the (a) real line-scan transmitted light image and a (b) virtual line-scan image created by plotting the local displacements of the simulated cell points across time.

to the AFM for measuring the local mechanical cell properties. Several two and three dimensional models of cardiomyocytes based on a continuum mechanical framework have been published [45–47, 158–160]. However, in all of them an isotropic distribution of the mechanical properties in the whole cell has been assumed. Our proposed simplified two-dimensional electromechanical cell model overcame this limitation by taking into account the local deformation and cytosolic Ca^{2+} concentration experimentally measured to define the variables of the constitutive laws locally, that described the electro/mechanical behavior of the cell. The correlation between the amplitude and duration of cell contraction and the different mechanical properties was assessed by a multiparametric analysis showing that the amount of contraction was determined mainly by the the cell elasticity together with the amount of force generated by the sarcomeres and in to lesser degree, by the cytosolic $[Ca^{2+}]$. On the other hand, the duration of cell contraction was mainly defined by the duration of the Ca^{2+} transient. Finally, the cell-specific variation of Young’s modulus along the longitudinal axis of the cell were successfully estimated in three different cardiac cells by the finite-element method, showing the heterogeneity in the elastic modulus within the cells.

The results from the multi-parametric analysis have shown that the duration of the cell contraction was mainly determined by the duration of the Ca^{2+} transient. These results agreed with the manual measurements performed in the three cells which showed a positive significant correlation between the time of sarcomere re-lengthening (τ_{sl}) and the time of $[Ca^{2+}]$ decay (τ_{Ca}). This result is also supported by previously published studies on cardiomyocytes reporting also a significant correlation between the both local and global τ_{sl} and τ_{Ca} [33]. The results of the multi-parametric analysis also suggested that the regional differences in the cellular deformation were mainly due to the local elasticity of the cell and the amount of force produced by the sarcomeres, rather than the local cytosolic $[Ca^{2+}]$. The re-

6.4. Discussion

sults from the cell-specific simulations also support this hypothesis, since the local cell elasticity estimated when considering an homogeneous Ca^{2+} activation function was practically identical to the local elasticity estimated when the local Ca^{2+} transients were used to construct the activation functions, suggesting that the local Ca^{2+} information is not adding value to the model, and therefore a global homogeneous activation could be considered instead. Also, the averaged Young's modulus that were obtained in our simulations agreed with the reported values in rat cardiac cells [47, 151, 153] as well as the global cell shortening.

Previous studies have demonstrated that there are significant variations of the values of Young's modulus at different regions of the cardiac cell [151–154]. A study on atrial cardiomyocytes [155] revealed that cardiac cells are softer at the nuclear region and become stiffer toward the periphery. This agreed with our results from the cell-specific simulations, since for the three cells we found that the Young's modulus seemed to be higher in the cellular extremes. Also, when the nucleus was included in the model, a lower elastic modulus compared to the mean elastic modulus of the cell was estimated. The same study of Shroff et al. stated that the stress fibers shown areas with high stiffness (elastic modulus between 100-200kPa) embedded in softer parts of the cell (elastic modulus between 5-30 kPa) [155]. An analysis of fluorescent images together with the elasticity maps obtained by AFM revealed that the variation of elastic properties across the cardiomyocyte was correlated with the cytoskeleton heterogeneity [161], specifically to the actin network of the cell cytoskeleton [151]. Additionally, changes in mechanical properties and cytoskeleton reorganization has been also described in cell aging [153] and under pathogenesis [151]. Regarding the sarcomere uniformity inside the cell, Brady et al [162] reported that in isolated unattached cardiac cells, the sarcomere pattern both at rest and during isotonic contractions was remarkably uniform, resulting in an overall sarcomere length variation of only $\pm 6\%$, and the major sarcomere length deviation was noted near the nuclei. However, regional variations in the onset of relaxation were observed during the active shortening that lead to a greater dispersion of sarcomere lengths. All these experimental studies supported our results showing that the heterogeneity in the cellular deformation seems to be mainly caused by the regional differences in the cell elasticity and, this variation can be explained by differences in the cytoskeleton architecture and organelles.

However some limitations of the present model deserve to be discussed. The first one concerns the geometrical simplification of the cell and the subsequent assumption of plane stress with zero stress in the perpendicular direction. Secondly, even if most of the biochemical and biomechanical processes were simplified in the our model, the present model was able to suc-

cessfully recreated the local and global behavior of electrically stimulated contracting cardiomyocytes. Thirdly, we are considering only heterogeneity in the longitudinal direction of the cell while assuming homogeneity in the transversal direction, due to the lack of experimental data on the transversal direction. Finally, we acknowledge that in order to further validate our model, experimentally measured elastic modulus should be compared with the estimated by the model in the same cell.

6.5 Conclusions

In conclusion, our proposed electromechanical model of a cardiomyocyte seems to be a good approximation to assess the local mechanical properties such as passive elasticity within a normal cardiomyocyte and offers a relevant basis for understanding the spatial heterogeneity in the mechanical properties and deformation. Our results suggested that the heterogeneity in the local deformation is caused mainly by the regional variation on the cell elasticity, that could be attributed to local changes in the cytoskeleton of the cell. Therefore, this model could provide a starting point for an extended analysis of the relationship among regional cell mechanical behavior and the underlying biochemical and/or structural environment, in both physiological and pathological context.

CHAPTER **7**

Conclusions

7.1 General conclusions

This thesis has focused on the development and validation of different computational models and tools to improve the understanding of intra-uterine cardiac remodelling at different scales. This goal was accomplished by:

1. The development and validation of a simplified lumped model of the fetal circulation. This model was used to improve the understanding of brain-sparing effect of IUGR fetuses.
2. The use of our previous simplified model of the fetal circulation to better understand the changes of AoI blood flow throughout the gestation and the origins of the brief end-systolic peak of reversal flow in the AoI, observed in healthy fetuses during the third trimester of pregnancy.
3. The extension of the previous lumped model of the fetal circulation by including more vessels and organs of the downstream circulation. The model was successfully used to estimate the patient-specific vascular properties in a population of more than 30 normal and IUGR fetuses. The results arising from this study improved the understanding of the underlying mechanisms of placental insufficiency and the detection of fetuses with an adverse perinatal outcome.
4. The implementation and validation of an image processing tool to automatically extract the morphometric characteristics of myofibrils of sarcomeres, from second-harmonic microscopy images of cardiac tissue. This tool allowed the characterization of sarcomere distances in both human and rabbit fetal hearts.
5. The development of a two-dimensional electromechanical model of a cardiomyocyte taking into account the heterogeneities of the mechanical (active and passive) properties.

7.2 Overview

We next summarize the advances presented in previous chapters and discuss the problems encountered.

The first three chapters were focused on the study of the fetal circulation, blood flow redistribution and vascular remodelling in healthy and IUGR fetuses. The main conclusions arising from these three studies are summarized below.

In *chapter 2* we presented a simplified equivalent lumped model of the fetal circulation. The proposed equivalent lumped model seemed to be a

7.2. Overview

good approximation to assess hemodynamic changes in the fetal circulation under abnormal growth conditions. Further developments of the model can be useful for assessing additional vessels and their interactions under various clinical conditions, and the impact of interventions. The model was used to study the blood flow redistribution in IUGR fetuses, focusing on the blood flow changes in the AoI and MCA. Our results suggested that AoI flow is affected by peripheral-placental as well as cerebral resistances while MCA flow mainly depends on cerebral resistance. Furthermore, when personalizing the model to IUGR fetuses we were able to estimate the specific vascular resistances variation, suggesting that the peripheral-placental resistance is the major determinant for observed changes in measured Doppler flows. This study supports the potential role of AoI as marker of adverse perinatal and neurological outcome since it is a central vessel connecting the two ventricular outputs and therefore its flow reflects the balance between ventricular output and upper/lower body vascular resistances. Personalizing the model shows promise to directly assess properties of the vascular bed and placenta rather than inferring them from Doppler indices.

In *chapter 3* we proposed to use the model implemented in the previous chapter to study how the AoI blood flow pattern changes throughout the gestation and to investigate the origins of the end-systolic notch that appears in the AoI blood flow velocity waveform at last trimester of gestation. We demonstrated that the characteristic notch in the AoI at the end of systole, and at late gestation, occurs mainly as a result of a delayed and longer ejection of the right ventricle as compared to the left, and therefore is not artifactual as suggested by Del Rio et al. [20]. Additionally, we demonstrated that our lumped model is an useful tool that allows the estimation of patient-specific parameters that cannot be assessed clinically, helping to improve the understanding of the hemodynamic changes in the fetal circulation throughout gestation.

In *chapter 4* we extended our previous lumped model of the fetal circulation by adding new arteries and organs of the downstream fetal circulation. We demonstrated that the extended patient-specific lumped model of the fetal circulation successfully estimated a set of fetal vascular and hemodynamic properties that cannot be assessed in a clinical setting. Also, we analyzed the correlation between Doppler and model-based parameters and we found that UA-PI was correlated with both placental resistance and compliance, while UtA-PI was correlated mainly with the placenta compliance, suggesting that the two parameters are describing different fetal/maternal placental problems. Finally we shown that the combination of a set of these model-based parameters with the conventional Doppler indices resulted in the improvement of the detection of fetuses with an adverse perinatal outcome.

The last two chapters were focused on the study of the cardiac remodelling at cellular and subcellular level. The main conclusions arising from these two last studies are summarized below.

In *chapter 5* we presented an image processing tool to automatically measure the sarcomere distances in second-harmonic generation images. We firstly validated our tool in computer-generated cardiac fibers and then in real images with different quality conditions. Our approach based on automated autocorrelation analysis shows similar results to manual delineations and is a robust technique provided a sufficient SNR in the images. We have evaluated the impact of noise, amplitude modulation and fiber twisting and minimal errors were found for images beyond 20dB, which is a realistic amount for automated histology analysis. We further supported our numerical results of computer generated data with real experiments based on two different acquisition conditions. The results showed that our technique for measuring the sarcomere distances is accurate and allows to reproduce changes previously described, concerning changes in the SL under pathological conditions [26–28]. Finally, our methodology was successfully applied to measure sarcomere distances in a fetal human control-case study [21] and also in an animal model of IUGR [22], reporting shorter cardiac sarcomere length in rabbits and human fetuses with intrauterine growth restriction.

Finally, in *chapter 6* we presented a two-dimensional electromechanical model of a cardiomyocyte to estimate the local mechanical properties within the cell based on experimentally measured data to then perform cell-specific simulations. Our proposed electromechanical model of a cardiomyocyte seems to be a good approximation to assess the local mechanical properties such as passive elasticity within the cell and offers a relevant basis for understanding the heterogeneity in the mechanical properties and deformation. Our results suggested that the heterogeneity in the local deformation is caused mainly by the regional variation in the cell elasticity, that could be attributed to local changes in the cytoskeleton of the cell. Therefore, this model could provide a starting point for an extended analysis of the relationship among regional cell mechanical behavior and the underlying biochemical and/or structural environment, in both physiological and pathological context.

7.3 Future perspective

Future research should mainly focus on further validation and exploitation of the results arising from this thesis by personalizing our proposed computational models in a large population of patients of intra-uterine cardiac remodelling.

7.3. Future perspective

Regarding the model of the fetal circulation, results from the third study interestingly point to that the different placental vascular properties assessed by the computational model, such as the placental resistance and compliance, seemed to be differently associated to the various causes of placental damage. However, the current model is too simple and a more detailed/complex model is necessary to further investigate the different fetal and/or maternal placental abnormalities and their impact on the fetal circulatory system. Therefore, the next step will be to implement a detailed model of the placental and maternal circulation and to carefully couple it with the already developed fetal circulation lumped model.

Another interesting point is that the heart has not been modeled and therefore the model was not a closed system. In all the different studies of the fetal circulation real blood flow waveforms from the aortic and pulmonary outflow tracts were used instead, and a venous pressure of 0 mmHg were considered. To cope with these limitations the development of a heart model should be necessary. Moreover, coupling the fetal heart and the circulation models will allow for a better understanding of the cardiac remodelling at the organ level and its direct involvement in the fetal circulation. As a last step, it would be interesting to study the long term consequences of the cardiovascular remodelling. Therefore, the coupled model should be adapted to study the cardiovascular system of the growing child in relation to the initial cardiovascular system that it was born with, depending on intra-uterine conditions.

We may also think about some additional applications of the proposed computational models such as the evaluation of the long-term consequences of fetal cardiovascular remodelling, the evaluation of the potential beneficial effect of different therapeutic strategies and also the evaluation of the effect of age per se and other risk factors related to age (hypertension, hypercholesterolemia, sedentary lifestyle and smoking).

Finally, regarding the last part of this thesis on the study of cardiac cell remodelling, there are some interesting points to address in the future. Results arising from the measurement of sarcomere length in human fetuses [21] and also in fetuses and adult rabbits of an animal model of IUGR [22], performed with our tool, demonstrated that IUGR fetuses have a shorter resting sarcomere length. Then, it would be interesting to study also the influence of having different resting sarcomere lengths on the amount of force developed by the sarcomere as well as on the cell contractility. Therefore, one of the first things to solve will be to improve the current model of the active stress-sarcomere length dependence relationship. Secondly, Gonzalez-Tendero et al. [23] shown that the number of mitochondria in IUGR fetal rabbits were reduced and the space between mitochondria and myofilaments was increased. However, the consequences of these

7.3. Future perspective

alterations regarding the function and contractility of the cell are still unknown. Therefore, the next step will be to incorporate the mitochondria into the model and to study the effects of having less mitochondria and a large distance between mitochondria and myofilaments. Finally, it would be interesting also to incorporate a simple model of the T-Tubule network and to investigate the effect of having different densities of T-tubules into the Ca^{2+} velocity wave propagation, since for example, in some pathologies a deterioration of the T-tubule network could be observed [31, 150]. Also, IUGR fetal cardiac cells show a longer period of Ca^{2+} re-uptake (data not published) and this might be related to alterations in the immature and still-developing T-tubule network and its related proteins such as SERCA2.

References

- [1] S. Allender, P. Scarborough, V. Peto, M. Rayner, J. Leal, R. Luengo-Fernandez, and A. Gray, *European cardiovascular disease statistics*. European Heart Network, Brussels, European Society of Cardiology, Sophia Antipolis, 2012.
- [2] G. S. Berenson, “Childhood risk factors predict adult risk associated with subclinical cardiovascular disease. The Bogalusa Heart Study.,” *Am. J. Cardiol.*, vol. 90, pp. 3L–7L, Nov. 2002.
- [3] A. W. Zieske, G. T. Malcom, and J. P. Strong, “Natural history and risk factors of atherosclerosis in children and youth: the PDAY study.,” *Pediatr. Pathol. Mol. Med.*, vol. 21, pp. 213–37, Jan. 2002.
- [4] D. J. Barker, P. D. Winter, C. Osmond, B. Margetts, and S. J. Simmonds, “Weight in infancy and death from ischaemic heart disease,” *Lancet*, vol. 2, no. 8663, pp. 577–580, 1989.
- [5] D. J. Barker, “The fetal origins of coronary heart disease.,” *Acta Paediatr. Suppl.*, vol. 422, pp. 78–82, July 1997.
- [6] A. Tintu, E. Rouwet, S. Verlohren, J. Brinkmann, S. Ahmad, F. Crispi, M. van Bilsen, P. Carmeliet, A. C. Staff, M. Tjwa, I. Cetin, E. Gratacos, E. Hernandez-Andrade, L. Hofstra, M. Jacobs, W. H. Lamers, I. Morano, E. Safak, A. Ahmed, and F. le Noble, “Hypoxia induces dilated cardiomyopathy in the chick embryo: mechanism, intervention, and long-term consequences.,” *PLoS One*, vol. 4, p. e5155, Jan. 2009.
- [7] F. Crispi, B. Bijmens, F. Figueras, J. Bartrons, E. Eixarch, F. Le Noble, A. Ahmed, E. Gratacós, and E. Gratacos, “Fetal growth restriction results in remodeled and less efficient hearts in children.,” *Circulation*, vol. 121, pp. 2427–36, June 2010.
- [8] M. Alberry and P. Soothill, “Management of fetal growth restriction,” *Arch Dis Child Fetal Neonatal Ed*, vol. 92, no. 1, pp. F62–7, 2007.
- [9] K. Hecher, S. Campbell, P. Doyle, K. Harrington, and K. Nicolaides, “Assessment of fetal compromise by Doppler ultrasound investigation of the fetal circulation. Arterial, intracardiac, and venous blood flow velocity studies.,” *Circulation*, vol. 91, pp. 129–38, Jan. 1995.
- [10] F. Crispi, E. Hernandez-Andrade, M. M. a. L. Pelsers, W. Plasencia, J. A. Benavides-Serralde, E. Eixarch, F. Le Noble, A. Ahmed, J. F. C. Glatz, K. H. Nicolaides, and E. Gratacos, “Cardiac dysfunction and cell damage across clinical stages of severity in growth-restricted fetuses.,” *Am J Obs. Gynecol*, vol. 199, pp. 254.e1–8, Sept. 2008.
- [11] M. Comas, F. Crispi, R. Cruz-Martinez, J. M. Martinez, F. Figueras, and E. Gratacós, “Usefulness of myocardial tissue Doppler vs conventional echocardiography in the evaluation of cardiac dysfunction in early-onset intrauterine growth restriction.,” *Am. J. Obstet. Gynecol.*, vol. 203, pp. 45.e1–7, July 2010.

- [12] T. Kiserud, J. Kessler, C. Ebbing, and S. Rasmussen, "Ductus venosus shunting in growth-restricted fetuses and the effect of umbilical circulatory compromise.," *Ultrasound Obstet. Gynecol.*, vol. 28, pp. 143–9, Aug. 2006.
- [13] L. K. Hornberger and D. J. Sahn, "Rhythm abnormalities of the fetus.," *Heart*, vol. 93, pp. 1294–300, Oct. 2007.
- [14] E. Eixarch, F. Figueras, E. Hernandez-Andrade, F. Crispi, A. Nadal, I. Torre, S. Oliveira, and E. Gratacos, "An experimental model of fetal growth restriction based on selective ligation of uteroplacental vessels in the pregnant rabbit," *Fetal Diagn Ther*, vol. 26, no. 4, pp. 203–211, 2009.
- [15] E. Eixarch, E. Hernandez-Andrade, F. Crispi, M. Illa, I. Torre, F. Figueras, and E. Gratacos, "Impact on fetal mortality and cardiovascular Doppler of selective ligation of uteroplacental vessels compared with undernutrition in a rabbit model of intrauterine growth restriction.," *Placenta*, vol. 32, pp. 304–9, Apr. 2011.
- [16] J. C. Fouron, M. Zarelli, P. Drblik, and M. Lessard, "Flow velocity profile of the fetal aortic isthmus through normal gestation," *Am J Cardiol*, vol. 74, no. 5, pp. 483–486, 1994.
- [17] J.-C. C. Fouron, "The unrecognized physiological and clinical significance of the fetal aortic isthmus.," *Ultrasound Obstet. Gynecol.*, vol. 22, pp. 441–7, Nov. 2003.
- [18] J. Ruskamp, J.-C. C. Fouron, J. Gosselin, M.-J. J. Raboisson, C. Infante-Rivard, and F. Proulx, "Reference values for an index of fetal aortic isthmus blood flow during the second half of pregnancy.," *Ultrasound Obstet. Gynecol.*, vol. 21, pp. 441–4, May 2003.
- [19] G. Acharya, A. Tronnes, and J. Rasanen, "Aortic isthmus and cardiac monitoring of the growth-restricted fetus," *Clin Perinatol*, vol. 38, no. 1, pp. 113–25, vi–vii, 2011.
- [20] M. Del Río, J. M. Martínez, F. Figueras, M. López, M. Palacio, O. Gómez, O. Coll, B. Puerto, M. Del Rio, J. M. Martinez, F. Figueras, M. Lopez, M. Palacio, O. Gomez, O. Coll, and B. Puerto, "Reference ranges for Doppler parameters of the fetal aortic isthmus during the second half of pregnancy.," *Ultrasound Obstet. Gynecol.*, vol. 28, pp. 71–6, July 2006.
- [21] J. I. Iruretagoyena, A. Gonzalez-Tendero, P. Garcia-Canadilla, I. Amat-Roldan, I. Torre, A. Nadal, F. Crispi, and E. Gratacos, "Cardiac dysfunction is associated with altered sarcomere ultrastructure in intrauterine growth restriction," *Am J Obs. Gynecol*, vol. 210, pp. 550.e1–7, June 2014.
- [22] I. Torre, A. González-Tendero, P. García-Cañadilla, F. Crispi, F. García-García, B. Bijnens, I. Iruretagoyena, J. Dopazo, I. Amat-Roldán, and E. Gratacós, "Permanent Cardiac Sarcomere Changes in a Rabbit Model of Intrauterine Growth Restriction," *PLoS One*, vol. 9, no. 11, p. e113067, 2014.
- [23] A. Gonzalez-Tendero, I. Torre, P. Garcia-Canadilla, F. Crispi, F. Garcia-Garcia, J. Dopazo, B. Bijnens, E. Gratacos, F. García-García, J. Dopazo, B. Bijnens, and E. Gratacós, "Intrauterine growth restriction is associated with cardiac ultrastructural and gene expression changes related to the energetic metabolism in a rabbit model," *Am J Physiol Hear. Circ Physiol*, vol. 305, pp. H1752–60, Dec. 2013.
- [24] P. Garcia-Canadilla, I. Torre, A. Gonzalez-Tendero, I. Iruretagoyena, E. Eixarch, F. Crispi, E. Gratacos, and I. Amat-Roldan, "Automated morphometric characterization of cardiac fibers by second harmonic microscopy imaging," in *Proc. 8th IEEE Int. Symp. Biomed. Imaging from Nano to Macro*, (Chicago, Illinois, USA), pp. 1379–1382, IEEE, Mar. 2011.

- [25] E. Eixarch, I. Torre, M. Illa, I. Iruretagoyena, I. Amat-Roldan, F. Crispi, F. Figueras, F. Garcia, J. Dopazo, and E. Gratacós, “Bioinformatic analysis of genes regulating myocardiocyte contractile function in a rabbit model of cardiac dysfunction due to intrauterine growth restriction,” in *Ultrasound Obstet. Gynecol.*, vol. 36, pp. 46–47, Oct. 2010.
- [26] P. G. Anderson, S. P. Bishop, and S. B. Digerness, “Transmural progression of morphologic changes during ischemic contracture and reperfusion in the normal and hypertrophied rat heart,” *Am J Pathol*, vol. 129, no. 1, pp. 152–167, 1987.
- [27] M. H. Radke, J. Peng, Y. Wu, M. McNabb, O. L. Nelson, H. Granzier, and M. Gotthardt, “Targeted deletion of titin N2B region leads to diastolic dysfunction and cardiac atrophy,” *Proc Natl Acad Sci U S A*, vol. 104, no. 9, pp. 3444–3449, 2007.
- [28] J. F. Chen, E. P. Murchison, R. Tang, T. E. Callis, M. Tatsuguchi, Z. Deng, M. Rojas, S. M. Hammond, M. D. Schneider, C. H. Selzman, G. Meissner, C. Patterson, G. J. Hannon, and D. Z. Wang, “Targeted deletion of Dicer in the heart leads to dilated cardiomyopathy and heart failure,” *Proc Natl Acad Sci U S A*, vol. 105, no. 6, pp. 2111–2116, 2008.
- [29] A. M. Gordon, E. Homsher, and M. Regnier, “Regulation of contraction in striated muscle.,” *Physiol. Rev.*, vol. 80, pp. 853–924, Apr. 2000.
- [30] A. G. Rodriguez, S. J. Han, M. Regnier, and N. J. Sniadecki, “Substrate stiffness increases twitch power of neonatal cardiomyocytes in correlation with changes in myofibril structure and intracellular calcium.,” *Biophys. J.*, vol. 101, pp. 2455–64, Nov. 2011.
- [31] F. R. Heinzel, V. Bito, L. Biesmans, M. Wu, E. Detre, F. von Wegner, P. Claus, S. Dymarkowski, F. Maes, J. Bogaert, F. Rademakers, J. D’hooge, and K. Sipido, “Remodeling of T-tubules and reduced synchrony of Ca²⁺ release in myocytes from chronically ischemic myocardium.,” *Circ. Res.*, vol. 102, pp. 338–46, Feb. 2008.
- [32] W. E. Louch, H. K. Mørk, J. Sexton, T. A. Strømme, P. Laake, I. Sjaastad, and O. M. Sejersted, “T-tubule disorganization and reduced synchrony of Ca²⁺ release in murine cardiomyocytes following myocardial infarction.,” *J. Physiol.*, vol. 574, pp. 519–33, July 2006.
- [33] F. Hohendanner, S. Ljubojević, N. MacQuaide, M. Sacherer, S. Sedej, L. Biesmans, P. Wakula, D. Platzer, S. Sokolow, A. Herchuelz, G. Antoons, K. Sipido, B. Pieske, and F. R. Heinzel, “Intracellular dyssynchrony of diastolic cytosolic [Ca²⁺] decay in ventricular cardiomyocytes in cardiac remodeling and human heart failure.,” *Circ. Res.*, vol. 113, pp. 527–38, Aug. 2013.
- [34] F. J. Huikeshoven, I. D. Hope, G. G. Power, R. D. Gilbert, L. D. Longo, I. D. Hope, L. Linda, and J. Frans, “Mathematical model of fetal circulation and oxygen delivery Mathematical model of fetal circulation and oxygen delivery,” *Am J Physiol Regul. Integr. Comp Physiol*, vol. 249, no. 2 Pt 2, pp. 192–202, 1985.
- [35] Guettouche, A. Guettouche, J. C. Challier, Y. Ito, C. Papapanayotou, Y. Cherruault, and A. Azancot-Benisty, “Mathematical modeling blood circulation of the human fetal arterial,” *Int J Biomed Comput*, vol. 31, no. 2, pp. 127–139, 1992.
- [36] G. Pennati, M. Bellotti, and R. Fumero, “Mathematical modelling of the human foetal cardiovascular system based on Doppler ultrasound data.,” *Med. Eng. Phys.*, vol. 19, pp. 327–35, June 1997.
- [37] E. Ménigault, M. Berson, P. Vieyres, B. Lepoivre, D. Pourcelot, L. Pourcelot, E. Menigault, M. Berson, P. Vieyres, B. Lepoivre, D. Pourcelot, and L. Pourcelot, “Feto-maternal circulation: mathematical model and comparison with Doppler measurements.,” *Eur. J. Ultrasound*, vol. 7, pp. 129–43, Apr. 1998.

- [38] P. M. Sá Couto, W. L. van Meurs, J. a. F. Bernardes, J. P. Marques de Sá, J. a. Goodwin, P. M. S. Couto, W. L. van Meurs, J. a. F. Bernardes, J. P. M. de Sa, and J. a. Goodwin, "Mathematical model for educational simulation of the oxygen delivery to the fetus," *Control Eng. Pract.*, vol. 10, pp. 59–66, Jan. 2002.
- [39] L. J. Myers and W. L. Capper, "A transmission line model of the human foetal circulatory system.," *Med. Eng. Phys.*, vol. 24, pp. 285–94, May 2002.
- [40] J. P. H. M. van den Wijngaard, B. E. Westerhof, D. J. Faber, M. M. Ramsay, N. Westerhof, and M. J. C. van Gemert, "Abnormal arterial flows by a distributed model of the fetal circulation.," *Am. J. Physiol. Regul. Integr. Comp. Physiol.*, vol. 291, pp. R1222–33, Nov. 2006.
- [41] D. NOBLE, "Cardiac action and pacemaker potentials based on the Hodgkin-Huxley equations.," *Nature*, vol. 188, pp. 495–7, Nov. 1960.
- [42] K. H. W. J. ten Tusscher, D. Noble, P. J. Noble, and A. V. Panfilov, "A model for human ventricular tissue.," *Am. J. Physiol. Heart Circ. Physiol.*, vol. 286, pp. H1573–89, Apr. 2004.
- [43] E. J. Crampin, N. P. Smith, A. E. Langham, R. H. Clayton, and C. H. Orchard, "Acidosis in models of cardiac ventricular myocytes.," *Philos. Trans. A. Math. Phys. Eng. Sci.*, vol. 364, pp. 1171–86, May 2006.
- [44] M. Pásek, J. Simurda, and G. Christé, "The functional role of cardiac T-tubules explored in a model of rat ventricular myocytes.," *Philos. Trans. A. Math. Phys. Eng. Sci.*, vol. 364, pp. 1187–206, May 2006.
- [45] A. Hatano, J.-i. Okada, T. Washio, T. Hisada, and S. Sugiura, "A three-dimensional simulation model of cardiomyocyte integrating excitation-contraction coupling and metabolism.," *Biophys. J.*, vol. 101, pp. 2601–10, Dec. 2011.
- [46] R. Ruiz-Baier, A. Gizzi, S. Rossi, C. Cherubini, A. Laadhari, S. Filippi, and A. Quarteroni, "Mathematical modelling of active contraction in isolated cardiomyocytes.," *Math. Med. Biol.*, pp. 1–25, 2013.
- [47] A. Pustoc'h, J. Ohayon, Y. Usson, A. Kamgoue, and P. Tracqui, "An integrative model of the self-sustained oscillating contractions of cardiac myocytes," *Acta Biotheor.*, vol. 53, no. 4, pp. 277–293, 2005.
- [48] E. Gratacos, "Towards an integrated third-trimester screening in pregnancy," *Fetal Diagn Ther.*, vol. 33, no. 3, pp. 141–142, 2013.
- [49] M. Cruz-Lemini, F. Crispi, T. Van Mieghem, D. Pedraza, R. Cruz-Martinez, R. Acosta-Rojas, F. Figueras, M. Parra-Cordero, J. Deprest, and E. Gratacos, "Risk of perinatal death in early-onset intrauterine growth restriction according to gestational age and cardiovascular Doppler indices: a multicenter study," *Fetal Diagn Ther.*, vol. 32, no. 1-2, pp. 116–122, 2012.
- [50] E. Eixarch, E. Meler, a. Iraola, M. Illa, F. Crispi, E. Hernandez-Andrade, E. Gratacos, and F. Figueras, "Neurodevelopmental outcome in 2-year-old infants who were small-for-gestational age term fetuses with cerebral blood flow redistribution," *Ultrasound Obs. Gynecol.*, vol. 32, pp. 894–899, Dec. 2008.
- [51] F. Figueras, R. Cruz-Martinez, M. Sanz-Cortes, A. Arranz, M. Illa, F. Botet, C. Costas-Moragas, and E. Gratacos, "Neurobehavioral outcomes in preterm, growth-restricted infants with and without prenatal advanced signs of brain-sparing," *Ultrasound Obs. Gynecol.*, vol. 38, no. 3, pp. 288–294, 2011.

- [52] J.-C. Fouron, J. Gosselin, M.-J. Raboisson, J. Lamoureux, C.-A. Tison, C. Fouron, and L. Hudon, "The relationship between an aortic isthmus blood flow velocity index and the postnatal neurodevelopmental status of fetuses with placental circulatory insufficiency," *Am. J. Obstet. Gynecol.*, vol. 192, pp. 497–503, Feb. 2005.
- [53] E. Hernandez-Andrade, F. Crispi, J. A. Benavides-Serralde, W. Plasencia, H. F. Diesel, E. Eixarch, R. Acosta-Rojas, F. Figueras, K. Nicolaides, and E. Gratacos, "Contribution of the myocardial performance index and aortic isthmus blood flow index to predicting mortality in preterm growth-restricted fetuses," *Ultrasound Obs. Gynecol.*, vol. 34, no. 4, pp. 430–436, 2009.
- [54] F. Figueras, A. Benavides, M. Del Rio, F. Crispi, E. Eixarch, J. M. Martinez, E. Hernandez-Andrade, E. Gratacós, and E. Gratacos, "Monitoring of fetuses with intrauterine growth restriction: longitudinal changes in ductus venosus and aortic isthmus flow," *Ultrasound Obs. Gynecol.*, vol. 33, pp. 39–43, Jan. 2009.
- [55] K. Makikallio, P. Jouppila, J. Rasanen, K. Mäkikallio, P. Jouppila, and J. Räsänen, "Retrograde net blood flow in the aortic isthmus in relation to human fetal arterial and venous circulations.," *Ultrasound Obstet. Gynecol.*, vol. 19, pp. 147–52, Feb. 2002.
- [56] T. Kiserud, C. Ebbing, J. Kessler, and S. Rasmussen, "Fetal cardiac output, distribution to the placenta and impact of placental compromise," *Ultrasound Obs. Gynecol.*, vol. 28, no. 2, pp. 126–136, 2006.
- [57] P. Bonnin, J. C. Fouron, G. Teyssier, S. E. Sonesson, and A. Skoll, "Quantitative assessment of circulatory changes in the fetal aortic isthmus during progressive increase of resistance to umbilical blood flow," *Circulation*, vol. 88, no. 1, pp. 216–222, 1993.
- [58] J. C. Fouron, G. Teyssier, E. Maroto, M. Lessard, and G. Marquette, "Diastolic circulatory dynamics in the presence of elevated placental resistance and retrograde diastolic flow in the umbilical artery: a Doppler echographic study in lambs," *Am J Obs. Gynecol.*, vol. 164, no. 1 Pt 1, pp. 195–203, 1991.
- [59] J. C. Fouron, A. Skoll, S. E. Sonesson, M. Pfizenmaier, E. Jaeggi, and M. Lessard, "Relationship between flow through the fetal aortic isthmus and cerebral oxygenation during acute placental circulatory insufficiency in ovine fetuses," *Am J Obs. Gynecol.*, vol. 181, no. 5 Pt 1, pp. 1102–1107, 1999.
- [60] P. Garcia-Canadilla, I. Torre, M. Calvo, A. Gonzalez-Tendero, E. Gratacos, and I. Amat-Roldan, "Calibration procedure and characterization of a commercial multiphoton microscope to measure Polarization Second Harmonic Generation microscopy," in *2012 9th IEEE Int. Symp. Biomed. Imaging*, pp. 1296–1299, IEEE, May 2012.
- [61] F. P. Hadlock, R. B. Harrist, Y. P. Shah, D. E. King, S. K. Park, and R. S. Sharman, "Estimating fetal age using multiple parameters: a prospective evaluation in a racially mixed population," *Am J Obs. Gynecol.*, vol. 156, no. 4, pp. 955–957, 1987.
- [62] F. Figueras, E. Meler, A. Iraola, E. Eixarch, O. Coll, J. Figueras, A. Francis, E. Gratacos, and J. Gardosi, "Customized birthweight standards for a Spanish population," *Eur J Obs. Gynecol Reprod Biol.*, vol. 136, no. 1, pp. 20–24, 2008.
- [63] A. A. Baschat and U. Gembruch, "The cerebroplacental Doppler ratio revisited," *Ultrasound Obs. Gynecol.*, vol. 21, no. 2, pp. 124–127, 2003.
- [64] D. Arduini and G. Rizzo, "Normal values of Pulsatility Index from fetal vessels: a cross-sectional study on 1556 healthy fetuses," *J Perinat Med.*, vol. 18, no. 3, pp. 165–172, 1990.

- [65] C. Schneider, B. W. McCrindle, J. S. Carvalho, L. K. Hornberger, K. P. McCarthy, and P. E. F. Daubeney, "Development of Z-scores for fetal cardiac dimensions from echocardiography," *Ultrasound Obs. Gynecol*, vol. 26, pp. 599–605, Nov. 2005.
- [66] V. Milisic and A. Quarteroni, "Analysis of lumped parameter models for blood flow simulations and their relation with 1D models," *Esaim-Mathematical Model. Numer. Anal. Math. Anal. Numer.*, vol. 38, no. 4, pp. 613–632, 2004.
- [67] Y. Shi, P. Lawford, and R. Hose, "Review of zero-D and 1-D models of blood flow in the cardiovascular system.," *Biomed. Eng. Online*, vol. 10, p. 33, Jan. 2011.
- [68] J. Alastruey, K. H. Parker, J. Peiro, S. M. Byrd, S. J. Sherwin, J. Peiró, S. M. Byrd, and S. J. Sherwin, "Modelling the circle of Willis to assess the effects of anatomical variations and occlusions on cerebral flows," *J Biomech*, vol. 40, pp. 1794–1805, Jan. 2007.
- [69] Guettouche, C. Papapanayotou, Y. Cherruault, H. R. Debric, J. C. Challier, A. Guettouche, C. Papapanayotou, Y. Cherruault, A. Azancot-Benisty, and J. C. Challier, "Optimization and resolution algorithm of the human fetal blood circulation model," *Math. Comput. Model.*, vol. 18, no. 9, pp. 1–8, 1993.
- [70] D. Nowak, H. Kozłowska, A. Żurada, and J. Gielecki, "Diameter of the ductus arteriosus as a predictor of patent ductus arteriosus (PDA)," *Cent. Eur. J. Med.*, vol. 6, pp. 418–424, May 2011.
- [71] R. Ruano, M. de Fatima Yukie Maeda, J. I. Niigaki, and M. Zugaib, "Pulmonary artery diameters in healthy fetuses from 19 to 40 weeks' gestation," *J Ultrasound Med*, vol. 26, no. 3, pp. 309–316, 2007.
- [72] M. Szpinda, P. Flisiński, G. Elminowska-Wenda, M. Flisiński, E. Krakowiak-sarnowska, P. Flisinski, G. Elminowska-Wenda, M. Flisinski, and E. Krakowiak-sarnowska, "The variability and morphometry of the brachiocephalic trunk in human foetuses," *Folia Morphol (Warsz)*, vol. 64, no. 4, pp. 309–314, 2005.
- [73] M. Szpinda, A. Szwesta, and E. Szpinda, "Morphometric study of the ductus arteriosus during human development," *Ann Anat*, vol. 189, no. 1, pp. 47–52, 2007.
- [74] M. Szpinda, "The normal growth of the pulmonary trunk in human foetuses," *Folia Morphol (Warsz)*, vol. 66, no. 2, pp. 126–130, 2007.
- [75] M. Szpinda, "The normal growth of the thoracic aorta in human foetuses," *Folia Morphol (Warsz)*, vol. 66, no. 2, pp. 131–137, 2007.
- [76] M. Szpinda, P. Flisinski, M. Wisniewski, M. Dombek, and E. Krakowiak-Sarnowska, "Digital-image analysis of the left common carotid artery in human foetuses," *Folia Morphol (Warsz)*, vol. 67, no. 3, pp. 186–192, 2008.
- [77] M. Szpinda, P. Flisinski, A. Szwesta, M. Wisniewski, M. Dombek, and E. Krakowiak-Sarnowska, "Quantitative morphology of the left subclavian artery in human fetuses," *Adv Med Sci*, vol. 53, no. 1, pp. 69–75, 2008.
- [78] M. Szpinda, "Length growth of the various aortic segments in human foetuses," *Folia Morphol (Warsz)*, vol. 67, no. 4, pp. 245–250, 2008.
- [79] M. Szpinda, A. Szpinda, A. Wozniak, C. Mila-Kierzenkowska, A. Kosinski, and M. Grzybiak, "Quantitative anatomy of the growing abdominal aorta in human fetuses: an anatomical, digital and statistical study," *Med Sci Monit*, vol. 18, no. 10, pp. BR419–26, 2012.
- [80] P. C. Struijk, V. J. Mathews, T. Loupas, P. A. Stewart, E. B. Clark, E. A. Steegers, and J. W. Wladimiroff, "Blood pressure estimation in the human fetal descending aorta," *Ultrasound Obs. Gynecol*, vol. 32, no. 5, pp. 673–681, 2008.

- [81] T. Kiserud, "Physiology of the fetal circulation.," *Semin. Fetal Neonatal Med.*, vol. 10, pp. 493–503, Dec. 2005.
- [82] M. Seed, J. F. P. van Amerom, S.-J. Yoo, B. Al Nafisi, L. Grosse-Wortmann, E. Jaeggi, M. S. Jansz, and C. K. Macgowan, "Feasibility of quantification of the distribution of blood flow in the normal human fetal circulation using CMR: a cross-sectional study.," *J. Cardiovasc. Magn. Reson.*, vol. 14, p. 79, Jan. 2012.
- [83] G. Pennati and R. Fumero, "Scaling approach to study the changes through the gestation of human fetal cardiac and circulatory behaviors," *Ann Biomed Eng*, vol. 28, no. 4, pp. 442–452, 2000.
- [84] S. Gallivan, S. C. Robson, T. C. Chang, J. Vaughan, and J. A. Spencer, "An investigation of fetal growth using serial ultrasound data," *Ultrasound Obs. Gynecol*, vol. 3, no. 2, pp. 109–114, 1993.
- [85] R. Cruz-Martinez, F. Figueras, a. Benavides-Serralde, F. Crispi, E. Hernandez-Andrade, and E. Gratacos, "Sequence of changes in myocardial performance index in relation to aortic isthmus and ductus venosus Doppler in fetuses with early-onset intrauterine growth restriction.," *Ultrasound Obstet. Gynecol.*, vol. 38, pp. 179–84, Aug. 2011.
- [86] K. L. Reed, C. F. Anderson, and L. Shenker, "Changes in intracardiac Doppler blood flow velocities in fetuses with absent umbilical artery diastolic flow," *Am J Obs. Gynecol*, vol. 157, no. 3, pp. 774–779, 1987.
- [87] Z. Weiner, G. Farmakides, H. Schulman, and B. Penny, "Central and peripheral hemodynamic changes in fetuses with absent end-diastolic velocity in umbilical artery: correlation with computerized fetal heart rate pattern," *Am J Obs. Gynecol*, vol. 170, no. 2, pp. 509–515, 1994.
- [88] T. Akalin-Sel, K. H. Nicolaides, J. Peacock, and S. Campbell, "Doppler dynamics and their complex interrelation with fetal oxygen pressure, carbon dioxide pressure, and pH in growth-retarded fetuses," *Obs. Gynecol*, vol. 84, no. 3, pp. 439–444, 1994.
- [89] K. G. Schmidt, N. H. Silverman, and A. M. Rudolph, "Phasic flow events at the aortic isthmus-ductus arteriosus junction and branch pulmonary artery evaluated by multimodal ultrasonography in fetal lambs," *Am J Obs. Gynecol*, vol. 179, no. 5, pp. 1338–1347, 1998.
- [90] X. De Muylder, J. C. Fouron, H. Bard, L. Riopel, and F. Urfer, "The difference between the systolic time intervals of the left and right ventricles during fetal life," *Am J Obs. Gynecol*, vol. 149, no. 7, pp. 737–740, 1984.
- [91] J. Chabaneix, J. C. Fouron, A. Sosa-Olavarria, R. Gendron, N. Dahdah, A. Berger, and S. Brisebois, "Profiling left and right ventricular proportional output during fetal life with a novel systolic index in the aortic isthmus," *Ultrasound Obs. Gynecol*, vol. 44, no. 2, pp. 176–181, 2014.
- [92] G. Acharya, "Technical aspects of aortic isthmus Doppler velocimetry in human fetuses.," *Ultrasound Obstet. Gynecol.*, vol. 33, pp. 628–33, June 2009.
- [93] M. V. Machado, S. C. Chita, and L. D. Allan, "Acceleration time in the aorta and pulmonary artery measured by Doppler echocardiography in the midtrimester normal human fetus," *Br Hear. J*, vol. 58, no. 1, pp. 15–18, 1987.
- [94] M. S. Sutton, T. Gill, T. Plappert, D. H. Saltzman, and P. Doubilet, "Assessment of right and left ventricular function in terms of force development with gestational age in the normal human fetus," *Br Hear. J*, vol. 66, no. 4, pp. 285–289, 1991.

- [95] F. S. Molina, C. Faro, A. Sotiriadis, T. Dagklis, and K. H. Nicolaides, "Heart stroke volume and cardiac output by four-dimensional ultrasound in normal fetuses," *Ultrasound Obs. Gynecol.*, vol. 32, no. 2, pp. 181–187, 2008.
- [96] T. Kiserud and G. Acharya, "The fetal circulation.," *Prenat. Diagn.*, vol. 24, pp. 1049–59, Dec. 2004.
- [97] P. Garcia-Canadilla, P. A. Rudenick, F. Crispi, M. Cruz-Lemini, G. Palau, O. Camara, E. Gratacos, and B. H. Bijens, "A computational model of the fetal circulation to quantify blood redistribution in intrauterine growth restriction," *PLoS Comput Biol.*, vol. 10, no. 6, p. e1003667, 2014.
- [98] O. Luria, J. Bar, M. Kovo, G. Malinger, A. Golan, and O. Barnea, "The role of blood flow distribution in the regulation of cerebral oxygen availability in fetal growth restriction.," *Med. Eng. Phys.*, vol. 34, pp. 364–9, Apr. 2012.
- [99] O. Luria, J. Bar, J. Shalev, M. Kovo, A. Golan, and O. Barnea, "Inverse Solution of the Fetal-Circulation Model Based on Ultrasound Doppler Measurements," *Cardiovasc. Eng. Technol.*, vol. 5, no. 2, pp. 202–216, 2014.
- [100] J. P. H. M. van den Wijngaard, B. E. Westerhof, M. G. Ross, and M. J. C. van Gemert, "A mathematical model of twin-twin transfusion syndrome with pulsatile arterial circulations.," *Am. J. Physiol. Regul. Integr. Comp. Physiol.*, vol. 292, pp. R1519–31, Apr. 2007.
- [101] M. J. C. van Gemert, H. J. Sterenborg, and M. J. C. V. G. C., "Haemodynamic Model of Twin-Twin Transfusion Syndrome," *Placenta*, vol. 19, no. 2-3, pp. 195–208, 1998.
- [102] R. Ponzini, C. Vergara, G. Rizzo, A. Veneziani, A. Roghi, A. Vanzulli, O. Parodi, and A. Redaelli, "Womersley number-based estimates of blood flow rate in Doppler analysis: in vivo validation by means of phase-contrast MRI," *IEEE Trans Biomed Eng.*, vol. 57, no. 7, pp. 1807–1815, 2010.
- [103] G. R. DeVore, "Assessing fetal cardiac ventricular function.," *Semin Fetal Neonatal Med.*, vol. 10, pp. 515–41, Dec. 2005.
- [104] F. Figueras and E. Gratacós, "Update on the diagnosis and classification of fetal growth restriction and proposal of a stage-based management protocol.," *Fetal Diagn. Ther.*, vol. 36, pp. 86–98, Jan. 2014.
- [105] M. Parra-Saavedra, F. Crovetto, S. Triunfo, S. Savchev, A. Peguero, A. Nadal, G. Parra, E. Gratacos, and F. Figueras, "Neurodevelopmental outcomes of near-term small-for-gestational-age infants with and without signs of placental underperfusion.," *Placenta*, vol. 35, pp. 269–74, Apr. 2014.
- [106] M. Parra-Saavedra, F. Crovetto, S. Triunfo, S. Savchev, A. Peguero, A. Nadal, G. Parra, E. Gratacos, and F. Figueras, "Placental findings in late-onset SGA births without Doppler signs of placental insufficiency.," *Placenta*, vol. 34, pp. 1136–41, Dec. 2013.
- [107] M. Parra-Saavedra, F. Crovetto, S. Triunfo, S. Savchev, A. Peguero, A. Nadal, E. Gratacós, and F. Figueras, "Association of Doppler parameters with placental signs of underperfusion in late-onset small-for-gestational-age pregnancies.," *Ultrasound Obstet. Gynecol.*, vol. 44, pp. 330–7, Sept. 2014.
- [108] M. Parra-Saavedra, S. Simeone, S. Triunfo, F. Crovetto, F. Botet, A. Nadal, E. Gratacos, and F. Figueras, "Correlation between histological signs of placental underperfusion and perinatal morbidity in late-onset small-for-gestational-age fetuses.," *Ultrasound Obstet. Gynecol.*, vol. 45, pp. 149–55, Mar. 2015.

- [109] H. van Huisseling, T. H. Hasaart, G. J. Muijsers, and J. de Haan, "Umbilical artery pulsatility index and placental vascular resistance during acute hypoxemia in fetal lambs.," *Gynecol. Obstet. Invest.*, vol. 31, pp. 61–6, Jan. 1991.
- [110] S. L. Adamson, "Arterial pressure, vascular input impedance, and resistance as determinants of pulsatile blood flow in the umbilical artery," *Eur J Obs. Gynecol Reprod Biol*, vol. 84, no. 2, pp. 119–125, 1999.
- [111] D. R. Surat and S. L. Adamson, "Downstream determinants of pulsatility of the mean velocity waveform in the umbilical artery as predicted by a computer model," *Ultrasound Med Biol*, vol. 22, no. 6, pp. 707–717, 1996.
- [112] H. M. Saunders, P. N. Burns, L. Needleman, J. B. Liu, R. Boston, J. A. Wortman, and L. Chan, "Hemodynamic factors affecting uterine artery Doppler waveform pulsatility in sheep.," *J. Ultrasound Med.*, vol. 17, pp. 357–68, June 1998.
- [113] S. L. Adamson, R. J. Morrow, P. A. Bascom, L. Y. Mo, and J. W. Ritchie, "Effect of placental resistance, arterial diameter, and blood pressure on the uterine arterial velocity waveform: a computer modeling approach.," *Ultrasound Med. Biol.*, vol. 15, pp. 437–42, Jan. 1989.
- [114] R. S. Thompson and B. J. Trudinger, "Doppler waveform pulsatility index and resistance, pressure and flow in the umbilical placental circulation: an investigation using a mathematical model," *Ultrasound Med Biol*, vol. 16, no. 5, pp. 449–458, 1990.
- [115] L. Y. Mo, P. A. Bascom, K. Ritchie, and L. M. McCowan, "A transmission line modelling approach to the interpretation of uterine Doppler waveforms.," *Ultrasound Med. Biol.*, vol. 14, pp. 365–76, Jan. 1988.
- [116] T. R. Everett and C. C. Lees, "Beyond the placental bed: placental and systemic determinants of the uterine artery Doppler waveform.," *Placenta*, vol. 33, pp. 893–901, Nov. 2012.
- [117] B. Almog, F. Shehata, S. Aljabri, I. Levin, E. Shalom-Paz, and A. Shrim, "Placenta weight percentile curves for singleton and twins deliveries.," *Placenta*, vol. 32, pp. 58–62, Jan. 2011.
- [118] T. Burkhardt, L. Schäffer, C. Schneider, R. Zimmermann, and J. Kurmanavicius, "Reference values for the weight of freshly delivered term placentas and for placental weight-birth weight ratios.," *Eur. J. Obstet. Gynecol. Reprod. Biol.*, vol. 128, pp. 248–52, Jan. 2006.
- [119] R. W. Redline, D. Heller, S. Keating, and J. Kingdom, "Placental diagnostic criteria and clinical correlation—a workshop report.," *Placenta*, vol. 26 Suppl A, pp. S114–7, Apr. 2005.
- [120] R. W. Redline, "Placental pathology: a systematic approach with clinical correlations.," *Placenta*, vol. 29 Suppl A, pp. S86–91, Mar. 2008.
- [121] S. Triunfo, S. Lobmaier, M. Parra-Saavedra, F. Crovetto, A. Peguero, A. Nadal, E. Gratacos, and F. Figueras, "Angiogenic factors at diagnosis of late-onset small-for-gestational age and histological placental underperfusion.," *Placenta*, vol. 35, pp. 398–403, June 2014.
- [122] P. Rudenick, B. Bijnens, C. Butakoff, D. Garcia-Dorado, and A. Evangelista, "Understanding Hemodynamics and Its Determinant Factors in Type B Aortic Dissections Using an Equivalent Lumped Model," in *STACOM, Proc. Int. Conf. Med. Image Comput. Assist. Interv. LNCS vol. 7746*, vol. 2, pp. 375–382, 2013.
- [123] R. Madazli, A. Somunkiran, Z. Calay, S. Ilvan, and M. F. Aksu, "Histomorphology of the placenta and the placental bed of growth restricted fetuses and correlation with

- the Doppler velocimetries of the uterine and umbilical arteries,” *Placenta*, vol. 24, no. 5, pp. 510–516, 2003.
- [124] S. Zhang, T. R. H. Regnault, P. L. Barker, K. J. Botting, I. C. McMillen, C. M. McMillan, C. T. Roberts, and J. L. Morrison, “Placental adaptations in growth restriction,” *Nutrients*, vol. 7, pp. 360–89, Jan. 2015.
- [125] C. G. Bonnemann and N. G. Laing, “Myopathies resulting from mutations in sarcomeric proteins,” *Curr Opin Neurol*, vol. 17, no. 5, pp. 529–537, 2004.
- [126] Y. Cheng, X. Wan, T. A. McElfresh, X. Chen, K. S. Gresham, D. S. Rosenbaum, M. P. Chandler, and J. E. Stelzer, “Impaired contractile function due to decreased cardiac myosin binding protein C content in the sarcomere,” *Am J Physiol Hear. Circ Physiol*, vol. 305, no. 1, pp. H52–65, 2013.
- [127] J. R. Patel, J. M. Pleitner, R. L. Moss, and M. L. Greaser, “Magnitude of length-dependent changes in contractile properties varies with titin isoform in rat ventricles,” *Am J Physiol Hear. Circ Physiol*, vol. 302, no. 3, pp. H697–708, 2012.
- [128] N. Fukuda, D. Sasaki, S. Ishiwata, and S. Kurihara, “Length dependence of tension generation in rat skinned cardiac muscle: role of titin in the Frank-Starling mechanism of the heart,” *Circulation*, vol. 104, no. 14, pp. 1639–1645, 2001.
- [129] T. Boulesteix, E. Beaurepaire, M. P. Sauviat, and M. C. Schanne-Klein, “Second-harmonic microscopy of unstained living cardiac myocytes: measurements of sarcomere length with 20-nm accuracy,” *Opt Lett*, vol. 29, no. 17, pp. 2031–2033, 2004.
- [130] G. Bub, P. Camelliti, C. Bollensdorff, D. J. Stuckey, G. Picton, R. A. Burton, K. Clarke, and P. Kohl, “Measurement and analysis of sarcomere length in rat cardiomyocytes in situ and in vitro,” *Am J Physiol Hear. Circ Physiol*, vol. 298, no. 5, pp. H1616–25, 2010.
- [131] P. Campagnola, “Second harmonic generation imaging microscopy: applications to diseases diagnostics,” *Anal Chem*, vol. 83, no. 9, pp. 3224–3231, 2011.
- [132] P. J. Campagnola, H. A. Clark, W. A. Mohler, A. Lewis, and L. M. Loew, “Second-harmonic imaging microscopy of living cells,” *J Biomed Opt*, vol. 6, no. 3, pp. 277–286, 2001.
- [133] P. J. Campagnola, A. C. Millard, M. Terasaki, P. E. Hoppe, C. J. Malone, and W. A. Mohler, “Three-dimensional high-resolution second-harmonic generation imaging of endogenous structural proteins in biological tissues,” *Biophys J*, vol. 82, no. 1 Pt 1, pp. 493–508, 2002.
- [134] C. Odin, T. Guilbert, A. Alkilani, O. P. Boryskina, V. Fleury, and Y. Le Grand, “Collagen and myosin characterization by orientation field second harmonic microscopy,” *Opt Express*, vol. 16, no. 20, pp. 16151–16165, 2008.
- [135] S. J. Wallace, J. L. Morrison, K. J. Botting, and T. W. Kee, “Second-harmonic generation and two-photon-excited autofluorescence microscopy of cardiomyocytes: quantification of cell volume and myosin filaments,” *J Biomed Opt*, vol. 13, no. 6, p. 64018, 2008.
- [136] M. Both, M. Vogel, O. Friedrich, F. von Wegner, T. Kunsting, R. H. Fink, and D. Uttenweiler, “Second harmonic imaging of intrinsic signals in muscle fibers in situ,” *J Biomed Opt*, vol. 9, no. 5, pp. 882–892, 2004.
- [137] S. V. Plotnikov, A. C. Millard, P. J. Campagnola, and W. A. Mohler, “Characterization of the myosin-based source for second-harmonic generation from muscle sarcomeres,” *Biophys J*, vol. 90, no. 2, pp. 693–703, 2006.

- [138] H. Bao, A. Boussioutas, R. Jeremy, S. Russell, and M. Gu, "Second harmonic generation imaging via nonlinear endomicroscopy," *Opt. Express*, vol. 18, no. 2, pp. 1255–1260, 2010.
- [139] L. Fu and M. Gu, "Polarization anisotropy in fiber-optic second harmonic generation microscopy," *Opt. Express*, vol. 16, no. 7, pp. 5000–5006, 2008.
- [140] M. E. Llewellyn, R. P. J. Barretto, S. L. Delp, and M. J. Schnitzer, "Minimally invasive high-speed imaging of sarcomere contractile dynamics in mice and humans," *Nature*, vol. 454, no. 7205, pp. 784–788, 2008.
- [141] E. U. Rafailov, M. A. Cataluna, and W. Sibbett, "Mode-locked quantum-dot lasers," *Nat. Photonics*, vol. 1, no. 7, pp. 395–401, 2007.
- [142] R. A. Rao, M. R. Mehta, and K. C. Toussaint Jr., "Fourier transform-second-harmonic generation imaging of biological tissues," *Opt Express*, vol. 17, no. 17, pp. 14534–14542, 2009.
- [143] M. Sivaguru, S. Durgam, R. Ambekar, D. Luedtke, G. Fried, A. Stewart, and K. C. Toussaint Jr., "Quantitative analysis of collagen fiber organization in injured tendons using Fourier transform-second harmonic generation imaging," *Opt Express*, vol. 18, no. 24, pp. 24983–24993, 2010.
- [144] V. Nucciotti, C. Stringari, L. Sacconi, F. Vanzi, L. Fusi, M. Linari, G. Piazzesi, V. Lombardi, and F. S. Pavone, "Probing myosin structural conformation in vivo by second-harmonic generation microscopy," *Proc Natl Acad Sci U S A*, vol. 107, no. 17, pp. 7763–7768, 2010.
- [145] H. Liu, Y. Shao, W. Qin, R. B. Runyan, M. Xu, Z. Ma, T. K. Borg, R. Markwald, and B. Z. Gao, "Myosin filament assembly onto myofibrils in live neonatal cardiomyocytes observed by TPEF-SHG microscopy," *Cardiovasc Res*, vol. 97, no. 2, pp. 262–270, 2013.
- [146] G. Recher, D. Rouede, P. Richard, A. Simon, J. J. Bellanger, and F. Tiaho, "Three distinct sarcomeric patterns of skeletal muscle revealed by SHG and TPEF microscopy," *Opt Express*, vol. 17, no. 22, pp. 19763–19777, 2009.
- [147] C. S. Garbe, A. Buttgerit, S. Schurmann, and O. Friedrich, "Automated multiscale morphometry of muscle disease from second harmonic generation microscopy using tensor-based image processing," *IEEE Trans Biomed Eng*, vol. 59, no. 1, pp. 39–44, 2012.
- [148] S. V. Plotnikov, A. M. Kenny, S. J. Walsh, B. Zubrowski, C. Joseph, V. L. Scranton, G. A. Kuchel, D. Dauser, M. Xu, C. C. Pilbeam, D. J. Adams, R. P. Dougherty, P. J. Campagnola, and W. A. Mohler, "Measurement of muscle disease by quantitative second-harmonic generation imaging," *J Biomed Opt*, vol. 13, no. 4, p. 44018, 2008.
- [149] S. Psilodimitrakopoulos, D. Artigas, G. Soria, I. Amat-Roldan, A. M. Planas, and P. Loza-Alvarez, "Quantitative discrimination between endogenous SHG sources in mammalian tissue, based on their polarization response," *Opt Express*, vol. 17, no. 12, pp. 10168–10176, 2009.
- [150] F. R. Heinzel, V. Bito, P. G. A. Volders, G. Antoons, K. Mubagwa, and K. R. Sipido, "Spatial and temporal inhomogeneities during Ca²⁺ release from the sarcoplasmic reticulum in pig ventricular myocytes," *Circ. Res.*, vol. 91, pp. 1023–30, Nov. 2002.
- [151] T. G. Kuznetsova, M. N. Starodubtseva, N. I. Yegorenkov, S. A. Chizhik, and R. I. Zhdanov, "Atomic force microscopy probing of cell elasticity," *Micron*, vol. 38, pp. 824–33, Jan. 2007.

- [152] A. B. Mathur, A. M. Collinsworth, W. M. Reichert, W. E. Kraus, and G. A. Truskey, "Endothelial, cardiac muscle and skeletal muscle exhibit different viscous and elastic properties as determined by atomic force microscopy," *J. Biomech.*, vol. 34, pp. 1545–53, Dec. 2001.
- [153] S. C. Lieber, N. Aubry, J. Pain, G. Diaz, S.-J. Kim, and S. F. Vatner, "Aging increases stiffness of cardiac myocytes measured by atomic force microscopy nanoindentation," *Am. J. Physiol. Heart Circ. Physiol.*, vol. 287, pp. H645–51, Aug. 2004.
- [154] U. G. Hofmann, C. Rotsch, W. J. Parak, and M. Radmacher, "Investigating the cytoskeleton of chicken cardiocytes with the atomic force microscope," *J. Struct. Biol.*, vol. 119, pp. 84–91, July 1997.
- [155] S. G. Shroff, D. R. Saner, and R. Lal, "Dynamic micromechanical properties of cultured rat atrial myocytes measured by atomic force microscopy," *Am. J. Physiol.*, vol. 269, pp. C286–92, July 1995.
- [156] C. Geuzaine and J.-F. Remacle, "Gmsh: A 3-D finite element mesh generator with built-in pre- and post-processing facilities," *Int. J. Numer. Methods Eng.*, vol. 79, no. 11, pp. 1309–1331, 2009.
- [157] R. Cimrman, "{SfePy} - Write Your Own {FE} Application," in *Proc. 6th Eur. Conf. Python Sci. (EuroSciPy 2013)* (P. de Buyl and N. Varoquaux, eds.), pp. 65–70, 2014.
- [158] P. Tracqui and J. Ohayon, "Multiphysic Modelling of the Self-sustained Anisotropic Contraction of Cardiac Myocytes," no. 1, pp. 1–4, 2007.
- [159] P. Tracqui, J. Ohayon, and T. Boudou, "Theoretical analysis of the adaptive contractile behaviour of a single cardiomyocyte cultured on elastic substrates with varying stiffness," *J. Theor. Biol.*, vol. 255, no. 1, pp. 92–105, 2008.
- [160] P. Tracqui and J. Ohayon, "An integrated formulation of anisotropic force-calcium relations driving spatio-temporal contractions of cardiac myocytes," *Philos. Trans. A. Math. Phys. Eng. Sci.*, vol. 367, no. 1908, pp. 4887–4905, 2009.
- [161] T. Ohashi, Y. Ishii, Y. Ishikawa, T. Matsumoto, and M. Sato, "Experimental and numerical analyses of local mechanical properties measured by atomic force microscopy for sheared endothelial cells," *Biomed. Mater. Eng.*, vol. 12, pp. 319–27, Jan. 2002.
- [162] A. J. Brady, "Mechanical properties of isolated cardiac myocytes," *Physiol. Rev.*, vol. 71, pp. 413–28, Apr. 1991.

Publications

Journal papers

1. **Garcia-Canadilla P**, Rodriguez JF, Palazzi MJ, Schonleitner P, Balicevic V, Loncaric S, Antoons G, Cripi F, Gratacos E, Bijmens B. *A two dimensional electromechanical model of a cardiomyocyte to assess intra-cellular regional mechanical heterogeneities*. [In preparation]
2. **Garcia-Canadilla P**, Crispi F, Cruz-Lemini M, Triumfo S, Nadal A, Valenzuela-Alcaraz B, Rudenick PA, Gratacos E, Bijmens BH. *Patient-specific estimates of vascular and placental properties in growth-restricted fetuses based on a model of the fetal circulation*. [Under review]
3. **Garcia-Canadilla P**, Crispi F, Cruz-Lemini M, Valenzuela-Alcaraz B, Rudenick PA, Gratacos E, Bijmens B. *Understanding the aortic isthmus Doppler profile, and its changes with gestational age, using a lumped model of the fetal circulation*. [Under review]
4. Torre I, Gonzalez-Tendero A, **Garcia-Canadilla P**, Crispi F, Garcia-Garcia F, Bijmens B, Iruretagoyena I, Dopazo J, Amat-Roldan I, Gratacós E. *Permanent Cardiac Sarcomere Changes in a Rabbit Model of Intrauterine Growth Restriction* PLoS One,9(11):e113067, 2014.
5. **Garcia-Canadilla P**, Rudenick PA, Crispi F, Cruz-Lemini M, Palau G, Camara O, Gratacos E, Bijens BH. *A computational model of the fetal circulation to quantify blood redistribution in intrauterine growth restriction*. PLoS Computational Biology, 10(6):e1003667, 2014.
6. **Garcia-Canadilla P**, Gonzalez-Tendero A, Iruretagoyena I, Crispi F, Torre I, Amat-Roldan I, Bijmens BH, Gratacos E. *Automated cardiac sarcomere analysis from second harmonic generation images*. Journal of Biomedical Optics, 19(5):056010, 2014.

7. Iruretagoyena JI, Gonzalez-Tendero A, **Garcia-Canadilla P**, Amat-Roldan I, Torre I, Nadal A, Crispi F, Gratacos E. *Cardiac dysfunction is associated with altered sarcomere ultrastructure in intrauterine growth restriction*. American Journal of Obstetrics and Gynecology, 210(6):550.e1-7, 2014.
8. Gonzalez-Tendero A, Torre I, **Garcia-Canadilla P**, Crispi F, García-García F, Dopazo J, Bijmens B, Gratacós E. *Intrauterine growth restriction is associated with cardiac ultrastructural and gene expression changes related to the energetic metabolism in a rabbit model*. American Journal of Physiology Heart and Circulatory Physiology, 305(12):H1752-60, 2013.

Conference papers

1. **Garcia-Canadilla P**, Rudenick PA, Crispi F, Cruz-Lemini M, Palau G, Gratacos E, Bijmens BB. *Understanding prenatal brain sparing by flow redistribution based on a lumped model of the fetal circulation*. Functional Imaging and Modeling of the Heart (FIMH), London, UK, 2013.
2. **Garcia-Canadilla P**, Torre I, Calvo M, Gonzalez-Tendero A, Gratacos E, Amat-Roldan I. *Calibration procedure and characterization of a commercial multiphoton microscope to measure Polarization Second Harmonic Generation microscopy*. International Symposium on Biomedical Imaging (ISBI), Barcelona, Spain, 2012.
3. **Garcia-Canadilla P**, Torre I, Gonzalez-Tendero A, Iruretagoyena I, Eixarch E, Crispi F, Gratacos E, Amat-Roldan I. *Automated morphometric characterization of cardiac fibers by second harmonic microscopy imaging*. International Symposium on Biomedical Imaging (ISBI), Chicago, USA, 2011.

Conference abstracts

1. **Garcia-Canadilla P**, Gonzalez-Tendero A, Schonleitner P, Balicevic V, Loncaric S, Palazzi MJ, Antoons G, Cripi F, Gratacos E, Bijmens B. *Two-dimensional mechanical model of a cardiomyocyte to assess the local inhomogeneities within the cell*. IV International Conference on Computational Bioengineering, Barcelona, Spain, 2015.
2. **Garcia-Canadilla P**, Gonzalez-Tendero A, Schonleitner P, Balicevic V, Palazzi MJ, Rodriguez JF, Antoons G, Cripi F, Camara O, Loncaric S, Gratacos E, Bijmens B. *Two-dimensional mechanical model*

of a cardiomyocyte to assess the local inhomogeneities within the cell. Cardiac Physiome, Auckland, New Zealand, 2015.

3. **Garcia-Canadilla P**, Crispi F, Rudenick PA, Cruz-Lemini M, Palau-Caballero P, Camara O, Gratacos E, Bijmens B. *Quantification of placental/brain vascular resistance and compliance in IUGR using a computational model of the fetal circulation.* 24th World Congress on Ultrasound in Obstetrics and Gynecology, Barcelona, Spain, 2014.
4. Crispi F, **Garcia-Canadilla P**, Rudenick PA, Cruz-Lemini M, Palau-Caballero P, Bijmens B, Gratacos E. *A computational model of the fetal circulation to better understand aortic isthmus flow changes in intrauterine growth restriction.* 12th World Congress in Fetal Medicine, Marbella, Spain, 2013.
5. Torre I, Gonzalez-Tendero A, Wojtas B, Amat-Roldan I, Llach A, **Garcia-Canadilla P**, Crispi F, Hove-Madsen L, Gratacos E. *Initiation of relaxation is delayed in fetal ventricular myocytes from rabbits suffering intrauterine growth restriction and worsen postnatally.* Frontiers in cardiovascular Biology, London, UK, 2012.
6. Torre I, Gonzalez-Tendero A, **Garcia-Canadilla P**, Crispi F, Garcia-Garcia F, Iruretagoyena I, Dopazo J, Amat-Roldan I, Gratacos E. *Sarcomere permanent morphometric changes underlie cardiac programming in intrauterine growth restriction.* Frontiers in cardiovascular Biology, London, UK, 2012.
7. Perez-Moreno A, **Garcia-Canadilla P**, Dominguez JM, Crispi F, Gratacos E, Amat-Roldan I. *Changes in B-mode Ultrasound invariant image features correlate with histological changes in an atherosclerotic rabbit model.* Frontiers in cardiovascular Biology, London, UK, 2012.
8. Iruretagoyena I, Torre I, Amat-Roldan I, Psilodimitrakopoulo S, Crispi F, **Garcia-Canadilla P**, Gonzalez-Tendero A, Nada A, Eixarch E, Loza-Alvare P, Artigas D, Gratacos E. *Ultrastructural analysis of myocardiocyte sarcomeric changes in relation with cardiac dysfunction in human fetuses with intrauterine growth restriction.* 31st Annual Meeting of Society for Maternal-fetal Medicine, San Francisco, USA, 2011.
9. Illa M, Iruretagoy I, Eixarch E, Torre I, Amat-Roldan I, **Garcia - Canadilla P**, Crispi F, Figueras F, Gratacos E. *Ultrastructural analysis of the sarcomere in relation with cardiac dysfunction in a rabbit*

model of intrauterine growth restriction. 20th International Conference on Ultrasound in Obstetrics and Gynecology, Prague, Czech Republic, 2010.

Acknowledgements

I would like to express my gratitude to all those that, in one way or another, have made the completion of this thesis possible.

First of all, I would like to give special thanks to my thesis supervisors, for all they have taught me over the last few years, that it has been much, their patience and enthusiasm in carrying out this ambitious project, and challenging me everyday to improve myself both personally and professionally.

To Eduard, for giving me the opportunity to be part of such wonderful and leader research group in fetal medicine, teaching us spirit of daily overcoming. To Fatima, for her patience and large amount of hours dedicated to teach me everything about fetal cardiology, her illusion and enthusiasm for this project, and for trusting me. To Bart, for teaching me one of the key phrases of this thesis: *”’t leven is lasting”*, for giving me the opportunity of joining the dark side, and leaving me free to learn and do it my own way but, at the same time, giving me all the support necessary.

Special thanks to all co-authors of this thesis, for their excellent work, their help, and because their collaboration have been essential for the completion of this thesis.

Voldria agrair també a tota la gent del grup de medicina fetal i perinatal, tant els que encara hi són, com els que en algun moment van formar part d’ell, per haver-me acompanyat durant aquest llarg camí des dels meus inicis com a projectista. Voldria però fer una menció especial a dues persones que s’han convertit en molt més que unes companyes de recerca: l’Anna i l’Ariadna. Gràcies per tota la vostra paciència en els moments més difícils, per ajudar-me a créixer com a persona, escoltar-me i ensenyar-me moltíssimes coses, tant de biologia com de la vida. Per tots els moments a la vostra vora i els que queden!

Als meus companys de la UPF, per deixar-me formar part d’un grup de gent tant alegre, entusiasta i ”dark”, amb els que he compartit molt bons moments, tant dins com fora de la feina, i espero poder seguir compartint molts més.

Vorrei anche ringraziare tutte le persone del LaBs (Politecno di Mi-

lano), per avermi fatto sentire come a casa durante questi tre mesi, per l'insegnamento non solo di italiano, ma descobrirme anche altre cose come il vero cibo italiano, il negroni e l'aperitivo. Un ringraziamento speciale a Jose Felix, per tutto quello che ho imparato al suo fianco, le ore dedicate e gli sforzi, e per avermi accettato qui in LaBS.

A tots els meus amics del poliesportiu UPC, per tots els body attacks, combats, pumps, balances i body birres dels divendres que hem compartit junts. Us heu convertit en la meva segona família, i sense vosaltres i els nostres moments de desconnexió i rialles, no solament practicant esport sinó també fent Aniol-calçotades, excursions, jugant a màgic... hagués estat molt més dur del que ha estat. A la Roser, perquè t'has convertit en un persona molt important en la meva vida, que sempre has estat allà, i si avui he arribat fins aquí en gran mesura és gràcies a tu. A en Sergi i la Marta, que malgrat la distància, el vostre suport ha estat molt important també.

A mis padres, por su apoyo incondicional, por creer en lo que hago aunque no seais capaces de entenderlo, por haberme animado siempre a seguir luchando y darme fuerzas en los momentos más difíciles y sobretodo enseñarme a sacar siempre lo mejor de mi. A mi hermano Iván, por soportar mis explicaciones sobre mi trabajo y no dormirse, por sacarme siempre unas carcajadas en los momentos más duros, y por creer en mi. A mi tata Flori y mis primos. A mi tío Manolo, un beso al cielo.

A tu Gerard, per rebre'm cada dia amb un somriure i donar-li sempre un toc de color als dies més grisos, per ser-hi sempre al meu costat, tant en els bons com en els moments dolents, animar-me a continuar lluitant, a buscar solucions i no lamentar-me. Sense tu, el teu suport, el teu amor, el teu optimisme simplement hagués estat impossible arribar al dia d'avui. Simplement per ser com ets i perquè t'estimo. Gràcies!

Barcelona, 2015

Curriculum Vitae

Patricia Garcia-Cañadilla was born on July 9, 1985 in Rubí, Barcelona, Spain. She grew up in the same city of the Barcelona state. After attending primary school at Escola Montserrat (1989–2001) and high school at IES La Serreta (2001–2003), she went on to study at the Universitat Politècnica de Catalunya. In 2010, she obtained a BSc degree in Telecommunication Engineering. Her BSc thesis project, carried out at Fetal i+D: Fetal and Prenatal Medicine



Research Group, from Hospital Clinic in Barcelona, under the supervision of Dr. Ivan Amat-Roldan and Prof. Ferran Marqués, was about developing image processing tools to automatically quantify microscopy images from cardiac tissue samples. It was the starting point of her biomedical career. In 2011, she obtained a MSc degree in Biomedicine from Universitat de Barcelona. Her MSc thesis was about improving the tool implemented for the BSc thesis, by adding new functionalities that allow the characterization of new morphometric features from microscopy cardiac tissue images. After graduation, she started her PhD studies under the supervision of Dr. Bart Bijnens, Dra. Fàtima Crispi and Dr. Eduard Gratacós.

